12-2016

An Integrated Approach for a Better Understanding of the Paleo-Hydrology and Landscape Evolution in the Sahara During the Previous Wet Climatic Periods

Abotalib Zaki Abotalib Farag
Western Michigan University, tolba_rocky@hotmail.com

AN INTEGRATED APPROACH FOR A BETTER UNDERSTANDING OF THE PALEO-HYDROLOGY AND LANDSCAPE EVOLUTION IN THE SAHARA DURING THE PREVIOUS WET CLIMATIC PERIODS

by

Abotalib Zaki Abotalib Farag

A dissertation submitted to the Graduate College
in partial fulfillment of the requirements
for the degree of Doctor of Philosophy
Geosciences
Western Michigan University
December 2016

Doctoral Committee:

Mohamed Sultan, Ph.D., Chair
Rama Krishnamurthy, Ph.D.
Alan Kehew, Ph.D.
Neil Sturchio, Ph.D.
Peter Voice, Ph.D.

AN INTEGRATED APPROACH FOR A BETTER UNDERSTANDING OF THE PALEO-HYDROLOGY AND LANDSCAPE EVOLUTION IN THE SAHARA DURING THE PREVIOUS WET CLIMATIC PERIODS

Abotalib Zaki Abotalib Farag, Ph.D.

Western Michigan University, 2016

Paleoclimatic regimes over Saharan Africa alternated between dry and wet periods throughout the Pleistocene Epoch, and it is during the wet periods that the Saharan fossil aquifers were recharged. The present study investigates the role of groundwater-related processes in shaping the Saharan landforms (e.g., theater-headed valleys [THV]; depressions, escarpments, playas, and tufa deposits) over areas occupied by the largest of these aquifer systems, the Nubian Sandstone Aquifer System (NSAS). The present study reviews the suggested hypotheses for the origin of these landforms in the Sahara, and in similar settings elsewhere, and presents evidence in support of the following: during the Pleistocene wet periods groundwater under high hydrostatic pressures accessed deep-seated structures, discharged at the free faces, THV developed, scarps retreated, fluvial (in wet periods) and aeolian processes (in dry periods) together with seepage weathering eroded and transported loose debris, and depressions were formed. Evidence includes: (1) extensive distribution of THV indicative of sapping processes were mapped (using a GIS-based logistic regression model) along faulted scarps extending for over 1450 km in the NSAS; (2) widespread distribution of tufa deposits plastered on scarp faces of the natural depressions within

the NSAS with isotopic compositions consistent with deposition from NSAS fossil groundwater ($\delta^{18}O$: −12.8 to −8.0‰); (3) absence of well-developed drainage systems over the Libyan Plateau; (4) onset of endorheic streams from the identified THV along the NSAS escarpments (within the Qattara, Kharga, Farafra, and Dakhla depressions) and at the boundary between massive limestone formations and underlying erodible shale and argillaceous sandstone formations consistent with a groundwater discharge origin for the endorheic streams; (5) reported carbonate-rich playa deposits within scarp-foot depressions at the terminations of the endorheic streams; (6) artesian upward leakage of depleted NSAS groundwater (δD: −81 to −72‰; and $\delta^{18}O$: −12.8 to −8.0‰) into shallower Oligocene, Miocene, and Pliocene aquifers (δD: −0.7 to 7.2‰; $\delta^{18}O$: −1.13 to 1.20‰) as evidenced by the mixed isotopic composition (δD range: −62.6 to −2.6‰; $\delta^{18}O$ range: −7.0 to −1.09‰) of groundwater. Previous attempts to reconstruct the paleoclimatic conditions in the Sahara using basinal deposit (i.e. lacustrine, tufa and travertine) records is complicated by the groundwater origin of many of these deposits and by the lag between the time of groundwater recharge (timing of wet periods) and the time of groundwater discharge and deposition of basinal deposits. To constrain the timing of the wet periods in the Sahara, eleven samples were collected from 2 stratigraphic successions that were deposited from surface stream flow in a small watershed (Wadi Feiran) in Sinai and were dated using Optically Stimulated Luminescence (OSL). Quartz extracts from these sediments yielded OSL ages between ca. 27 and 11 ka and place these wetter conditions during the last glacial period. The present study contributes to our understanding of the nature and timing of the wet

climatic periods in Saharan Africa and Arabia and emphasizes the possible role of groundwater sapping in the evolution of the Saharan and Arabian landscape, similar settings worldwide, and of the Martian landscape as well.

ACKNOWLEDGMENTS

All praises for Almighty ALLAH, who guides us in darkness and help us in difficulties and due respect of Holy Prophet (Peace be upon him) who enable us to recognize our creator.

I was extraordinarily fortunate in having Dr. Mohamed Sultan as my advisor. Without Dr. Sultan's great advice, encouragement, support and help this work would not have been completed. I am indebted to him more than he knows. I am also grateful to Dr. R. V. Krishnamurthy for the invaluable discussions and suggestions throughout each phase of the project.

Thanks and appreciations are expressed to my committee members, Dr. Alan Kehew, Dr. Neil Sturchio and Dr. Peter Voice, who kept an eye on the progress of my work and always were available when I needed their advice.

I really appreciate the support of Dr. Racha Elkadiri for helping me to run the geostatistical models and for her fruitful discussions and valuable suggestions.

I also express my thankfulness to my colleagues in the Earth Science Remote Sensing Facility (ESRS) for their valuable support, encouragement, advice and help in difficult times. I'll never forget you guys (Abdullah, Karem, Dr. Mohamed, Dr. Abdou, Sita, Kyle, Mustafa, Hanah, Essayes, Lamees, Abdulaziz).

Where would I be without my family? My Mother is the one who sincerely raised me with her caring and gently love. I am grateful for my brothers and sisters for rendering me the sense and the value of brotherhood. I am glad to be one of them. Thanks for being supportive and caring siblings.

This research is funded by the Egyptian Ministry of Higher Education and Scientific Research.

Finally, I would like to thank everyone who was important to the successful realization of thesis, as well as expressing my apology that I could not mention personally one by one.

Abotalib Zaki Abotalib Farag

TABLE OF CONTENTS

ACKNOWLEDGMENTS ii

LIST OF TABLES vi

LIST OF FIGURES vii

CHAPTER

1. INTRODUCTION 1

    1.1 Dissertation Framework 1

    1.2 Background 3

    1.3 Geologic, Hydrologic, and Topographic Settings of the NSAS 9

2. DATA SETS 15

    2.1 Remote Sensing Data Sets 15

    2.2 Geologic Maps 16

    2.3 Isotopic and Chronological Data 17

3. REGIONAL DISTRIBUTION OF THV ACROSS THE NSAS 22

    3.1 Database Generation (Inventory and Predictor Variables Preparation) 22

    3.2 Model Construction, Validation, and Results 25

    3.3 Spatial Correlation between Delineated THV, Tufa and Playa Deposits, and Stream Networks 29

4. LANDSCAPE ANALYSIS OF SELECTED GEOMORPHOLOGICAL SITES IN THE NSAS 33

    4.1 Minimal Contribution of the Libyan Plateau Exorheic Drainage Systems 33

Table of Contents—Continued

CHAPTER

4.2 High Structural Control 37

4.3 Strong-Over-Weak Stratigraphy 43

4.4 Abundant Denudational Landforms and Tracers for Groundwater Activity 46

4.5 Remnant Hills in the Farafra Depression: Polygonal Fault-related or Denudational Features 56

5. LITHOLOGIC AND ISOTOPIC CHARACTERISTICS OF PLAYA AND TUFA DEPOSITS AND GROUNDWATER 60

5.1 Lithologic Characteristics of Playa Deposits 60

5.2 Isotopic Analysis of Tufa Deposits 61

5.3 Isotopic Analysis of Groundwater Samples 63

6. DISCUSSION 68

6. 1 Groundwater versus Surface Runoff Models 68

6. 2 Conceptual Model 73

6. 3 Timing of Wet Periods 76

7. TIMING OF WET CLIMATIC PERIODS; OPTICALLY STIMULATED LUMINESCENCE (OSL) AGES OF THE SINAI QUATERNARY DEPOSITS 82

7.1 Geologic Setting 82

7.2 OSL Sample Collection and Analysis 88

7.3 Interpretation and Implications of OSL Dates 92

8. REGIONAL AND PLANETARY IMPLICATIONS 92

8.1 Implications for Landscape Evolution in the Sahara-Arabian Desert Belt 92

Table of Contents—Continued

CHAPTER

8.2 Implications for Paleoclimate Variability in North Africa and Arabia 96

8.3 Implications for the Origin of Outflow Channels in Valles Marineris, Mars 97

9. SUMMARY 100

REFERENCES 103

APPENDICES

A. Isotopic Composition of Quaternary Deposits in the Eastern Sahara and Inferred Isotopic Composition of the Waters from which these Deposits Were Formed 131

B. Age Dating of Lacustrine, Travertine and Tufa Deposits in the Sahara 137

LIST OF TABLES

1. Sample locations, well information, O and H isotopic compositions for groundwater samples from wells tapping the NAS, Miocene, and Pliocene aquifers in north Western Desert, Egypt..... 20

2. Carbon isotopic data and ^{14}C model ages for investigated groundwater samples..... 21

3. Upslope contributing areas and minimum eroded volume of selected THVs in the Sahara and in the Snake River Plain, Idaho, USA..... 36

4. Optically stimulated luminescence (OSL) age on quartz grains from Quaternary deposits in Feiran Oasis, Sinai, Egypt..... 90

5. Optically stimulated luminescence (OSL) age on quartz grains from Quaternary deposits in Tarfa Oasis, Sinai, Egypt..... 90

LIST OF FIGURES

1. Location map. (A) Hillshade map for the study area in the Western Desert of Egypt and northern Sudan showing the distribution of depressions and sample locations for O and H isotopic analyses (yellow circles). 8

2. Hydrostratigraphy of the NSAS. 12

3. Hillshade map for the study area showing the distribution of playas. 13

4. Typical features for THV in plain view (left) and in cross section (right). 14

5. Google Earth images showing selected THV in the Western Desert (left) and the LR model-delineated pixels (red squares) along the alcoves (right). 28

6. Color-coded digital elevation model showing the spatial correlation between the distribution of THV-rich escarpments and tufa deposits. 31

7. Radarsat-1 mosaic over southwest Egypt and northern Sudan showing the distribution of reported playa deposits. 32

8. Delineated stream networks over the THV-rich escarpments and the Libyan Plateau showing minimal contribution of plateau surface runoff to depressions and their bounding escarpments in the Qattara. 35

9. Distribution of major fault traces, deep-seated faults, and the Pelusium meagashear system. 41

10. Local structural control on the spatial distribution of THV. 42

11. Simplified stratigraphic cross sections across the selected four sites. 45

12. Denudational landforms along the northern Qattara escarpment. 51

13. Denudational landforms in the Kharga depression (Wadi El-Medawara embayment). 52

14. Denudational landforms in the Farafra depression. 53

15. Three-dimensional model of Teneida playa basin and Abu Tartur Plateau. 54

16. Features related to salt weathering in the Qattara depression. 55

17. (A) Shaded-relief image showing the distribution of the Khoman Formation (Klitzsch et al., 1987) and locations of circular basins and polygonal features in limestone formations in the Western Desert. 59

18. (A) Distribution of groundwater samples from this study (solid symbols) and from previous studies. 66

19. δD versus $\delta^{18}O$ plot for groundwater samples from fossil Nubian aquifer NAS (Group I), OMPQ aquifer (Groups II and III), and Quaternary Nile Aquifer Group (IV). 67

20. Block diagram of the NSAS (modified from Salem and Pallas, 2004). 75

21. Hydrologic cross section of the Dakhla basin in the NSAS showing predicted groundwater ages (in thousands years) based on average groundwater velocity in the NAS. 79

22. Summary of the reported ages of lacustrine, travertine and tufa deposits in the Eastern Sahara. 80

23. Frequency distribution of reported ages for basinal deposits collected from the Eastern Sahara. 81

24. (A) Location map of the Feiran watershed. 84

25. Field shots of various lithofacies within the Quaternary deposits of the Feiran watershed. 85

26. Lithostratigraphic section for the Quaternary deposits in Feiran Oasis..... 86

27. Lithostratigraphic section of the Quaternary deposits in Tarfa Oasis. 87

28. Distribution of THV in Saharan and Arabian fossil aquifers. 95

29. Color-coded digital elevation model extracted from the MOLA mosaic for the eastern region of Valles Marineris and surroundings..... 99

CHAPTER 1

INTRODUCTION

1.1 Dissertation Framework

The present work provides an integrated (geochemistry, geochronology, remote sensing, and geographical information system [GIS]) approach aimed at deciphering the role that the groundwater processes could have played in shaping the Saharan landscape and the implications of findings from the present study on similar settings elsewhere and on the evolution of the Martian landscape. The area covered by the Nubian Sandstone Aquifer System (NSAS) that extends in four countries (Egypt, Sudan, Libya, and Chad) was used as the site.

The thesis is divided into nine chapters. Chapter 1 provides a brief overview of the geologic, hydrologic and topographic settings of the NSAS. It also investigates the prominent landforms observed in the Sahara including natural depressions, escarpments, and theater-headed valleys (THV), and lists the hypotheses that were proposed to explain their origin in the test site and in other areas worldwide as well. Special attention was dedicated to the THV, as their distribution could indicate areas of extensive groundwater discharge in previous wet climatic conditions. A detailed description of datasets used in this study including remote sensing data, geologic maps, isotopic and chronological data was provided in Chapter 2.

Chapter 3 discusses the mapping of the regional distribution of THV across the NSAS using remote sensing-based geostatistical modeling (e.g. logistic regression); it also examines the spatial correlation of the delineated THV with the distribution of tufa and playa deposits, and stream networks in search for causal relationships. Chapter 4 provides additional insights into the origin of the Saharan THV by using detailed landscape analysis of selected geomorphological sites, all of which display abundant THV occurrences. Specifically, it discusses the prominent and common topographic, structural, stratigraphic and morphological characteristics of the THV-rich sites in the Sahara whose presence is indicative of groundwater-related processes.

Chapter 5 focuses on the investigation of lithological and isotopic characteristics of playa and tufa deposits in the Sahara; it also examines the relationships between lithofacies characteristics, the isotopic composition of these deposits, and their spatial distribution in relation to that of the THV along depression-bounding escarpments. Furthermore, the chapter addresses the artesian upward leakage from the deep Nubian Aquifer System (NAS) into the overlying aquifers using isotopic analysis of groundwater samples collected from both the NAS and the overlying aquifers.

Chapter 6 discusses the findings from the previous chapters, examines the popular models for the origin of THV and associated landforms (i.e. groundwater sapping versus surface runoff), and demonstrates that the former model, not the latter, is consistent with findings from the Sahara. Moreover, the chapter provides a conceptual model that shows in detail the mechanism of formation for THV and natural

depressions in the Sahara. Finally, it discusses the implications of the present study findings on the timing of wet periods in the Sahara. Specifically, the chapter describes the uncertainties associated with the use of the ages of the basinal deposit ages in the Western Desert to infer the timing of the Saharan wet periods. In Chapter 7, an alternative and viable setting and test site was provided for accurate identification of the Saharan wet periods. This involves a detailed investigation (i.e. field, stratigraphic and OSL dating) of the Quaternary deposits in the Feiran watershed in Sinai.

The regional implications of the present study's findings on the landscape evolution of, and paleoclimatic interpretations for, the Saharan-Arabian desert belt are provided in Chapter 8. This chapter also describes the apparent similarities of the Martian denudational landscape features to those observed in the Sahara, the potential role and significance of the groundwater processes in shaping the Martian landscape, and the implications of such processes on the evolution of the Martian landscape. The findings from the present study are summarized in Chapter 9.

1.2 Background

The Saharan Desert is the largest hyper-arid area (9,400,000 km^2) on Earth, receiving less than 5 mm of average annual precipitation (New et al., 2000). It extends from the Atlantic Ocean in the west to the Red Sea Hills in the east, and from the Mediterranean Sea in the north to the Sahel zone in the south. Previous studies on the distribution and origin of fossil groundwater, fluvial landforms, and paleo-channel river systems, wind regimes, and deposits (e.g., tufa, playas, and cave fillings) indicate that

paleoclimatic regimes of the North African Sahara alternated between dry and wet periods throughout the past several million years (Szabo et al., 1995; Smith et al., 2004a, 2004b; Sultan et al., 2007; Abouelmagd et al., 2012). During the wet periods the aquifers in North Africa were recharged during interglacial periods through the intensification of the paleomonsoons (Yan and Petit-Maire, 1994) or in glacial periods by intensified paleowesterlies (Sultan et al., 1997, Sturchio et al., 2004; Abouelmagd et al., 2012); during these periods a considerable rise of the paleopiezometric surfaces was reported (Causse et al., 1989; Pachur and Hoelzmann, 2000). The largest of these aquifer systems is the Nubian Sandstone Aquifer System (NSAS; area: 2.6×10^6 km^2) in Egypt, Libya, Sudan, and Chad. The NSAS occupies around 20% of the Sahara (Fig. 1). There are other large fossil aquifers such as the North Western Sahara Aquifer System (NWSAS; area: 1.2 million km^2) in Algeria, Tunisia, and Libya, and smaller fossil aquifers ($<900 \times 10^3$ km^2) including the Iullemeden Aquifer, the Western Sahara Aquifer, and the Taoudeni Aquifer (IGRAC, 2012; Fig. 1). Similar fossil aquifers (e.g., the Upper Mega Aquifer) were reported from the neighboring deserts in Arabia.

Areas occupied by the NSAS are dominated by extensive outcrops of flat-topped carbonate plateaus, hereafter referred to as the Libyan Plateau, and natural depressions (Kharga, Dakhla, Farafra, Bahariya, and Qattara depressions; Fig. 1) that cover large areas and are bound by escarpments. Deep canyons, hereafter referred to as theater-headed valleys (THV), are incised in these escarpments and playa and tufa deposits are found proximal to these escarpments. The origin of these escarpments,

natural depressions, THV, tufa and playa deposits and the role of groundwater as a denudational process in shaping the landscape has not been fully investigated.

Proposed origins for the natural depressions and bounding escarpments include wind deflation, fluvial systems and stream erosion, tectonic deformation, and salt weathering. The presence of cliffs on the upwind side of the Qattara, Siwa, Farafra and Dakhla depressions, the gentle slopes on the downwind side (Aref et al., 2002) and the abundance of dune fields along the wind trajectory downwind of the depressions supports the wind deflation hypothesis (Ball, 1927; Squyres and Bradley, 1964). However, wind deflation alone cannot breach the limestone cap rocks, a condition that is required to expose the underlying clastic strata to erosion and deflation by aeolian processes (Albritton et al., 1990). Fluvial systems and stream erosion models (McCauley et al., 1982; Said, 1983; Albritton et al., 1990) provide adequate solutions for the removal of the limestone cap rock by integrated surficial erosion, karstic and mass wasting processes, yet the absence of notable exorheic streams (Kropelin, 1993) that drain toward depressions sheds doubt on the validity of this model. A tectonic origin for the Dakhla and Kharga oases is supported by the thin sedimentary cover (~120 m) and the structural expression of the basement uplifts in these areas (Said, 1979; Gindy et al., 1991), but is less relevant for the depressions within the northern Libyan Plateau, an area that is identified as being a stable shelf since the Early Miocene (Albritton et al., 1990; Abdeldayem, 1996). Erosion by salt weathering coupled with wind and stream activity (Aref et al., 2002) is supported by the extensive distribution of salt weathering-related features in Eastern Sahara (Goudi, 2013), but the model

cannot account for the presence of deep canyons within the escarpments and for the associated mass wasting.

The role of groundwater as a denudation process that locally shaped the landscape of the Sahara was suggested by Maxwell, (1982); he stated that the deep canyons incised into the Gilf Kebir Plateau was eroded by cliff sapping and spring discharge, but the mechanism of erosion remained ambiguous until the groundwater sapping processes were proposed and modeled by Luo et al. (1997). Specifically, they modeled groundwater discharge along deep-seated faults bounding the escarpments of the Kharga depression in the Western Desert of Egypt, mass transport by discharged water, escarpment retreat, and development of THV along the compromised escarpments.

The term "groundwater sapping" refers to the undermining, collapse, and retreat of valley head and side walls by the weakening or removal of the basal support as a result of weathering and erosion processes associated with the groundwater outflow along the seepage plane (Dunne, 1980; Laity and Malin, 1985; Irwin et al., 2014). Stream networks associated with groundwater sapping processes differ from those related to overland flow stream systems in their overall patterns, stream characteristics (stream profile, width, density, and onset location), and the degree to which structures control stream distribution (Laity and Malin, 1985; Luo et al., 1997; Hoke et al., 2004).

For several decades, THV have been considered by default as groundwater sapping–related landforms in many areas worldwide, including the Western Desert, Egypt (Luo et al., 1997); Hackness Hills, England (Nash, 1996); Apulia region,

southern Italy (Mastronuzzi and Sanso, 2002); Altiplano Plateau, northern Chile (Hoke et al., 2004); slopes of the Kohala volcano, Hawaii, USA (Kochel and Piper, 1986); the Colorado Plateau, USA (Laity and Malin, 1985); the Southern High Plains, USA (Wood, 2002); Obara Hills, Japan (Onda, 1994); and the Canterbury Plain, New Zealand (Schumm and Phillips, 1986). The THV were also recognized on the Martian surface (Higgins, 1982; Kochel and Piper, 1986; Malin and Edgett, 2000).

The proposed groundwater origin for the formation of THV was later challenged by findings from field and experimental studies. These studies suggested that the valleys should not be exclusively attributed to groundwater seepage, but other processes (e.g., megaflooding, waterfall erosion, landslides, and differential weathering) could play a major role in their formation as well (Lamb et al., 2006, 2008, 2014; Lamb and Dietrich, 2009; Craddock et al., 2012; Marra et al., 2014; Irwin et al., 2014). The major arguments that were advanced against the seepage erosion origin are the bedrock strength and the large size of THV, which requires not only extensive weathering and/or the presence of gigantic water discharge to disintegrate bedrock and remove (transport) weathering products away from the escarpment, but also for these processes to be active for substantial timespans to remove the large amounts of weathered material (Howard and Kochel 1988; Howard and Selby, 1994; Lamb et al., 2006).

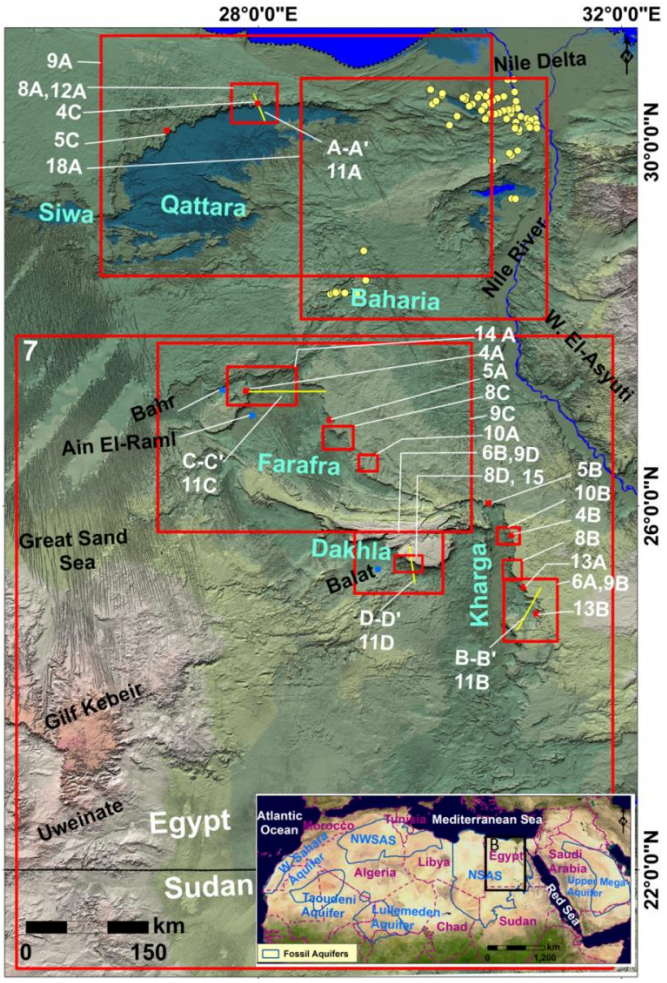

Figure. 1. Location map. (A) Hillshade map for the study area in the Western Desert of Egypt and northern Sudan showing the distribution of depressions and sample locations for O and H isotopic analyses (yellow circles). Open red boxes outline areas covered by Figures 6A, B, 7, 8A, B, C, D, 9A, B, C, D, 10A, B, 12A, 14A, 15, and 18A; solid red boxes outline areas displayed in Figures 4A, B, C, 5A, B, C, 13A, and B; transects A–A′, B–B′, C–C′, and D–D′ denote cross sections displayed in Figure 11A, B, C, and D. Inset shows the location of the study area (Box B) and the distribution of fossil aquifers across North Africa and Arabia.

1.3 Geologic, Hydrologic, and Topographic Settings of the NSAS

The NSAS is largely composed of: (1) pre–Upper Cretaceous continental sandstone formations (Nubian Aquifer System [NAS]), and (2) Upper Cretaceous–Tertiary marine carbonates that give way to Mio-Pliocene sandy formations (Post-Nubian Aquifer System [PNAS]) and build up the so-called Libyan Plateau (Fig. 2) (Thorweihe, 1990; Bakhbakhi, 2006). The continental and marine sequences in the NSAS are separated by confining shale and clay layers of Cenomanian age (Thorweihe and Heinl, 2002). The thickness of the marine carbonates overlying the NAS aquifer increases northward (from 400 to 2000 m; Shata, 1982).

The NSAS is heavily dissected by sub-vertical deep-seated faults, many of which are basement structures that were reactivated by tectonic activities at later time periods (Neev et al., 1982; Sultan et al., 2007). These include east-west—trending (Kalabsha trend) and northeast-southwest—trending (Pelusium trend) fault systems in the southern and northern Western Desert, respectively (Neev et al., 1982; Hermina, 1990; Thurmond et al., 2004; Khan et al., 2014).

Measurements of radiochlorine (^{36}Cl) and radiokrypton (^{81}Kr) isotopes in deep groundwater from the northern regions of the NSAS indicate very long residence time (up to 1.3×10^6 years; Sturchio et al., 2004; Patterson et al., 2005) except for areas proximal to the recharge areas, where reported ages do not exceed a few tens of thousands of years (Haynes and Haas, 1980). The recharge areas for the NSAS are found in the south, where the NAS crops out. Unconfined aquifer conditions prevail in the south and give way to confined conditions north of latitudes 25°N (Sturchio et al.,

2004), giving rise to a regional groundwater flow from southwest to northeast and from south to north (Shata, 1982; Thorweihe, 1990; Salem and Pallas, 2004).

Because of the extensive faulting in the NAS (Neev and Hall, 1982; Shata, 1982; Thorweihe, 1990) and the high artesian pressure of the overlying thicknesses, artesian upward leakage takes place along deep-seated faults and recharges the overlying PNAS aquifer (Shata, 1982; Sultan et al., 2007). Furthermore, discharge occurs in depressions where the groundwater level intersects the surface. These depressions enclosed several paleolakes during Pleistocene wet periods and are now the sites of playa deposits under present dry conditions. Examples include the Balat and Bahr playas in Egypt (Hassan et al., 2001; Brookes, 2010) (Fig. 1). Under present-day arid conditions, discharge in closed depressions (e.g., the Qattara depression in Egypt) produces evaporative sabkha deposits (Aref et al., 2002; Salem and Pallas, 2004).

As described earlier, the landscape of the NSAS is dominated by extensive flat-topped, gently dipping strata that are truncated by depressions and escarpments, many of which are structurally controlled (Said, 1979; Robinson, 2002). Proximal to, and at the foothills of, these escarpments are springs and depressions; plastered on the walls of some of these escarpments, and located at scarp-foot depressions (e.g., the Kharga and Dakhla depressions) (Fig. 3), are groundwater tufa deposits of varying ages (Smith et al., 2004a; Adelsberger and Smith, 2010; Brookes, 2010). For example, reported tufa ages ranged from 50 to 600 ka in the Kharga depression, and from 80 to 620 ka in the Dakhla depression (Smith et al., 2004a; Brookes, 2010; Jimenez, 2014). The THV were

reported in the Kharga and Farafra depressions and the following features were identified as indicative of their presence: (1) headward channel growth; (2) scallop-shaped escarpment edges; (3) stubby-looking geometry; (4) theater-like heads; (5) U-shaped profiles with valley-width ratio exceeding 1.0 (Pedrera et al., 2009); (6) flat floors; and (7) structurally controlled patterns (Luo et al., 1997). These features, together with three additional features (1) low stream order; (2) asymmetrical drainage patterns (Laity and Malin, 1985; Kochel and Piper, 1986; Schumm et al., 1995); and (3) high junction angles (>55˚; Kochel and Piper, 1986; Devauchelle et al., 2012) were used to delineate similar THV in the Colorado Plateau, Hawaii, and Florida Panhandle.

A wide distribution of features indicative of the presence of THV was revealed from the examination of Google Earth images draped over digital topography and cross sections across valleys in the Kharga and Farafra depressions, the areas where the THV were first reported by Luo et al. (1997), and in the Qattara depression (Fig. 4).

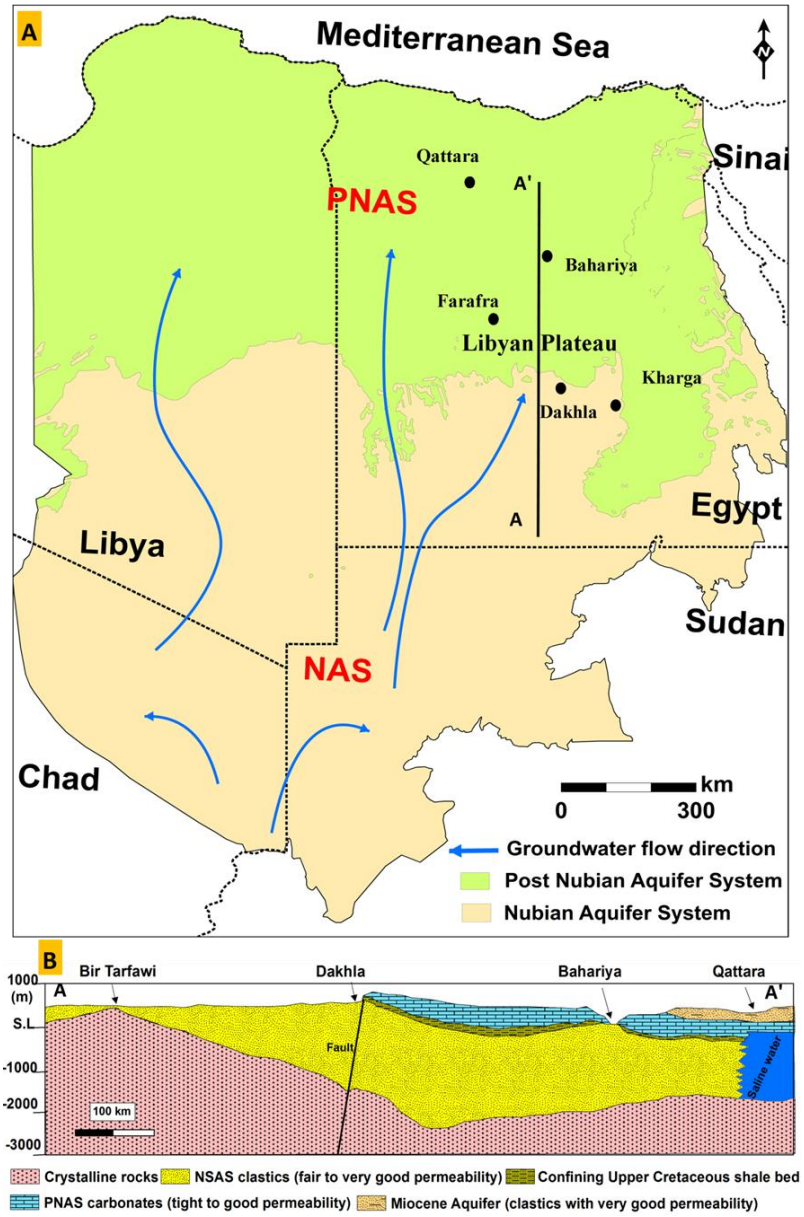

Figure. 2. Hydrostratigraphy of the NSAS. (A) Sketch map showing the distribution of the NSAS, the PNAS, and the unconfined section of the underlying NAS, and the groundwater flow directions within the NSAS. (B) Simplified hydrostratigraphic cross-section along line A–A′ plotted in Figure 2A showing the distribution of the NAS and PNAS aquifer systems (modified from Thorweihe, 1990).

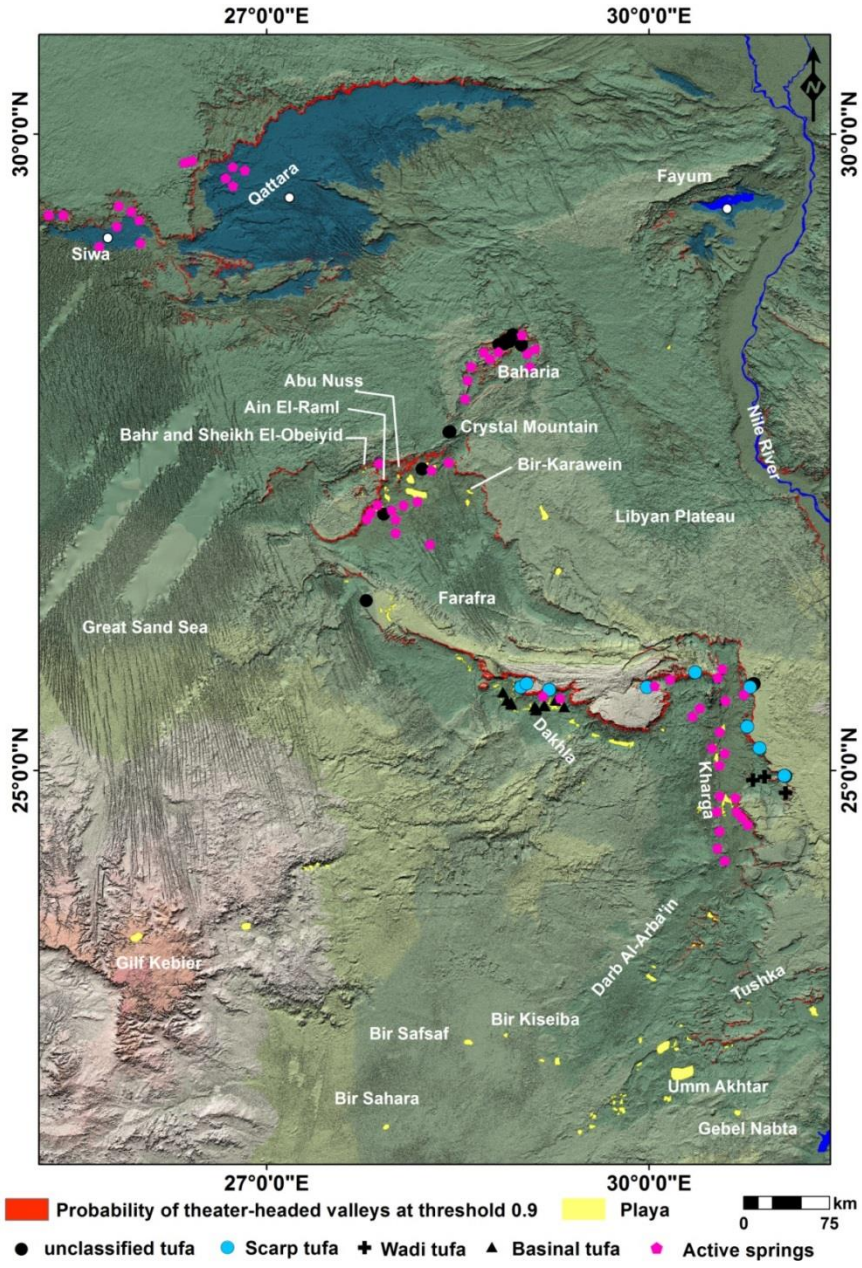

Figure. 3. Hillshade map for the study area showing the distribution of playas (El-Hinnawi et al., 2005, 2006), tufa deposits (Smith, 2001; Kieniewicz and Smith, 2009; Torab, 2013; Jimenez, 2014), springs (Klitzsch et al., 1987), and our LR model outputs (distribution of modeled THV).

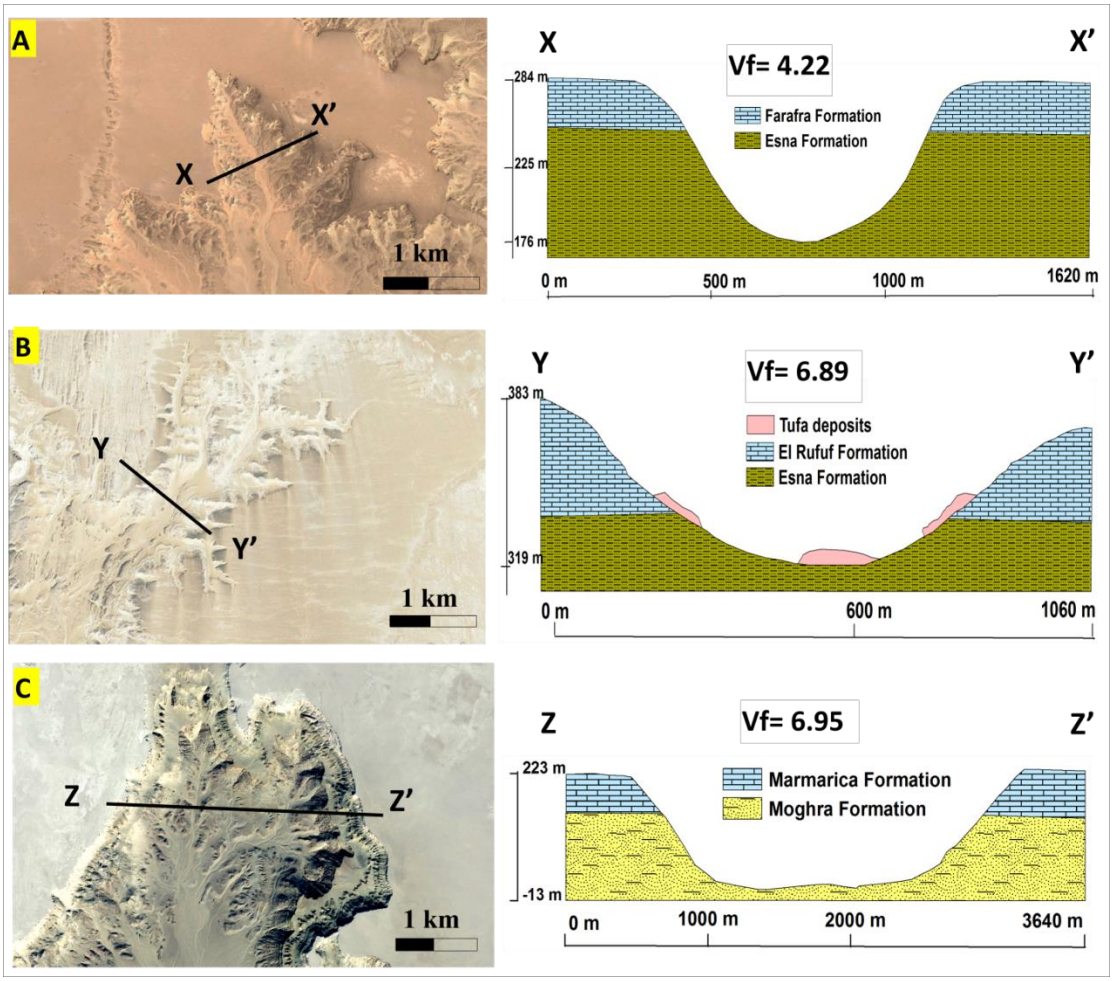

Figure 4. Typical features for THV in plain view (left) and in cross section (right) in the Farafra (4 A), Kharga (4B), and Qattara (4C) depressions, including stubby-looking geometry, theater-like heads, structural control patterns, U-shaped profiles, valley height-width (Vf) values > 1, flat floors, and low stream order. Stratigraphic data in cross sections were derived from Klitzsch et al. (1987), Luo et al. (1997); El-Hinnawi et al. (2005, 2006), and field measurements. Areas covered by Figure 4A, 4B, and 4C are outlined by solid red boxes 4A, 4B, and 4C, respectively, in Figure 1.

CHAPTER 2

DATA SETS

The collection and analysis of data was carried out on both the local and regional scales. Three main types of datasets were used: (1) remote sensing, (2) geologic maps, and (3) isotopic and chronological datasets. All datasets were co-registered to a unified projection (Datum: WGS-84; UTM Zone: NSAS N36, NWSAS N32, Upper-Mega Aquifer System N38) in a GIS environment.

2.1 Remote Sensing Data Sets

Remote sensing data sources include: (1) Advanced Spaceborne Thermal Emission and Reflection Radiometer (ASTER) digital elevation model (DEM) mosaics (scenes: 12; spatial resolution: 30 m; source: USGS website[1]; coverage: the Qattara, Kharga, Farafra and Dakhla depressions in Egypt, Gebel El-Gharbi in the NWSAS, and Al-Guwifa area in Saudi Arabia), Shuttle Radar Topography Mission (SRTM) DEM mosaics (tiles: 475; spatial resolution: 90 m; source: USGS website; coverage: NSAS, NWSAS, and Najd Plateau); (2) painted hillshade images for the NSAS, the NWSAS, and Najd Plateau derived from the DEMs using the Arc hillshade tool (ESRI Arc GIS v.10); (3) drainage networks and watershed boundaries extracted from SRTM and ASTER DEMs using D8 flow direction algorithms (O'Callaghan and Mark, 1984) in Arc Hydro tool (ESRI Arc GIS v.10); (4) Landsat 4-5 Thematic Mapper (TM) mosaic bands 7, 4, and 2 (scenes: 11; spatial resolution: 30 m; source: Global Land Cover

[1] www.earthexplorer.usgs.gov

Facility database[2]; coverage: north Western Desert of Egypt); (5) false-color composite (blue: band 2; green: band 4; and red: band 7) Landsat 8 mosaic (three scenes; spatial resolution: 30 m source: USGS website; coverage: the Kharga depression in Egypt, Gebel El-Gharbi in the NWSAS, and Al-Guwifa area in Saudi Arabia); (5) high-resolution 3D models generated from Landsat 8 and ASTER DEM following the application of a resolution merge (Gram-Schmidt Pan Sharpening method; Li et al., 2004) of multispectral Landsat 8 images (spatial resolution: 30 m) with panchromatic Landsat 8 images (spatial resolution:15 m); (6) Radarsat-1 mosaic (tiles: 2; spatial resolution: 30 m; source: Canadian Space Agency website[3]; coverage: Egypt and northern Sudan); (7) Geoeye images (scenes: 8; spatial resolution: 1 m; source: Google Earth imagery; coverage: Qattara, Kharga, and Farafra depressions; (8) merged Advanced Land Imager (ALI) (scenes: 1; spatial resolution: 10 m; source: USGS website; coverage: Qattara), and (9) Mars datasets including Mars Orbiter Laser Altimeter (MOLA) mosaic and the High-Resolution Stereo Camera (HRSC) mosaic (ESA/DLR/FU Berlin; source: the Geosciences Node of NASA's Planetary Data System at Washington University in St. Louis).

2.2 Geologic Maps

The following geologic maps were utilized: (1) mosaicked geologic map for the Western Desert (scale: 1: 500,000; sheets: 15; coverage: Western Desert, Egypt;

[2] www.landcover.org
[3] www.asc-csa.gc.ca/eng/ / satellites radarsat1/mosaic.asp

Klitzsch et al., 1987); (2) mosaicked geologic map for the northern Western Desert (scale: 1: 250,000; sheets: 25; coverage: north Western Desert, Egypt; El-Hinnawi et al., 2006); (3) mosaicked geologic map for the south Western Desert (scale: 1: 250,000; sheets: 30; coverage: south Western Desert, Egypt ; El-Hinnawi et al., 2005); (4) distribution of deep-seated and surface regional faults for the Western Desert (coverage: Western Desert, Egypt; Klitzsch et al., 1987; El-Hinnawi et al., 2005; 2006; Wescot et al., 2011); (5) detailed stratigraphic sections for the Western Desert, Egypt (coverage: the Kharga, Farafra and Dakhla depressions; Hermina, 1990); and (6) distribution of tufa and playa deposits in the Western Desert (coverage: south Western Desert, Egypt; source: Crombie et al., 1997; Sultan et al., 1997; Smith, 2001; El-Hinnawi et al., 2005; Jimenez, 2014)

2.3 Isotopic and Chronological Data

Twenty groundwater samples were collected for isotopic analyses (H and O) from the Bahariya Oasis, tapping the NAS (10 samples), and from Wadi El-Natrun and Wadi El-Farigh areas (10 samples), tapping the Miocene and Pliocene aquifers (Table 1; Fig. 1). Wells were pumped for a minimum of 20 to 30 minutes prior to sample collection. Groundwater samples were collected in 100 ml polyethylene bottles and tightly capped. Stable isotope ratios of H and O in water were measured at ISOTECH Laboratories in Champaign, Illinois, USA using a Picarro cavity ring-down spectroscopy (CRDS) laser system (Lehmann et al., 2009). The isotopic data for samples are reported (Table 1) in terms of the conventional delta (δ) notation, in units

of per mil (‰) deviation relative to Vienna Standard Mean Ocean Water (V-SMOW; Coplen., 1996), whereby

$$\delta\ (‰)\ =\ [(R\ sample/R\ standard)\ -\ 1]\ \times\ 10^3 \qquad (1)$$

and $R = {}^2H/{}^1H$ or ${}^{18}O/{}^{16}O$

For comparison purposes, additional reported analyses were included for samples from the northern part of the Western Desert from: (1) Oligocene, Miocene, and Quaternary aquifers in El-Fayum area (21 samples: Thompson, 2007), and from (2) Miocene, Pliocene, and Quaternary aquifers (30 samples: El-Gamal, 2005) (Fig. 1).

Four groundwater samples (S.31, S.33, S.61, and S.62) were collected for ^{14}C dating along two east-west—trending traverses west of the Nile Delta. Dissolved inorganic carbon (DIC) was first extracted in a vacuum by acidifying the sample, and the extracted carbon dioxide was cryogenically purified from other reaction products and catalytically converted to graphite (Vogel et al., 1984). Graphite $^{14}C/^{13}C$ ratios were measured using the 0.5 MeV accelerator mass spectrometer at the University of Georgia Center for Applied Isotope Studies (Cherkinsky et al., 2010). The ^{14}C isotopic abundances are reported (Table 2) in percent modern carbon (pmC), relative to that in atmospheric CO_2 in 1950 (Stuiver and Polach, 1977). Model ages are given in radiocarbon years before 1950 (years B.P.), using a ^{14}C half-life of 5568 years. The error is quoted as one standard deviation and reflects both statistical and experimental errors. The data was corrected for isotopic fractionation. For comparison purposes, the

results from the present study were compared to reported ^{14}C ages for groundwater samples collected along an east-west transect to the west of the Nile Delta (Aeschbach-Hertig et al., 2007).

Table 1. Sample locations, well information, O and H isotopic compositions for groundwater samples from wells tapping the NAS, Miocene, and Pliocene aquifers in north Western Desert, Egypt

Well No.	Name	Latitude N	Longitude E	Aquifer type	DWT* (m)	δ D (‰)	$\delta^{18}O$ (‰)
31	El-Sedk Farm	30.5137	30.0240	Production well in Pliocene	26	-12.6	-1.37
32	Sabry Harfoush Farm	30.4187	29.9163	Production well in Miocene	150	10.1	1.29
33	El-Zoghbi Farm	30.4518	29.9566	Production well in Miocene		2.6	0.42
34	Ali Salem Farm	30.4707	30.2795	Production well in Pliocene		-7.0	-1.28
36	El-Tyseer Farm	30.5782	29.8966	Production well in Pliocene		7.3	0.99
37	Abu Gamous Farm	30.5355	30.0260	Production well in Pliocene		-5.6	-0.59
38	Spring	30.3950	30.3300	Artesian spring in Pliocene	artesian	-8.6	-1.61
61	Ahmed Atyia Farm	30.2866	30.189	Production well in Miocene	190	-14.4	-2.34
62	El-Wadi Farm	30.1867	30.1047	Production well in Miocene		-15.1	-2.37
63	Bir El-Geles	28.3538	28.8653	Production well tapping Nubian	30	-81.5	-10.74
64	Bir Haddad	28.3544	28.8709	Production well tapping Nubian	8	-80.6	-10.28
65	Ain Madi well	28.3284	28.7943	Production well tapping Nubian	20	-80	-10.25
66	Bir Tamania	28.3457	28.822	Production well tapping Nubian		-83.6	-10.87
67	Bir El-Meftella	28.3593	28.8472	Production well tapping Nubian	45	-83.1	-10.83
68	Bir Walid	28.3448	28.8516	Production well tapping Nubian		-83.4	-10.79
69	Bir Segam	28.343	28.9521	Production well tapping Nubian		-83.4	-10.85
70	Ain Youssef	28.3357	29.0836	Artesian well in the Nubian	artesian	-83.7	-10.82
71	Iron Mines	28.4817	29.1824	Production well tapping Nubian	110	-84.4	-10.81
72	El-Bohour Well	28.8062	29.1602	Artesian well tapping Nubian	artesian	-83.8	-10.96

* Depth to water table

Table 2. Carbon isotopic data and ^{14}C model ages for investigated groundwater samples

Well No.	GGAMS#	$\delta\ ^{13}C$ (‰)	^{14}C pMC	^{14}C model age Years B.P.
31	13317	−8.8	32.81 ± 0.11	8950 ± 30
33	13318	−7.6	10.46 ± 0.06	18140 ±40
61	13319	−9.1	38.04 ± 0.13	7760 ± 30
62	13320	−8.9	35.92 ± 0.13	8230 ± 30

CHAPTER 3

REGIONAL DISTRIBUTION OF THV ACROSS THE NSAS

Visual inspection of image products similar to those shown in Fig. 4 indicated that THV are widespread across the NSAS. To enable mapping of these features over the NSAS and across the entire Sahara, a GIS-based logistic regression (LR) model was developed to predict the presence or absence of THV based on values of a set of predictor variables, all of which were extracted from remote sensing datasets. The application of the model encompassed four steps: database generation, model construction, model validation, and model output generation.

3.1 Database Generation (Inventory and Predictor Variables Preparation)

The ten morphological characteristics listed above were used together with one additional feature (valley height-width ratio [Vf]) value (Fig. 2) to identify the locations of THV in the NSAS using remotely acquired data. The Vf was used to quantify the U-shaped cross section of THV (high Vf value: >1) relative to V-shaped valleys (Vf values: ~0) (Bull and McFadden, 1977; Pedrera et al., 2009). The ratio Vf can be written as:

$$Vf = 2Vfw/[(Eld - Esc) + (Erd - Esc)] \quad (2)$$

where Vfw is the width of valley floor, Eld is the elevation of the left local divide, Esc is the elevation of the valley floor, and Erd is the elevation of the right local divide.

Because of the extensive area covered by the NSAS and the inaccessibility of large areas within the NSAS, the adopted methodology heavily relies on observations extracted from high-resolution satellite imagery (viewable in Google Earth) that were field-verified in selected locations (e.g., the Farafra and Qattara depressions). Using these geomorphological criteria, a total of 1500 THV-present points and 1534 THV-absent points were identified. Selection of the THV-present points targeted the onset of the valleys only. THV in the NSAS range from tens of meters to few kilometers in cross section.

Although the THV are larger in dimensions than gullies, both have similar morphological characteristics; the THV and gullies share the headward growth, theater- or amphitheater-like heads, paucity of stream tributaries, vertical sidewalls, and tendency to occur along steep slopes (Luo et al., 1997; Martinez-Casanovas et al., 2004; Hobbs et al., 2014; Imwangana et al., 2015; Conway et al., 2015). To map the distribution of THV in the NSAS, LR statistical methods and predictor variables that were successfully used to map large gullies and topsoil depressions related to groundwater sapping or runoff erosion in Spain, Italy, Turkey, and Algeria (Martinez-Casanovas et al., 2004; Fernandez et al., 2008; Akgun and Turk, 2011; Luca et al., 2011; Conoscenti et al., 2014; Dewitte et al., 2015) were applied.

An SRTM mosaic over the NSAS was used to generate six predictor variable (slope angle, plan curvature, profile curvature, drainage density, stream power index

[SPI], and topographic wetness index [TWI]) images. Slope angle refers to the change in elevation over run in a particular direction. Plane curvature measures the surface curvature in a direction orthogonal to the slope, whereas profile curvature measures the rate of change of slope along a profile. Drainage density refers to the total length of all the streams and rivers within an area. SPI and TWI are useful indices for modelling the hydrodynamic behavior of water flow in connection with hillslope morphology and investigating the effects of terrain erodibility conditions (Fernandez et al., 2008; Elkadiri et al., 2014). The mathematical expressions of the SPI and TWI (Bagnold, 1966; Moore et al., 1991) can be written as:

$$SPI = ln\,[A * tan\,(S)] \qquad (3)$$

$$TWI = ln\,[\frac{A}{tan(S)}] \qquad (4)$$

Where A is the upslope contributing area and S is the slope angle.

THV are characterized by steep slopes (Laity and Malin, 1985; Howard and McLane, 1988; Dunne, 1980; Howard and Selby, 1994), negative plan curvatures (i.e., surface is increasingly concave towards valley sides), positive profile curvatures (i.e., surface is increasingly convex at higher elevations; Fernandez et al., 2008), low drainage density and low stream order (Laity and Malin, 1985; Kochel and Piper, 1986; Luo et al., 1997), and moderate SPI and TWI values given the high slope and small upslope contributing area for the THV. Measurements of the 1500 THV-present points

show that this is indeed the case (mean ± 1S: slope: 14.9° ± 6.5, plane curvature: −0.25±0.18, profile curvature: 0.17±0.06, stream density: 9.4±15.4, SPI: 8.6±1.2, TWI: 12.1±1.37).

A lithologic filter was generated and used to mask out areas to be omitted from the LR model. The filter is a binary (1, 0) lithologic map (spatial resolution: 90 m) that was used to identify areas with massive carbonate cap rock overlying easily eroded beds, a condition that was previously identified for the formation of THV in the Kharga depression (Luo et al., 1997). The model was applied only to the limestone-covered plateau in Egypt and Libya; thus, the mapped THV are probably those that formed under conditions and settings similar to those identified in the Kharga area.

3.2 Model Construction, Validation, and Results

The LR model is a logarithmic model that generates a multivariate regression relationship between one or more predictor variables and a response variable (Pradhan, 2010). It gives each variable a coefficient that measures its contribution to variations in the response variable. For this study, the response variable is a binary variable describing the presence and absence of THV. The logistic function equation is expressed as follows:

$$p = \frac{1}{1+\exp(a_0+a_1x_1+a_2x_2+\cdots+a_nx_n)} \qquad (5)$$

where p is the probability of THV occurrence; a0 is the equation intercept; x1, x2 to xn denote the predictor variables; and a1, a2 to an refer to the coefficients that need to be estimated for the predictor variables using a maximum likelihood optimization method (Amini et al., 2010; Elkadiri et al., 2014).

The application of the LR model involved six major steps. First, each input variable was normalized to the −1 to 1 range using the following equation:

$$X_{i,n} = \frac{X_i - (\frac{X_{Max}+X_{Min}}{2})}{(\frac{X_{Max}-X_{Min}}{2})} \qquad (6)$$

Where, X_i,n denotes the normalized value for X_i, X_i represents each data point, X_{Min} is the minima among the dataset, and X_{Max} is the maxima among the dataset. The normalization was applied to standardize the range of magnitude of inputs. Second, for each inventoried location (i.e. THV present or absent), values of the normalized input variables were extracted. Third, the available samples were portioned randomly into two subsets: training and testing. The former comprised 80% of the available locations (2427 pixel element locations) and the latter included the remaining 20% (607 pixel element locations). Fourth, the 80% data subset was analyzed using Minitab v.16 to extract the regression equation that best fits the input data. Fifth, the extracted LR model was tested on the remaining 20% of the data to determine the model accuracy in predicting the THV locations from the inputted morphological variables.

This test was conducted using the receiver operating characteristic (ROC) test, a widely applied measure of the performance of a predictive rule (Park et al., 2013). The ROC is defined as a curve connecting the sensitivity and the 1− specificity (Swets, 1988). Sensitivity is the fraction of positive occurrences of THV that is correctly predicted, whereas 1− specificity is the fraction of incorrectly predicted cases that did not occur. The area under the ROC curve (AUC) characterizes the quality of a forecast system by describing the system's ability to anticipate the occurrence or non-occurrence of predefined events correctly. A perfect model would have an AUC of 1.0 (Vorpahl et al., 2012); the conducted model had a high AUC value (0.87 or 87%). Sixth, a lithological filter was applied to mask out areas that are lacking previously identified conditions (hard on soft rock units; Luo et al., 1997) for the formation of THV.

The LR-delineated distribution for the THV across the NSAS is an occurrence probability map ranging from 0 to 1. Fig. 2 shows the distribution of the THV at probabilities equal to, or exceeding, a threshold value of 0.9. Inspection of Fig. 2 and other data sets (e.g., DEM or slope image) indicate that the majority of the identified THV occur along the edges of the carbonate plateau and along the escarpments of depressions within the plateau with a total length of 1450 km. Because the target was the onset of these valleys in the selection of the THV-present points, the LR-delineated distribution includes the topmost locations of the THV (alcoves), whereas the main channels of the valleys were not incorporated (Fig. 5). The delineated locations have the following characteristics: steep slope, positive profile curvature, and negative plan curvature. The area occupied by the delineated alcoves was estimated at 3436 km^2.

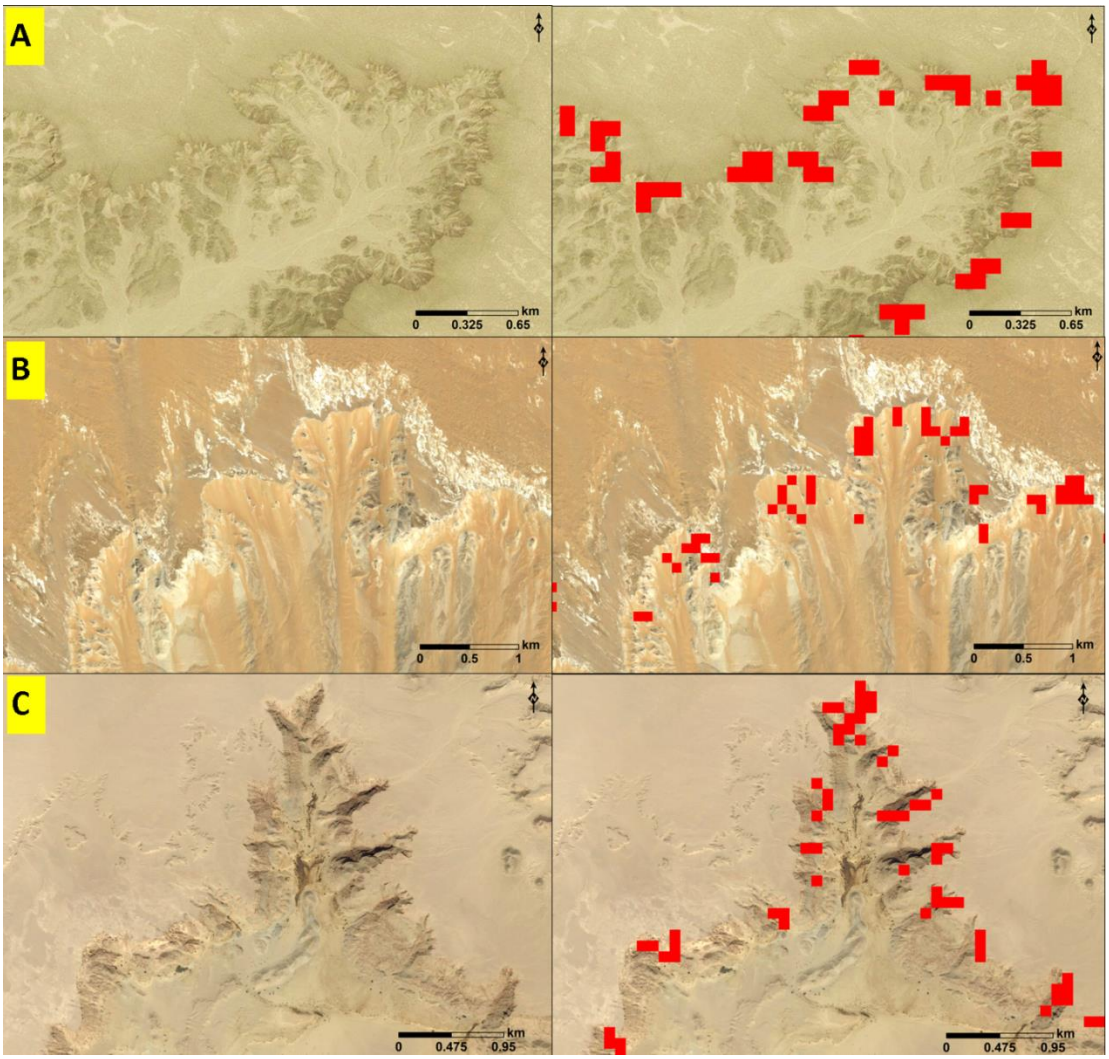

Figure 5. Google Earth images showing selected THV in the Western Desert (*left*) and the LR model-delineated pixels (*red squares*) along the alcoves (*right*) in the Farafra (Figure 5A), Kharga (Figure 5B), and Qattara (Figure 5C) depressions. Areas covered by Figsure 5A, 5B, and 5C are outlined by solid red boxes 5A, 5B, and 5C, respectively, on Figure 1.

3.3 Spatial Correlation between Delineated THV, Tufa and Playa Deposits, and Stream Networks

The spatial distribution of the delineated THV across the NSAS was correlated with that reported for tufa deposits (Sultan et al., 1997; Nicoll et al., 1999; Smith et al., 2004a, 2004b; Kieniewicz and Smith, 2009; Adelsberger and Smith, 2010; Torab, 2013; Jimenez, 2014) (Fig. 3). Inspection of Fig. 3 shows: (1) the delineated THV are concentrated along the peripheries of the Libyan Plateau escarpments and on the scarp faces of depressions within the Plateau, and (2) the reported occurrences and types (plateau, wadi, and basinal) of tufa deposits (Crombie et al., 1997; Smith et al., 2004b; Adelsberger and Smith, 2010; Brookes, 2010) and the majority of playa deposits (El-Hinnawi et al., 2005; El-Hinnawi et al., 2006) are proximal (<25 km) to the delineated THV (Figs. 3, 6, and 7). Scarp or plateau tufas are plastered along scarp faces at elevations exceeding present-day piezometric surfaces (i.e. 10–15 m below the level of the Libyan Plateau); compared to scarp tufa, wadi tufas are generally located at lower elevations and follow the old slope of the escarpment as thin inclined sheets or as thick horizontal strata (Smith et al., 2004b). Basinal tufas (also called spring tufa mounds) are associated with lacustrine playa deposits in scarp-foot depressions, with a maximum distance of 25 km from proximal escarpments (e.g., the Dakhla depression; Figs. 3 and 6).

Furthermore, the spatial distribution of the delineated THV across the NSAS was correlated with the reported distribution of lacustrine playa deposits (El-Hinnawi et al., 2005, 2006) and the inferred distribution of the paleochannels (Fig. 7). Two datasets were used to map the paleochannels: (1) radar imagery (C band from Radarsat-

1) that penetrates (up to 50 cm) the dry fine-grained sand sheet in the study area and images the shallow subsurface features (Schaber et al., 1997), and (2) DEM from which the drainage network was extracted. A mosaic was generated from Radarsat-1 tiles over Egypt and Sudan and the major drainage networks were extracted from the DEM applying a high threshold value for the number of cells (50,000 cells) draining towards a downslope cell. The Radarsat-1 mosaic, the extracted drainage network, the delineated THV, and the reported playa deposits are all shown in Fig. 7. Inspection of radar imagery (Fig. 7), visible near-infrared (VNIR) imagery, field observations, and those reported by Kropelin (1993) indicate that: (1) well-developed drainage systems are absent over the Libyan Plateau, and (2) locations of delineated THV mark the onset of drainage systems.

A major west to east paleodrainage pattern was observed on the radar imagery (Fig. 7, dark interconnected channel networks) and in the DEM-derived channels (Fig. 7, blue lines). The source areas for this network are the Gilf Kebir Plateau and Uweinate highlands; one interpretation for the general correspondence between the radar paleochannels and the DEM-derived channels is that the sand sheet cover in these areas modulates, but does not obscure, paleotopography. Similar applications and findings were reported in the study area (Ghoneim and El-Baz, 2007).

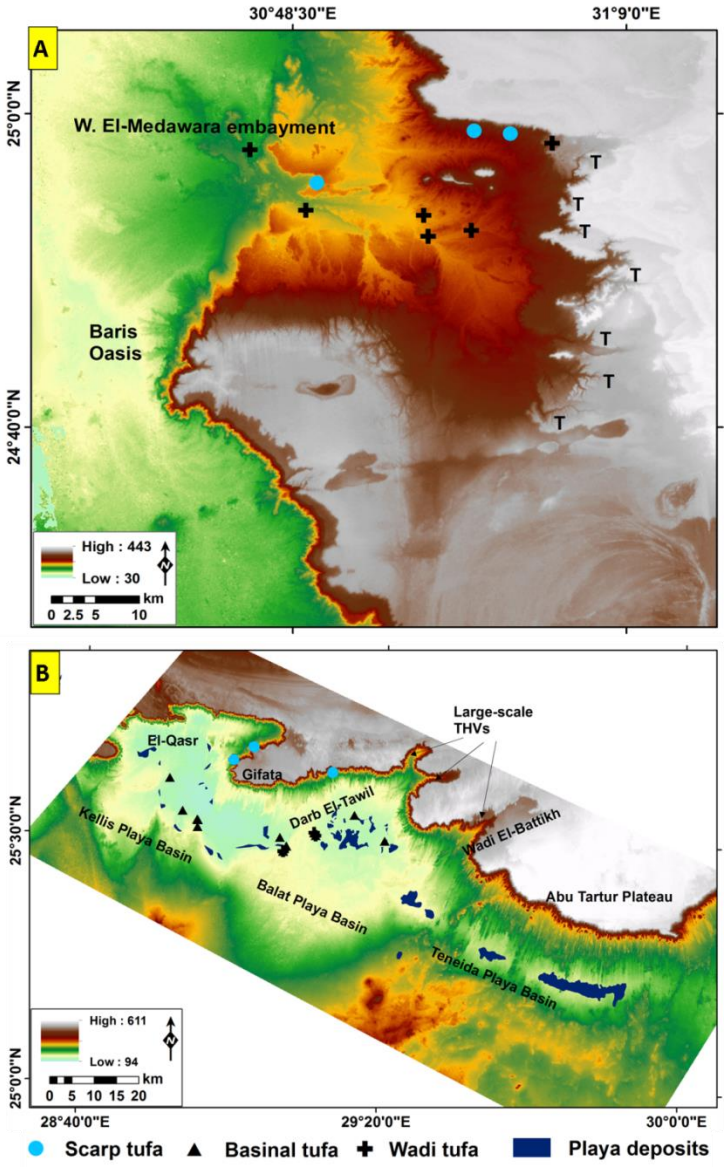

Figure 6. Color-coded digital elevation model showing the spatial correlation between the distribution of THV-rich escarpments and tufa deposits in the Kharga (Wadi El-Midauwara) (Figure 6A) and Dakhla (Figure 6B) depressions. The letter T refers to selected locations of THV. Areas covered by Figure 6A and 6B are outlined by open red boxes 6A and 6B, respectively, on Figure 1.

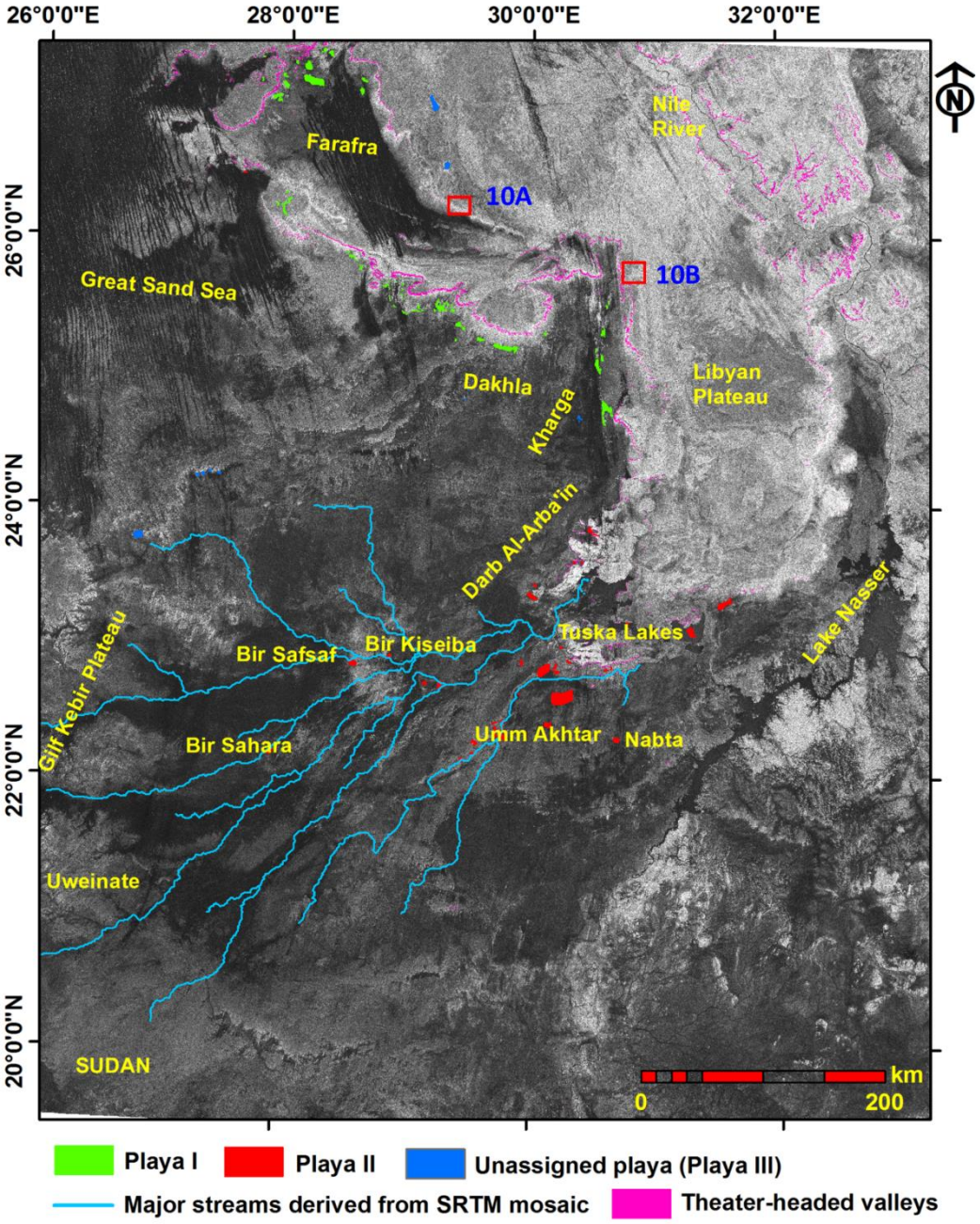

Figure 7. Radarsat-1 mosaic over southwest Egypt and northern Sudan showing the distribution of reported playa deposits (El-Hinnawi et al., 2005), LR-delineated THV, and SRTM-delineated major streams. Area covered by Figure 7 is outlined by open red box 7 on Figure 1.

CHAPTER 4

LANDSCAPE ANALYSIS OF SELECTED GEOMORPHOLOGICAL SITES IN THE NSAS

Additional insights into the origin of THV and natural depressions within the limestone Libyan Plateau and associated denudational landforms were gained from the landscape analysis of four selected geomorphological sites (Fig. 1) in the Qattara, Kharga, Farafra, and Dakhla depressions. The LR model results indicate abundant distribution of THV along escarpments in these locations. The published geological and structural datasets were compiled in a GIS environment, together with remote sensing data and field observations, to investigate the geologic and topographic characteristics of these locations. The studied sites display striking similarities in their geologic and topographic characteristics: (1) minimal contribution of the Libyan Plateau drainage systems (i.e. exorheic streams) into the depressions, (2) high structural control, (3) strong-over-weak stratigraphy, and (4) abundant denudational landforms and tracers for groundwater activity.

4.1 Minimal Contribution of the Libyan Plateau Exorheic Drainage Systems

Drainage networks over the Libyan Plateau were delineated in areas where THV are prominent, extensive and deeply incised into the depressions-bounding escarpments in the four investigated regions (Qattara, Kharga, Farafra, and Dakhla). The networks were extracted from the DEM by applying a small threshold value for the number of cells (100 cells) draining towards a downslope cell. The extracted

networks were then superimposed over the DEMs (Fig. 8). Inspection of Fig. 8 reveals the following in all investigated areas: (1) the surface of the Libyan Plateau gently slopes and drains away from the escarpment and, (2) a minimal contribution of the surface runoff over the Libyan Plateau into the THV and their bounding escarpments was inferred given the limited extension of the catchment areas.

The catchment area for a number of THV in each of the investigated regions was delineated by identifying a snap pour point at a location that is approximately halfway along the valley's length (Fig. 8), and then calculating the upstream contributing area using flow accumulation algorithms (Tarboton, 1997; Teng et al., 2008). Conservative estimates for the eroded volume of these valleys were derived by first projecting the surface of the Libyan Plateau to its pre-incision location and then calculating the volume of rocks subtended between the projected surface and present-day DEM (Giaconia et al., 2012). The adopted methodology yields minimum estimates for the eroded rocks (Bellin et al., 2014). These findings reveal small upslope contributing areas (range: 4.21 to 43.2 km^2) and considerable erosion (volume eroded material: 2.8×10^7 to 259×10^7 m^3) when compared to THV that were generated by megafloods elsewhere (upslope contributing area: 228 to 4713 km^2; volume eroded material: 9.2×10^6 to 1.46×10^7 m^3; Lamb et al., 2008; Table 3).

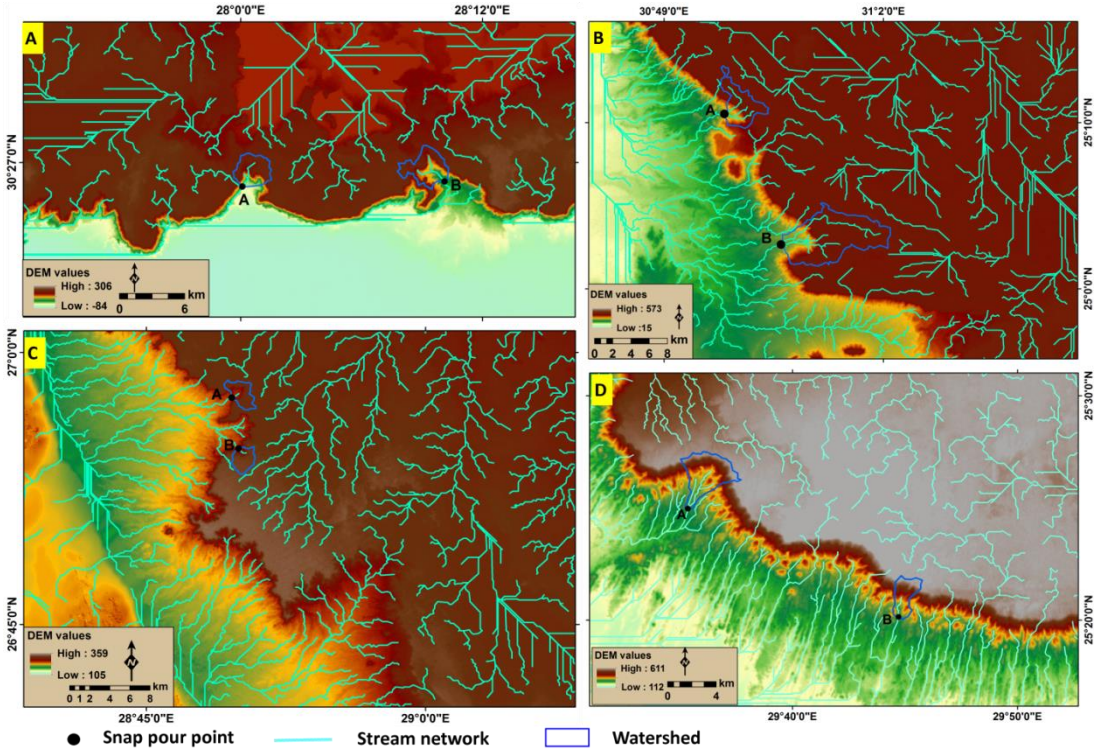

Figure 8. Delineated stream networks over the THV-rich escarpments and the Libyan Plateau showing minimal contribution of plateau surface runoff to depressions and their bounding escarpments in the Qattara (Figure 8A), Kharga (Figure 8B), Farafra (Figure 8C), and Dakhla (Figure 8D) depressions. Areas covered by Figure 8A through 8D are outlined by red boxes 8A through 8D, respectively on Figure 1.

Table 3. Upslope contributing areas and minimum eroded volume of selected THVs in the Sahara and in the Snake River Plain, Idaho, USA

Valley name	Minimum eroded volume	Contributing area	Notes
Box Canyon	$1.46 \times 10^7\ m^3$	$228\ km^2$	Lamb et al., 2008
Blind Canyon	$9.2\ x10^6\ m^3$	$4713\ km^2$	Lamb et al., 2008
Qattara valley (a)	$151 \times 10^7\ m^3$	$7.03\ km^2$	
Qattara valley (b)	$225 \times 10^7\ m^3$	$8.73\ km^2$	
Farafra valley (a)	$29.6 \times 10^7\ m^3$	$4.92\ km^2$	
Farafra valley (b)	$2.8 \times 10^7\ m^3$	$4.21\ km^2$	
Kharga valley (a)	$61.6 \times 10^7\ m^3$	$13.89\ km^2$	
Kharga valley (b)	$164 \times 10^7\ m^3$	$43.2\ km^2$	
Dakhla valley (a)	$259 \times 10^7\ m^3$	$10.57\ km^2$	
Dakhla valley (b)	$20.7 \times 10^7\ m^3$	$4.62\ km^2$	

4.2 High Structural Control

This section demonstrates that structural control on the THV in the Sahara can be recognized on two levels. On the regional scale, major, sub-vertical, deep-seated fault systems act as conduits for ascending groundwater, provide opportunities for surface or near-surface discharge, and create a free face that could develop into an escarpment with progressive dissolution and/or denudation of the faulted blocks (Laity, 1988; Luo et al., 1997). On the local scale, fracture systems exert substantial control over the distribution and geometry of the THV. Often the case the THV propagate preferentially along existing fracture planes that represent zones of weakness (Laity and Malin, 1985).

Field observation in the Western Desert in general, and in the four geomorphological sites in particular, together with inspection of Google Earth images, geological maps (Klitzsch et al., 1987; El-Hinnawi et al., 2005, 2006), and 2D and 3D seismic profiles (Wescott et al., 2011) reveal two prominent—yet poorly understood—fault systems across large sectors of the Western Desert. The first is a northeast-southwest to east-west trending system that could be part of the Pelusium System, a major transcurrent Precambrian fault system that witnessed periodic activities throughout the geologic record (Neev et al., 1982). It runs subparallel to the eastern margin of the Mediterranean, curves northeast-southwest across central Africa, and extends from the Nile Delta to the Niger Delta (Neev and Hall, 1982).

The second trend is a northwest-southeast fault system that is interpreted here as possibly being reactivated Najd faults. The Najd is the largest Proterozoic

transcurrent fault system on Earth (Stern, 1985). It extends for 1200 km in outcrop in the Arabian Peninsula and for an additional 800 km under the sedimentary cover, making a potential total length in excess of 2000 km (Brown and Coleman, 1972). Using a pre–Red Sea rift reconstruction, together with field, geochemical, and geochronological data, Sultan et al. (1988and 1993) mapped the extension of the Najd shear system of the Arabian Shield into the basement complex of the Central Eastern Desert of Egypt. This system is supposed to extend at depth under the sedimentary cover in the Eastern and Western Deserts.

As is the case with many of the Najd faults in the Eastern Desert that were reactivated by dip slip movement during the Red Sea opening (Sultan et al., 2011; Abotalib and Mohamed, 2013), similar movements could have occurred on these faults in the Western Desert. Additional structural trends include the east-west trending Kalabsha dextral faulting in southern parts of the Western Desert (Issawi, 1982; Rayan et al., 2010) and the east-west trending Syrian arc folding and faulting tectonics in the northern parts of the Western Desert (Guiraud and Bosworth, 1997; Kuss et al., 2000). The above-mentioned systems include deep-seated faults (Guiraud and Bosworth, 1997; Saleh, 2011) that witnessed one or more episodes of movement throughout their geologic history (Moustafa, 2002; AlFarhan et al., 2006). Many of these faults could be acted as conduits for ascending Nubian groundwater.

Spatial correlation (in a GIS environment) of the distribution of THV and the escarpments with the distribution of deep-seated structures in the Western Desert (Fig. 9) extracted from over 700 wells, 2D and 3D seismic profiles (Wescott et al., 2011),

satellite and field-based regional structures (Neev et al., 1982; Klitzsch et al., 1987; El-Hinnawi et al., 2005, 2006) revealed the following. First, the boundaries of the Qattara depression, especially the northern Qattara escarpment, are highly dissected by THV; the extension of the northern escarpment correlates largely with the distribution of deep-seated northeast-southwest trending faults, and to a lesser extent with the northwest-southeast trending faults, suggesting a causal effect (Fig. 9A). Second, numerous THV and tufa deposits are observed along Wadi El-Medawara embayment in the Kharga depression; the wadi is bounded by deep-seated, east-west trending faults as evidenced by gravity and borehole data (Zaher et al., 2009) that displaced underlying successions including the basement (Hermina, 1990; Thurmond et al., 2004) (Fig. 9B). Third, the western, eastern, and northern escarpments of the Farafra depression are highly dissected by THV and are apparently controlled by the distribution of deep-seated northeast-southwest and northwest-southeast fault systems (Klitzsch et al., 1987; El-Hinnawi et al., 2006; Sanz-Montero et al., 2013) (Fig. 9C).

Fourth, the distribution of large-scale THV in the Dakhla depression (Fig. 9D) is correlated with the distribution of major faults (northeast-southwest and to a lesser extent by northwest-southeast trending faults; El-Hinnawi et al., 2005). Often, it is the case that where these faults intersect the escarpment, embayments and promontories are formed along the extension of these faults, as with Wadi El-Battikh and Darb El-Tawil (Fig. 9D). Fifth, the structural control over the distribution of the THV is observed on the local level as well. For example, in the Farafra (Fig. 10A) and the

Kharga (Fig. 10B) depressions the THV have apparently propagated along northwest-southeast and northeast-southwest trending structural discontinuities, respectively.

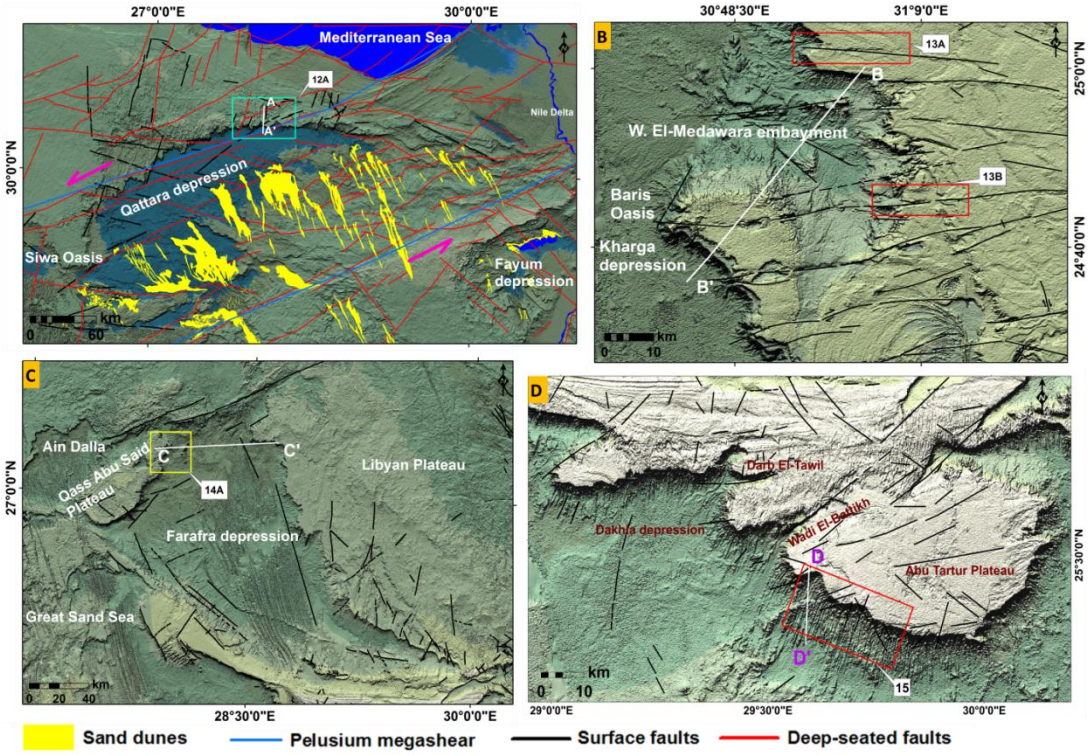

Figure 9. Distribution of major fault traces, deep-seated faults, and the Pelusium meagashear system (Klitzsch et al., 1987; El-Hinnawi et al., 2005, 2006; Wescott et al., 2011) in the Qattara (Figure 9A), Kharga (Figure 9B), Farafra (Figure 9C), and Dakhla (Figure 9D) depressions plotted on hillshade images. Areas covered by Figures 9A through 9D are outlined by open red boxes 9A through 9D, respectively, on Figure 1. Also shown are locations at which detailed geomorphological studies and stratigraphic cross-sections were conducted in the Qattara (Figures 1, 9A: box 12A, line A-A′), Kharga (Figures 1, 9B: boxes 13A and 13B, line B-B′), Farafra (Figures 1, 9C: box 14A, line C-C′), and Dakhla (Figures 1, 9D: box 15, line D-D′) depressions.

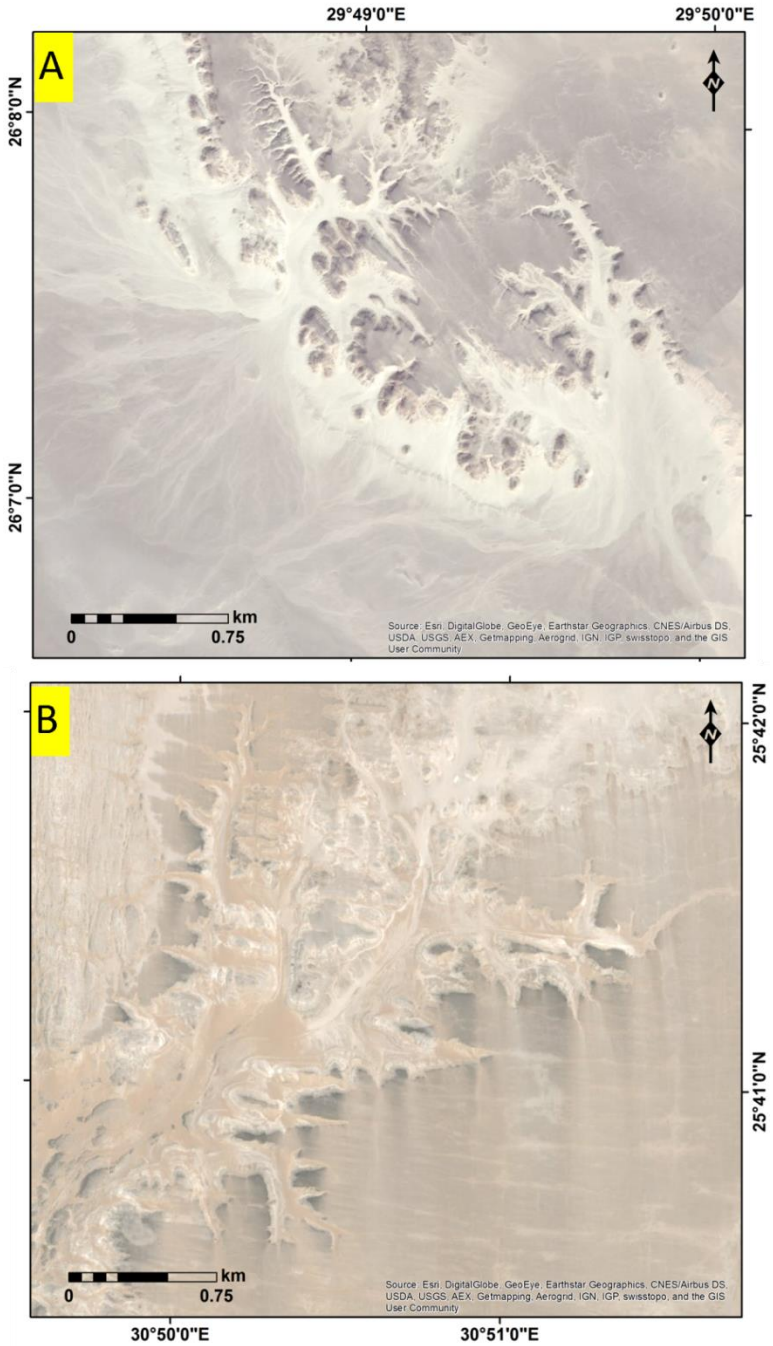

Figure 10. Local structural control on the spatial distribution of THV in the Farafra (Figure 10A) and Kharga (Figure 10B) depressions. Areas covered by Figures 10A and 10B are outlined by open red boxes 10A and 10B, respectively, on Figures 1 and 7.

4.3 Strong-Over-Weak Stratigraphy

Four stratigraphic cross-sections were constructed (Fig. 11) across the selected sites using available geological datasets (Klitzsch et al., 1987; Hermina, 1990; Churcher et al., 1999; El-Hinnawi et al., 2005, 2006), elevation data, and field observations to investigate the morpho-stratigraphic relationships in these locations. The four sites are all characterized by strong massive limestone, capping soft, easily eroded shale and argillaceous sandstone. The Qattara depression (Figs. 9A and 11A; A-A′) is excavated in sedimentary rocks of Tertiary age, including the lower Miocene Moghra Formation and the middle Miocene Marmarica Formation (Said, 1962). The Moghra Formation is mainly composed of sandy and clayey beds, whereas the overlying Marmarica Formation composition ranges from pure limestone to shaly limestone and marl (Said, 1962). Further south, in the deepest region of the depression, the black shale of the Upper Eocene–Oligocene Dabaa Formation is exposed (Aref et al., 2002).

The Kharga depression (Figs. 9B and 11B; B-B′) is floored by Upper Cretaceous Quseir and Duwi Formations and the Upper Cretaceous–Paleocene Dakhla Formation. These sedimentary formations are mainly composed of vari-colored shale and siltstone with calcareous marl, phosphorite, and fine-grained sandstone inter-beds (Hermina, 1990). The embayment of Wadi El-Medawara is floored by the greenish-gray shale of the Paleocene-Eocene Esna Formation (El-Hinnawi et al., 2005). Along the scarp face, the Paleocene fossiliferous and chalky limestone of the Kurkur and Tarawan Formations and the underlying Dakhla Formation are exposed. The surface of

the plateau is covered by marine carbonate formations ranging from the Paleocene Garra Formation to the Oligocene Katkut Formation.

The Farafra depression (Figs. 9C and 11C; C-C′) is floored by Upper Cretaceous Khoman and Paleocene Tarawan Formations. The Khoman Formation consists of snow-white to light gray chalky limestone in the northern part of the depression, which gives way to dark gray shale of the Dakhla Formation in the south (Klitzsch et al., 1987; El-Hinnawi et al., 2005). The Tarawan Formation is composed of snow-white chalky limestone that is more compact and harder than the underlying Khoman Formation (El-Hinnawi et al., 2005). Escarpment around the depression is made up of the Upper Paleocene and lower Eocene sequences of the Esna and Farafra Formations, respectively (Hermina, 1990). The Esna Formation occupies the lower part of the escarpments and consists of soft green shale intercalated with marl beds, whereas the Farafra Formation caps the escarpment with argillaceous limestone followed upward by snow-white limestone (Said, 1962). The Dakhla depression (Figs. 9D and 11D; D-D′) is covered by Upper Cretaceous Nubia Group including the Taref Sandstone Formation, the overlying Mut claystone, and the Duwi mudstone Formations (Brookes, 2010). The escarpment of the Abu Tartur Plateau is composed of the Upper Cretaceous–Paleocene Dakhla Formation capped by Paleocene Kurkur and Garra Formations. The Dakhla Formation consists mostly of shale, marl, and clay with calcareous and sandy intercalations (Hermina, 1990); the Kurkur and Garra Formations consist of massive thick-bedded limestone.

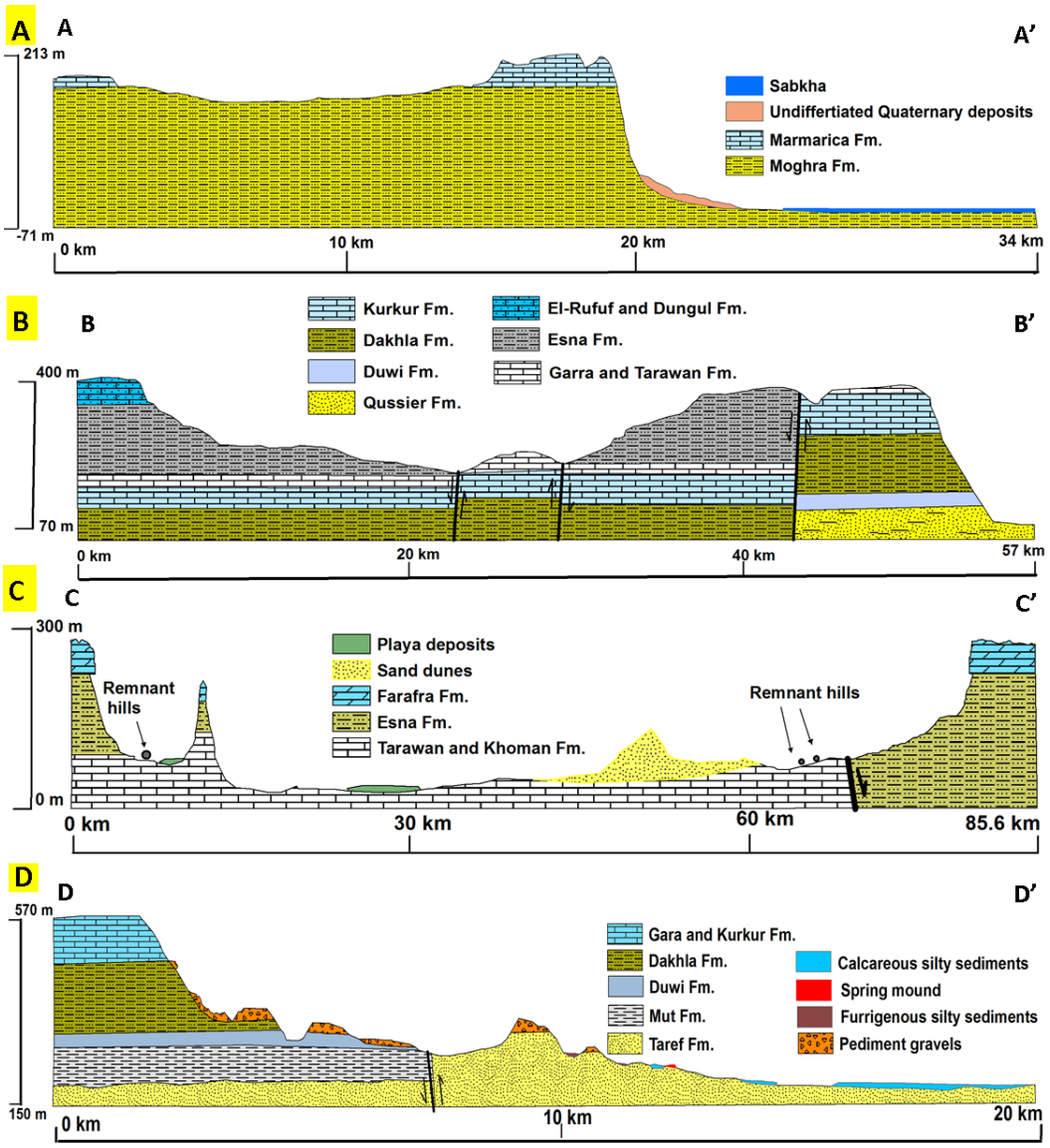

Figure 11. Simplified stratigraphic cross-sections across the selected four sites, including the Qattara (Figure 11A), Kharga (Wadi El-Medawara; Figure 11B); Farafra (Figure 11C), and Dakhla (Figure 11D) depressions showing the strong-over-weak stratigraphy. Stratigraphic data was extracted from Klitzsch et al. (1987), Hermina (1990), and El-Hinnawi et al. (2005, 2006). The cross sections were constructed along transects A-A′, B-B′, C-C′, and D-D′ shown as solid lines on Figures 1 and 9.

4.4 Abundant Denudational Landforms and Tracers for Groundwater Activity

Field investigations, together with remote sensing–based landscape analysis (Figs. 12 through 16) were conducted in the Qattara, Kharga, Farafra, and Dakhla depressions in search of denudational landforms that are associated with, and indicative of, groundwater activity. Figs. 12A, 14A, and 15 are 3D models covering the Qattara, Farafra, and Dakhla depressions, respectively. Figs. 13A and 13B are merged Landsat 8 images (spatial resolution: 15 m) for Wadi El- Medawara embayment. Fig. 12B is a merged ALI image (spatial resolution: 10 m) for the Qattara escarpment. Figs. 14B, 14C, and 16 are field shots from the Farafra and Qattara depressions. Inspection of Figs. 12 through 16 indicates that the investigated sites share many denudational landforms. These include, first, drainage systems that over the bounding limestone Libyan Plateau are minimal to absent, whereas the scarp faces are intensively incised by THV in all four sites. Second, there are THV and sink holes that originate at, and propagate along, major faults; examples include THV and sink holes along the east-west trending escarpment of Wadi El-Medawara embayment (Figs. 13A and 13B) and the sink holes in the northern Qattara depression that developed along a northeast-southwest trending fault that runs parallel to the scarp rim (Wescott et al., 2011) (Fig. 12A). Third, endorheic streams begin at the boundary between the strong and underlying weak rock units. In the Qattara depression, endorheic streams emerge at the boundary between the Marmarica limestone Formation and underlying sandy member of Moghra Formation, and/or between the sandy and shaly members of the Moghra Formation, (Fig. 12B). In the Dakhla depression, they emerge at the boundary between

the Garra and/or Kurkur limestone Formations and underlying Dakhla shale Formation (Fig. 15). Fourth, widespread playa deposits are found at the terminations of endorheic streams (e.g., Farafra and Dakhla depressions; Figs. 14 and 15). Lastly, the removal of large thicknesses of rock sequences by groundwater discharge during wet periods and by aeolian processes in the interleaving dry periods (Aref et al., 2002). Analysis of digital elevation data along transects A-A′ and B-B′ in Fig. 11 showed that the incision of THV in each of the Qattara and Kharga depressions resulted in the removal of large thicknesses (up to 200 m) of the rock sequences.

Each of the investigated areas has its own peculiar denudational landforms and features. For example, in the northern Qattara depression (Fig. 12), the following was observed: (1) the erosional processes removed the limestone cap rock of the Marmarica Formation and exposed the underlying shaly sandstone of the Moghra Formation within sink holes and excavated THV; (2) extensive inland sabkhas located in scarp-foot depressions, possibly where the groundwater table intersected the land surface in previous wet periods; and (3) abundant features related to extensive salt weathering including tafoni, block disintegration, gypsum veins cutting through stratigraphic sequences, polygonal halite and flaky gypsum crusts, and salt quarries (Fig. 16). These field and remote sensing observations in Qattara are consistent with an elevated groundwater table during the previous wet climatic periods in the Sahara that caused intensive salt weathering, erosion, and removal of the limestone caprock and the formation of THV and sinkholes.

In Wadi El-Medawara, the abundance of the structurally controlled THV, sinkholes, and tufa deposits within the valleys (Figs. 9B and 13) are consistent with a model that calls on artesian upward leakage from the underlying NAS along deep-seated faults, causing erosion of the plateau, formation of the embayment, and deposition of tufa. This model is supported by the work of Smith et al. (2004a, 2004b), who advocated extensive groundwater activity along Wadi El-Medawara based on the wide distribution of tufa deposits over the Paloecene-Eocene units (Smith et al., 2004a, 2004b) and that of Luo et al. (1997) who reported numerous structurally controlled, groundwater sapping-related THV from El-Rufuf Pass, some 80 km to the north.

Investigations of the Farafra depression revealed abundant denudational and dissolution landforms and remnant hills (e.g. pinnacles, limestone towers, and inselbergs) and sub-parallel ridges (e.g. interfluves) that originate at scarp foothills and extend away from it across a pediment surface. These relationships are observed locally on a 3D model (Fig. 14A) for the Qass Abu Said Plateau at the northwestern corner of the Farafra depression and regionally on Google Earth Digital Globe imagery and Radarsat-1 images (Fig. 7). Along the western escarpment of the Farafra depression, a wide (width: 2.5 km) pediment is observed with extensive west-to-northwest trending subparallel ridges (average height: 3 m; average width: 50 m) separated by interleaving endorheic streams. The ridges originate at, or are proximal to, the scarp face, and transition into a series of rounded remnant hills along their extension away from the scarp face (Figs. 14B and 14C). The origin of these rounded hills was attributed to expulsion of formation water along layer-bounded polygonal fault systems in the

Khoman Formation and subsequent preferential fluvial and aeolian erosion along the faulted and fractured surfaces (Tewksbury et al., 2014). Field observations and analysis of satellite images indicate that these rounded features are bounded by two of the dominant fault systems of the Western Desert, the northwest- and northeast-trending faults, suggesting a causal effect. The present study suggests an alternative, yet similar hypothesis: rising groundwater during previous wet climatic periods accessed deep-seated faults and fractures, fluvial and later aeolian erosion along planes of weakness shaped the landscape giving rise to THV at the scarp face, subparallel ridges separated by interleaving endorheic streams, and a series of rounded remnant hills along their extension transitioning away from the scarp.

Examination of a 3D model for the Teneida playa basin and Abu Tartur escarpment in the Dakhla depression reveals that small-scale THV or gullies are subdivided in three segments head alcoves, channels, and depositional aprons (Fig. 15). The head alcoves are eroded depressions along the side of a cliff or scarp face, and the depositional aprons are, wedge-shaped features located at the bottom of a hillside; the aprons comprise colluvial and slope wash processes sediments, cut through Pleistocene slumping colluvium along the scarp rampart and terminate in playas at the scarp-foot depression (also see Fig. 6). Detailed field studies identified the slumping colluvium as gravel deposits formed along the scarp ramparts by cliff-sapping of the limestone caprock (Churcher et al., 1999; Kieniewicz and Smith, 2009; Brookes, 2010). The landforms described here bear striking similarities to those observed on the surface of

Mars (Malin and Edgett, 2000), which are believed to have been formed by subsurface fluid seepage, followed by surface runoff along slope surfaces.

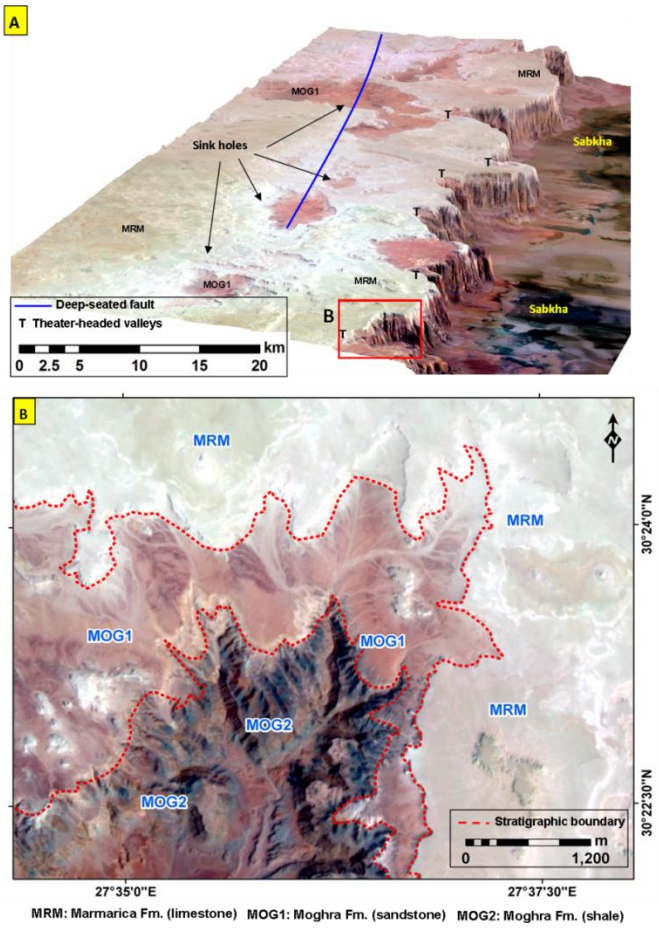

Figure 12. Denudational landforms along the northern Qattara escarpment. (A) 3D model showing the extensive distribution of THV along the scarp face and the presence of sink holes on the plateau and their alignment with an identified deep-seated fault (Wescott et al., 2011); (B) High-resolution (spatial resolution: 10 m) ALI image for the area outlined by box B in Figure 12A showing the emergence of streams at the contact between the limestone Marmarica Formation and underlying sandy member of Moghra Formation, or between sandy and shaly members of the Moghra Formation. The area covered by Figure 12A is outlined by open box 12A on Figs. 1 and 9, and letter "T" marks the location of selected THV.

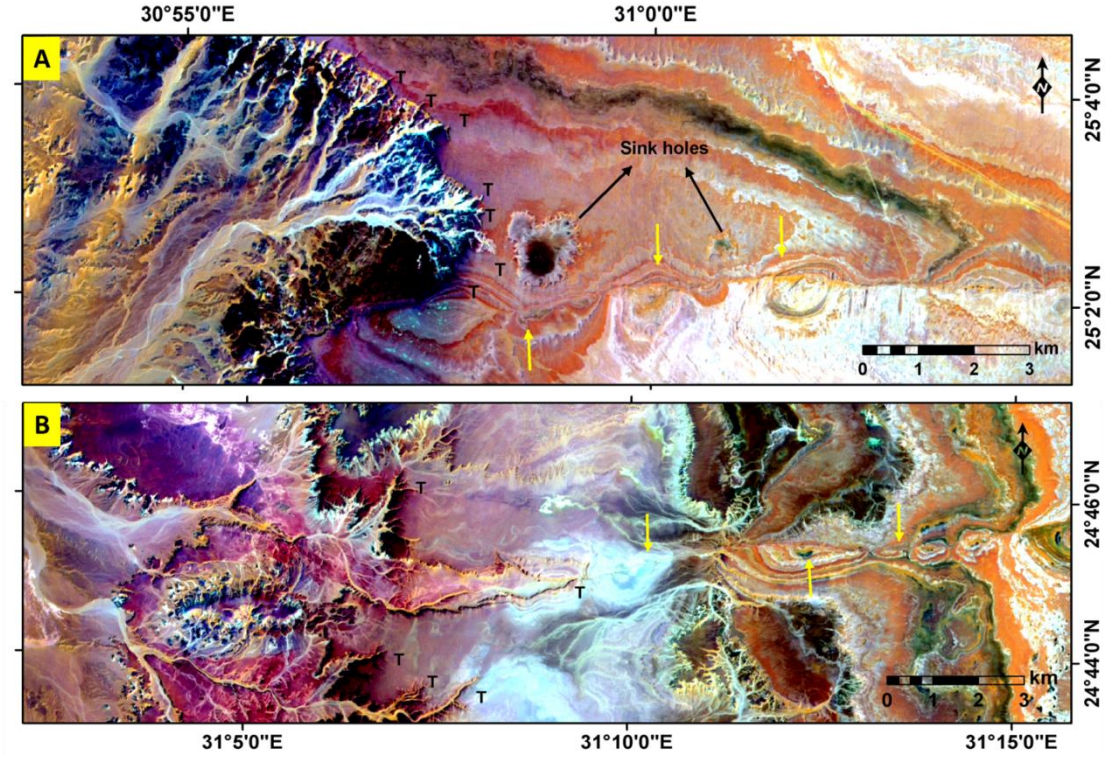

Figure 13. Denudational landforms in the Kharga depression (Wadi El-Medawara embayment). (A) Merged Landsat 8 image showing the distribution of sinkholes along an east-west trending fault (*yellow arrows*) that is part of the Seyal fault system. (B) Merged Landsat 8 image showing the origination and propagation of THV (marked with letter "T") along a major east-west trending fault that belongs to the Seiyal fault system (Jerris, 2014). Areas covered by Fig. 13A and 13B are outlined by open boxes 13A and 13B, respectively, on Figures 1 and 9.

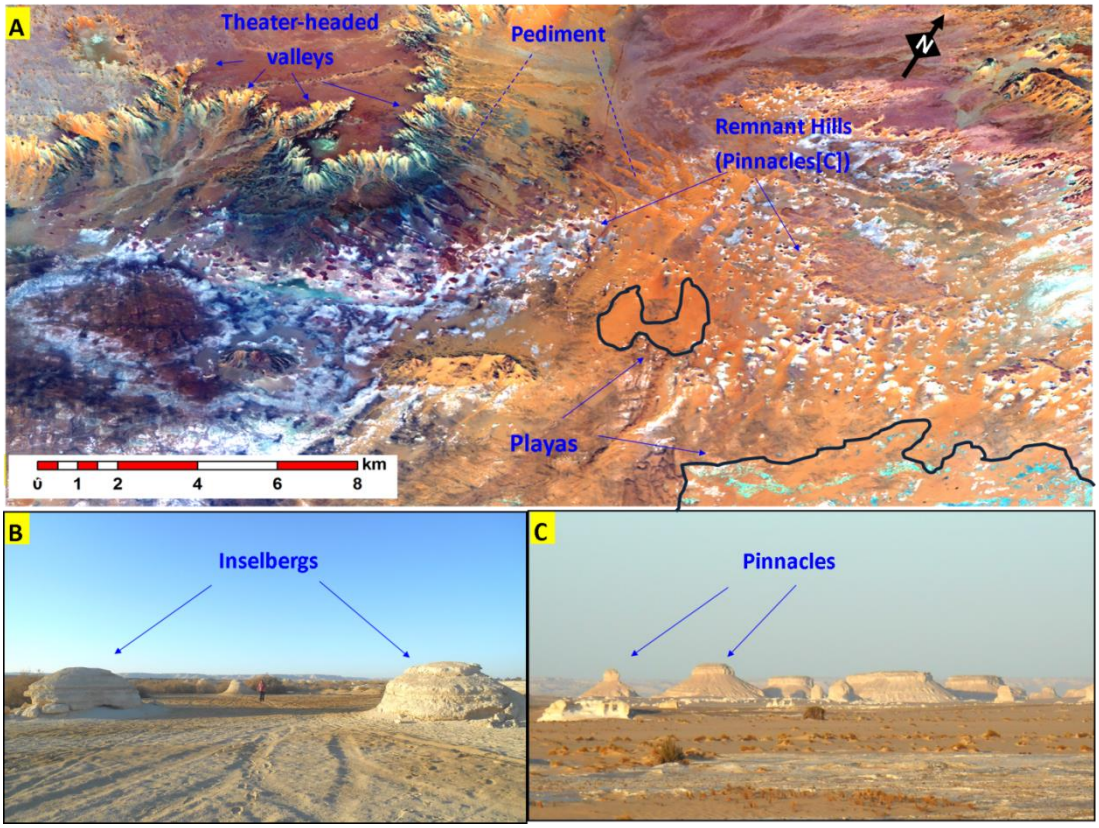

Figure 14. Denudational landforms in the Farafra depression. (A) 3D model for the northwestern escarpment at Qass Abu Said Plateau showing the distribution of denudational and dissolution landforms. (B) Rounded remnant hillocks (inselbergs) of playa deposits in Ain El-Raml area (Figure 1). (C) Rounded remnant hills (pinnacles) of the chalky limestone Khoman Formation. Area covered by Figure 14A is outlined by open box 14A on Figures 1 and 9.

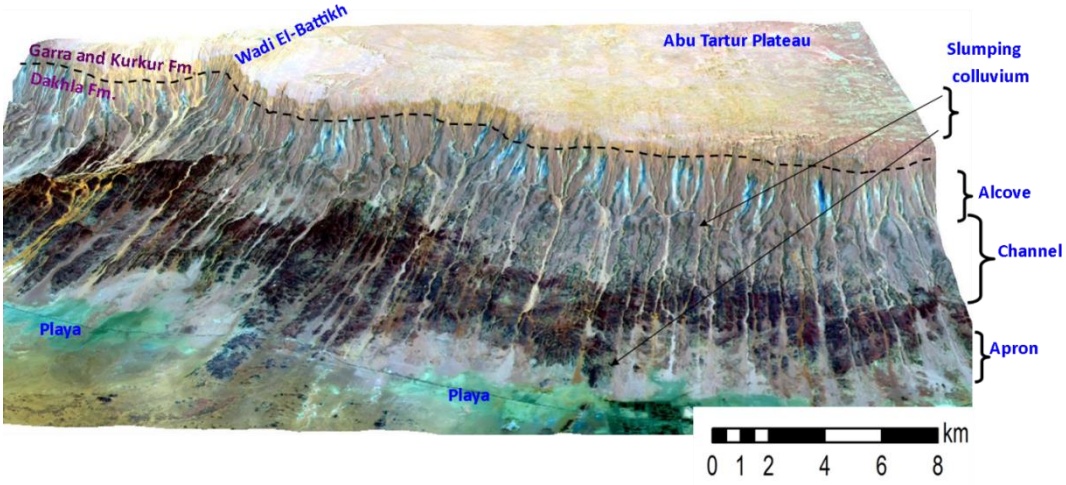

Figure 15. Three-dimensional model of Teneida playa basin and Abu Tartur Plateau showing the characteristics of THV emanating from Abu Tartur scarp face. Area covered by Figure 15 is outlined by open box 15 on Figures 1 and 9.

Figure 16. Features related to salt weathering in the Qattara depression. (A) Tafoni landform in the Moghra sandstone Formation; (B) block disintegration of the of the Moghra sandstone and spalling of the underlying evaporite vein–rich Moghra shale; (C) halite and gypsum veins cutting through the Moghra shale; (D) gypsum flakes at the boundary between the Moghra sandstone and shale; (E) polygonal-shaped halite crust; (F) ongoing salt quarrying from the sabkha.

4.5 Remnant Hills in the Farafra Depression: Polygonal Fault-related or Denudational Features

Using field observations and inferences from Google Earth images, Tewksbury et al. (2014) reported the discovery of the first major on-land surface exposure of fluid escape–related, polygonal fault systems and associated circular features (pockmarks) and vein-filling calcite in the chalky Khoman Formation in the Western Desert of Egypt. Such features are common in modern and ancient marine basins and form early in the burial history of fine-grained sediments due to pore fluid pressure, which may be related to compaction of sediments during burial. Here are four observations that are inconsistent with the presence of escape–related features in the Khoman Formation.

1- Host lithologies. The only common factors in reported examples of layer-bound polygonal fault systems are their deposition in marine environment and their ultrafine-grained texture (Cartwright and Dewhurst, 1998). Inspection of Google Earth images and geologic maps (Klitzsch et al., 1987), indicates that the reported escape-related features are not restricted to the ultrafine-grained marine Khoman Formation (chalk), but they extend in the overlying Tarawan Formation (chalky limestone), the underlying Duwi Formation (limestone, phosphate, and sandstone), and in eight additional limestone formations (Fig.17) with varying depositional environment, texture, and grain size (e.g., reefal, nummulitic, lagoonal, open marine) (Klitzsch et al., 1987). None of the above-mentioned formations is ultrafine in texture.

2- Regional extent/structural geology. In modern and ancient settings where layer-bound polygonal fault systems are identified, the fault systems are regionally extensive and continuous and show large dip slip displacements. For example, in the

North Sea Basin and in the Eromanga Basin, the polygonal fault systems extend across an area exceeding 150,000 km^2 and the reported throw is typically 10-100m (Cartwright and Dewhurst, 1998). Two major outcrops for the Khoman Formation were mapped by Klitzsch et al. (1987). The first is the outcrop (area: 2675 km^2) identified by Tewksbury et al. (2014) and the second (area: 1101 km^2) crops out only a few kilometers to the northeast (Fig. 17). Field observations and inspection of Google Earth images indicate that the polygonal faulting is absent from the northern outcrop. Tewksbury et al. (2014) do not provide convincing structural data to validate the presence of dip slip displacement on the polygonal faults. They report a displacement for a single fault and the throw they report is modest (2-3 m) compared to those observed in typical layer-bound polygonal fault systems.

3- Stable isotope data/fluid sources. Tewksbury et al. (2014) report range and mean isotopic composition for 14 samples (individual analyses were not provided) and interpret these data to indicate an origin involving re-equilibration of formation-generated fluids with isotopically depleted meteoric waters. Alternatively, the reported light isotopic compositions (probably from the calcite veins) could indicate deposition from depleted ($\delta^{18}O$: –10.6 to –11.5‰) Pleistocene NAS groundwater (Sultan et al., 1997). A similar origin was proposed to account for compositionally similar vein-filling calcite and tufa that were deposited during previous wet periods elsewhere in the Western Desert (Sultan et al., 1997; Smith et al., 2004).

4- Detailed field investigation and analysis of satellite imagery in the Farafra depression (refer to section 4.4) indicate that circular features are located downslope

from a 2.5 km wide pediment; the pediment is incised by THV-related endorheic streams leaving behind parallel ridges which gradually transition to the circular features downslope towards the flat basin areas.

The fluid escape-related origin of the remnant hills in the Farafra depression as described in Tewksbury et al. (2014), is inconsistent with the above-mentioned observations and a denudational-related origin is favored given the detailed landscape analysis and the supporting evidence that was provided for the Farafra depression (refer to section 4.4).

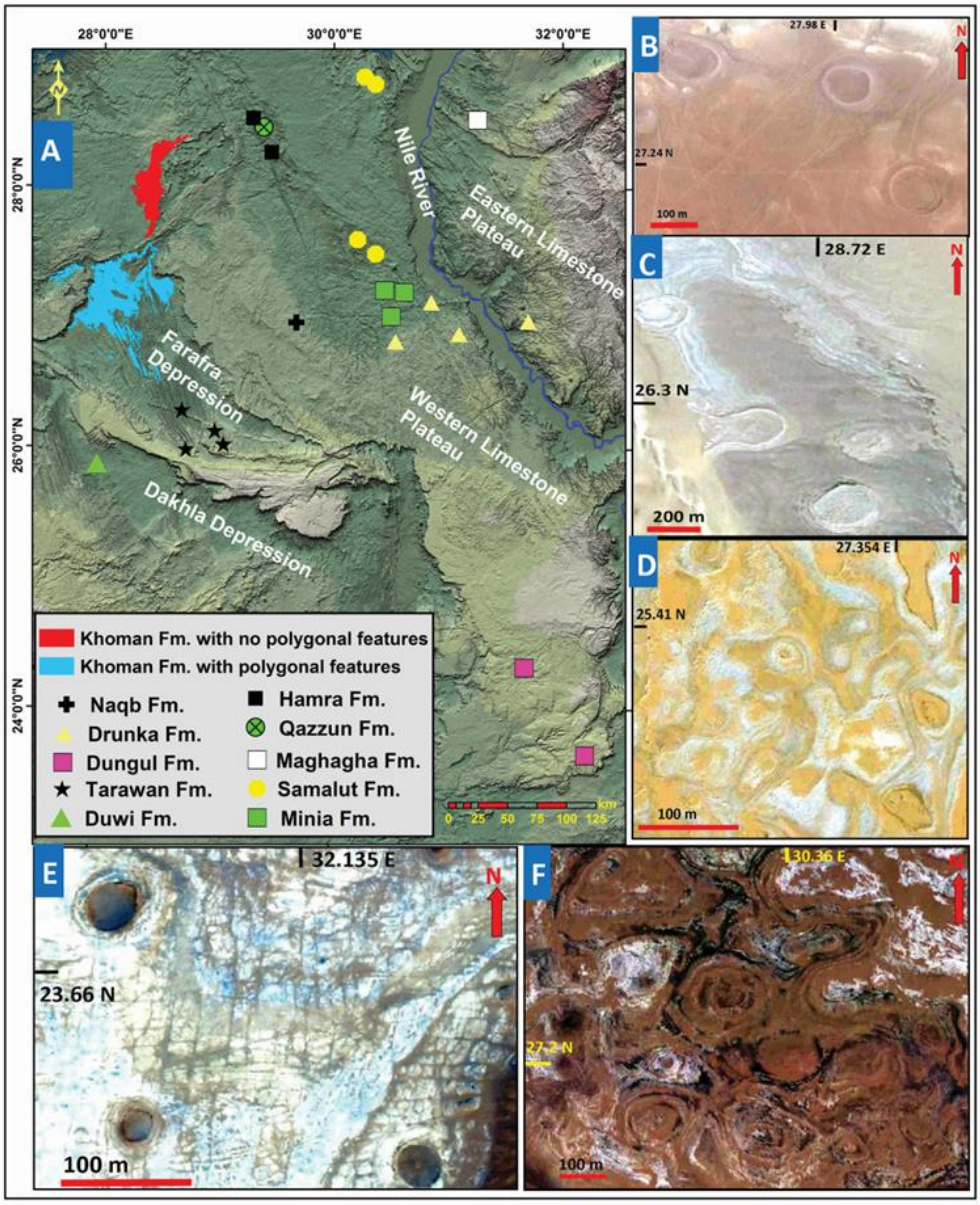

Figure 17. (A) Shaded-relief image showing the distribution of the Khoman Formation (Klitzsch et al., 1987) and locations of circular basins and polygonal features in limestone formations in the Western Desert. Google Earth images showing the circular basins in the (B) Khoman and (C) Tarawan formations, and circular basins bounded by polygonal features in the (D) Duwi, (E) Dungul, and (F) Minia Formations.

CHAPTER 5

LITHOLOGIC AND ISOTOPIC CHARACTERISTICS OF PLAYA AND TUFA DEPOSITS AND GROUNDWATER

5.1 Lithologic Characteristics of Playa Deposits

Inspection of Figs. 3, 6, and 7 indicates that the majority of the reported playa occurrences fall in one of two groups: Group I are found within scarp-foot depressions along linear trends that run parallel and proximal (<25 km) to scarp faces, whereas Group II are distant (>25 km) from the scarp faces and proximal to the west-east trending paleochannel network (Fig. 7). The unclassified playas on Fig. 7 are found in areas where encroaching thick sand sheets obscure field relations that are here used for classification purposes. The aforementioned observations are consistent with the deposition of Group II playas from the west-east trending paleochannel network (Fig. 7) and Group I playas from spring waters emerging from the Libyan Plateau escarpments, a suggestion that is supported by the lithologic and isotopic composition of Groups I and II.

Group I playa deposits are characterized by sequences with high carbonate content including intercalated calcareous silty sediments, highly fossiliferous lacustrine marl deposits, fossiliferous authigenic calcite silts, calcareous playa mud deposits, and massive limestone sequences, whereas Group II playa deposits are largely composed of beach gravels, aeolian sand, clay, non-calcareous medium sand, and siliceous mud; authigenic chemical precipitates are absent. Group I playa sequences were reported from the Dakhla depression (Churcher et al., 1999; Kieniewicz and Smith, 2009;

Brookes, 2010), Wadi El-Midawara in the Kharga depression (Kieniewicz and Smith, 2007), from Abu Nuss, Ain El-Raml, Bahr, Sheikh El-Obeiyid, and the Bir-Karawein area in the Farafra depression (Hassan et al., 2001; Wanas, 2012; Hamdan and Lucarini, 2013). Group II deposits were reported from the Nabta (Wendorf and Schild, 1980), Bir Kiseiba (Wendorf et al., 1984), Bir Sahara (Szabo et al., 1995), Umm Akhtar (Nicoll, 1998), Darb Al-Arba'in (Haynes, 2001), and Bir Safsaf palyas (Fig. 3; Paillou et al., 2003).

The high carbonate content and relatively high $\delta^{13}C$ (range $\delta^{13}C$: −2.19 to 0.2‰) of the inorganic deposits of Group I playa in the Farafra, Kharga, and Dakhla depressions are consistent with dissolution of limestone by spring waters emerging from the Libyan Plateau escarpment and re-precipitation of calcite within proximal playas (Kieniewicz and Smith, 2007; Kieniewicz and Smith, 2009; Wanas, 2012). Differences in pattern of distribution, distance to escarpments and major streams, calcium carbonate content, and $\delta^{13}C$ values point to differences in water sources between the spring-fed Playa I (Group I) and river-fed Playa II deposits (Group II).

5.2 Isotopic Analysis of Tufa Deposits

The following steps were conducted to test whether the isotopic composition of the tufa deposits is consistent with deposition from NSAS fossil groundwater. First the reported isotopic compositions (Crombie et al., 1997; Sultan et al., 1997; Smith, 2001; Jimenez, 2014) of tufa deposits (147 samples) collected from five localities (Crystal Mountain, Farafra depression, Kharga depression, Kurkur Oasis, and Dakhla

depression; Fig. 3) in the Western Desert were compiled and these compositions were used to derive the isotopic composition ($\delta^{18}O$) of groundwater from which these tufa were deposited. This investigation followed the procedures described in Friedman and O'Neil (1977) for the fractionation of ^{18}O between $CaCO_3$ and water under equilibrium conditions:

$$1000 \ln\alpha = 2.78(10^6 T^{-2}) - 2.89 \quad (7)$$

$$\alpha = (1000 + \delta^{18}O_{calcite})/(1000 + \delta^{18}O_{water}) \quad (8)$$

Where α is the fractionation factor, T is the prevailing paleomean annual air temperature (MAAT, in Kelvin) during calcite deposition from spring water, $\delta^{18}O_{calcite}$ is the isotopic composition of the tufa, and $\delta^{18}O_{water}$ is the isotopic composition of the tufa-depositing groundwater. The average value (19.8 °C) for the reported (Abouelmagd et al., 2014) noble gas recharge temperatures (NGRT; range: 17.5–22.0 °C) for fossil groundwater from the NSAS in Sinai was used as a proxy for the MAAT.

The composition of the majority of the tufa (118 samples; 80% reported analyses) are consistent with deposition from depleted Nubian waters (range $\delta^{18}O$: −12.8 to −8.0‰) (Patterson et al., 2005). Few samples (29 samples) yield more enriched water compositions (range $\delta^{18}O$: −7.9 to −3.9‰); such enrichments could be attributed to evaporation, degassing, and kinetic effects (Smith et al., 2004a).

Findings pertaining to the origin of tufa deposits by natural discharge are consistent with those advocated by Nicolle et at al., (1999); they stated that topographic locations, structural morphologies (e.g., wedge-shaped slopes and broad sheets), mineralogical composition (e.g., very high calcite [>90 mol %] and very low $MgCO_3$[<1.2 mol %]), and organo-sedimentary laminations of tufa deposits from different localities near the Kharga depression is indicative of precipitation by processes operating within freshwater spring-fed alkaline stream environments during pluvial Quaternary periods.

5.3 Isotopic Analysis of Groundwater Samples

The main water-bearing horizons in the north Western Desert include six aquifers: the NAS, the carbonate aquifer, the Oligocene aquifer, the Miocene Moghra aquifer, the Pliocene Wadi El-Natrun aquifer, and the Quaternary aquifer (RIGW, 1992). The Oligocene, Miocene, Pliocene, and Quaternary aquifers in the study area (Fig. 18A) are hydrologically connected and are considered as one hydrological unit (REGWA, 1990), hereafter referred to as the Oligocene Miocene Pliocene Quaternary (OMPQ) aquifer. The NAS is separated from these aquifers by the Paleocene-Eocene carbonate aquifer (RIGW, 1992). The NAS was recharged by direct precipitation over its outcrops in southern Egypt and northern Sudan from an Atlantic moisture source during the Pleistocene pluvial periods (Sultan et al., 1997; Sturchio et al., 2004).

The OMPQ aquifer is believed to be largely recharged by groundwater flow from the Nile River with contributions from the underlying aquifers (Thompson, 2007;

El-Gamal, 2005), whereas modern recharge from local storms is negligible (<1% total annual recharge) (REGWA, 1990). The suggestion that the OMPQ aquifer is being recharged by groundwater flow from the Nile aquifer is supported by the progressive increase in radiocarbon ages of groundwater samples (31, 33, 61, and 62; Figs. 18B and C) along the general groundwater flow direction (northeast to southwest; RIGW, 1992); samples from the OMPQ aquifer were collected along two northeast-southwest trending transects proximal to, and west of, the Nile Delta (Figs. 18B and C). Similar findings were reported along an east-to-west transect where an increase in groundwater ages was detected from tens of years in areas proximal to the Nile Delta to thousands of years some 100 km to the west of it (Fig. 18D; samples 8 and 10: <30 YBP; sample 25: 9250 YBP); these ages were estimated using SF_6, ^3H-^3He, and ^{14}C dating methods (Aeschbach-Hertig et al., 2007).

Groundwater samples from the Pliocene (six samples), Miocene (four samples), and NAS (10 samples) aquifers were collected and analyzed for O and H isotopic compositions, and the results were compared to reported data (51 samples) from the OMPQ aquifer (Fig. 19). The investigated samples could be classified into four groups on the basis of their isotopic composition. Group I samples were collected from wells tapping the NAS in the Bahariya Oasis, and they have depleted δD and $\delta^{18}O$ values (δD: −84.4 to −80.0‰; $\delta^{18}O$: −10.3 to −11.0‰) similar to those reported from the fossil Nubian groundwater elsewhere (δD: −81 to −72‰; and $\delta^{18}O$: −12.8 to −8.0‰; Sonntag et al., 1978; Sultan et al., 1997; Patterson et al., 2005). Group II samples were extracted from the OMPQ aquifer; their isotopic composition is enriched (δD: −0.7 to 7.2‰;

$\delta^{18}O$: −1.13 to 1.20‰) compared to Group I samples and is similar to that of the pre-High Dam Nile water (δD =−1 to 7.5‰ and $\delta^{18}O$ = −1 to 1.5‰; El-Bakri et al., 1992; Dahab et al., 1999; Sultan et al., 2000) .

Not all of the OMPQ aquifer samples have isotopic compositions similar to those of the pre–High Dam. Many of them (19 samples, hereafter referred to as Group III samples) display a wider range of compositions (δD: −62.6 to −2.6‰; $\delta^{18}O$: −7.0 to −1.09‰); Group III samples are here interpreted as being mixtures of fossil Nubian Group I, pre–High Dam Nile Group II, and post–High Dam (Group IV) end members. The samples from Group IV have the highest δD and $\delta^{18}O$ values (δD: 18.8 to 25.4‰; $\delta^{18}O$: 2.08 to 3.10‰) compared to those of Groups I, II, and III, and were collected from the Quaternary aquifer adjacent to the Nile Delta. Group IV samples show a deviation from the global meteoric water line (GMWL) suggesting evaporation-enrichment relationships for ^{18}O and δD.

Inspection of Figs. 18 and 19 shows that the spatial distribution of Group II and III samples do not depend on the distance from the Nile aquifer water. Some of Group III samples are closer to the Nile aquifer than Group II samples. One explanation for this observation is that the fossil Nubian groundwater ascends along deep-seated fault systems and discharges into the shallower OMPQ aquifer. Artesian upward leakage of the deep Nubian waters into the shallower carbonates and alluvium aquifers along deep-seated structures was also reported in the Gulf of Suez (Sturchio et al., 1996) and in the Eastern Desert of Egypt at Wadi El-Asyuti (Sultan et al., 2007) (Fig.1).

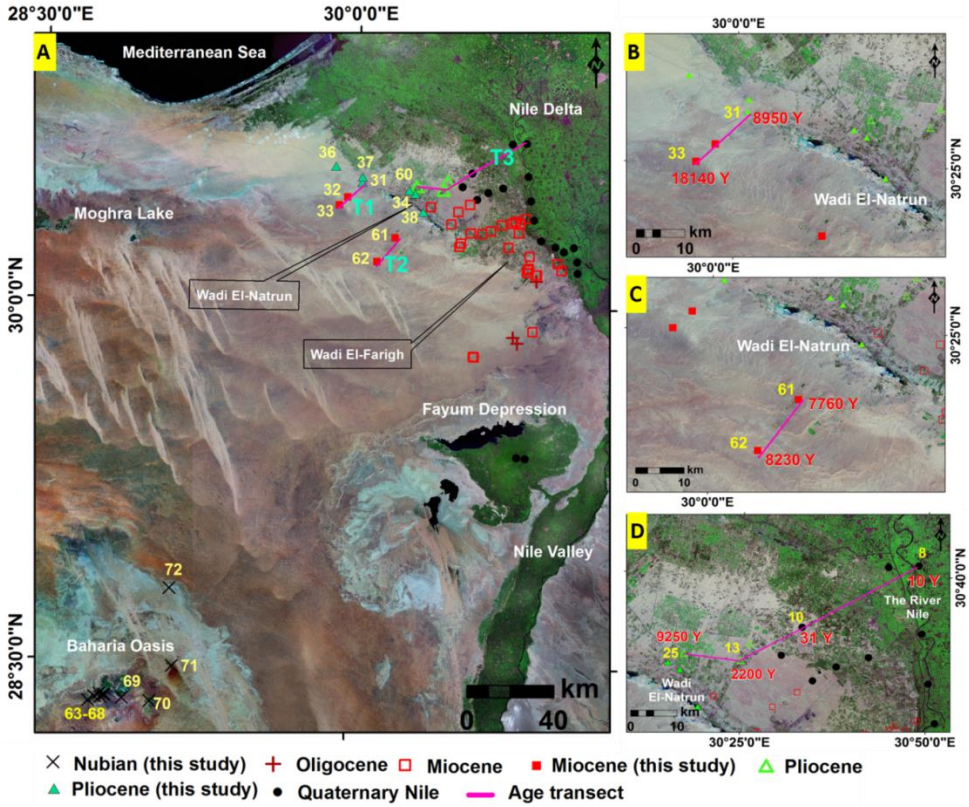

Figure 18. (A) Distribution of groundwater samples from this study (solid symbols) and from previous studies (Thompson, 2007; El-Gamal, 2005) (open symbols) from the Quaternary Nile, Pliocene, Miocene, Oligocene, and NAS aquifers in the north Western Desert of Egypt that were analyzed for their stable isotopic compositions (O and H) and locations of transects along which groundwater samples were collected in this study (T1 and T2) and in previous studies (T3; Aeschbach-Hertig et al., 2007) for ^{14}C dating. Enlargement of areas encompassing T1, T2, and T3 on Figure 18A are shown in Figure 18B, 18C, and 18D, respectively; these figures show transect location (*purple line*), sample numbers (*yellow*) and C-14 ages (*red*). Area covered by Figure 18A is outlined by open red box 18A on Figure 1, and locations of wells are shown as solid yellow circles on Figure 1.

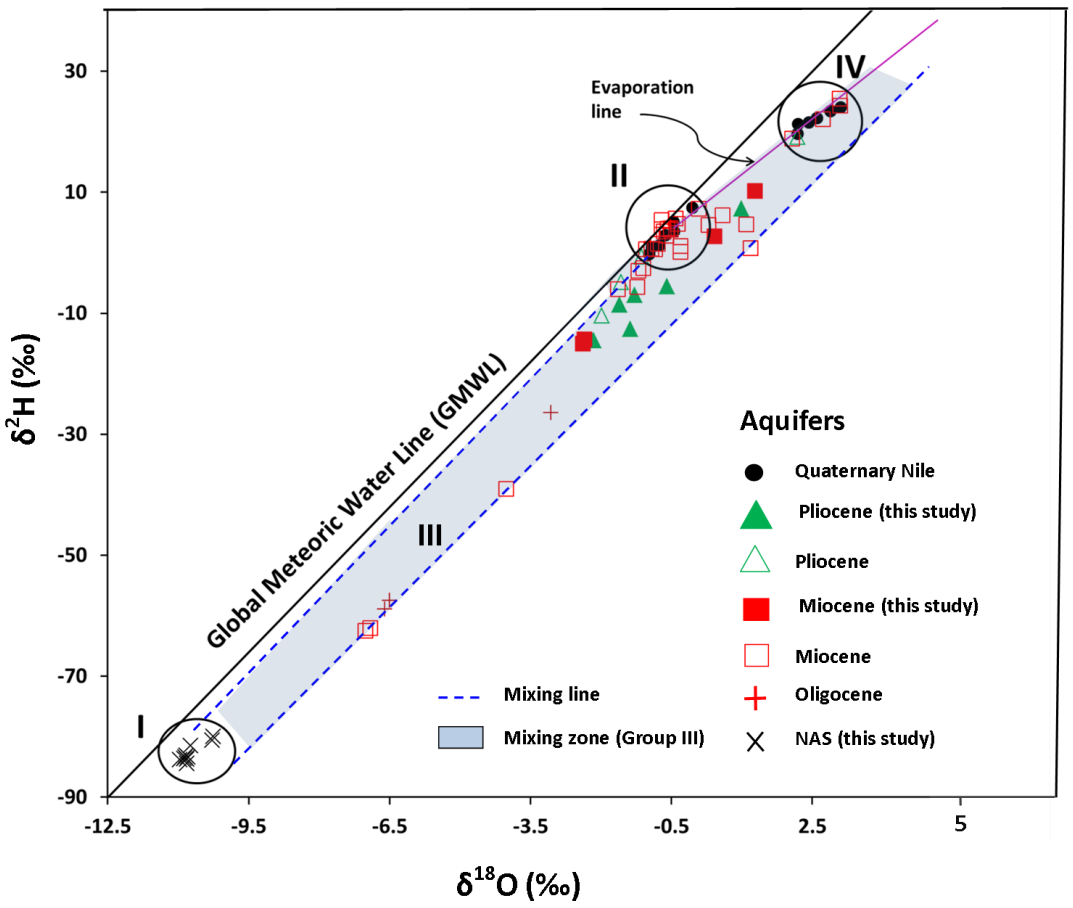

Figure 19. δD versus $\delta^{18}O$ plot for groundwater samples from fossil Nubian aquifer NAS (Group I), OMPQ aquifer (Groups II and III), and Quaternary Nile Aquifer Group (IV). Also shown are the fields for the NAS groundwater (Sultan et al., 1997; Patterson et al., 2005), pre–High Dam groundwater (El-Bakri et al., 1992; Sultan et al., 2000), and post–High Dam groundwater (Dahab et al., 1999; El-Gamal, 2005), the GMWL as a solid line ($\delta D = \delta^{18}O+10$; Craig, 1961) and the evaporation line for the Nile water as a purple line (Sultan et al., 2000).

CHAPTER 6

DISCUSSION

This section first describes the popular models (sapping versus surface runoff) for the origin of the THV and shows that the requirements for the former model, not the latter, are available in the study area. Then it provides a conceptual model to explain how the sapping model can account for the observed topographic, geomorphologic, and hydrogeologic settings over the NSAS study area. Finally, it discusses the implications of the findings from the present study on the timing of wet periods in the Sahara.

6. 1 Groundwater versus Surface Runoff Models

The role of groundwater sapping in shaping THV in resistant bedrock has been recently challenged, and alternative models (e.g. megaflooding, waterfall erosion, and landslides) for the development of THV were proposed (Lamb et al., 2006, 2008; Lamb and Dietrich, 2009; Craddock et al., 2012; Lamb et al., 2014; Marra et al., 2014; Irwin et al., 2014). The major arguments they cite against the seepage erosion origin are the bedrock strength and the large size of THV, which necessitate gigantic water discharge systems and/or substantial weathering along the seepage face to disintegrate the bedrock into loose debris and a transporting agent/or agents to remove the debris out of the valley (Howard and Kochel, 1988; Lamb et al., 2006; Luo and Howard, 2008). It also requires a long timescale of groundwater seepage (Howard and Selby, 1994; Lamb et al., 2006).

The findings indicate that the requirements (i.e., prolonged groundwater seepage and a mechanism to disintegrate and transport debris) for the groundwater sapping model, but not the surface runoff model, are present in the study area and that the aforementioned arguments against the groundwater sapping model are not applicable to the Saharan THV.

Field investigations revealed that strong-over-weak stratigraphy and extensive salt and chemical weathering is common in areas where THV were reported (refer to sections 4.3 and 4. 4), as did the investigations by other researchers in the Qattara depression (Aref et al., 2002), Fayum depression (Keatings et al., 2007), Dakhla depression (El Kammar and El Kammar, 1996; Brookes, 2010), Kharga depression (Salman et al., 2010), and in Egypt's cultural heritage sites such as the Giza Pyramids and Sphinx (Goudie, 2013) and the Pharaonic sandstone monuments in Luxor (Smith, 1986; Wust and Schluchter, 2000). It is most likely that the strong-over-weak stratigraphy along with the extensive salt and chemical weathering facilitate the removal of the basal unit along the Saharan escarpments and the development of THV.

The distribution of denudational landforms (refer to section 4.4; Figs. 12–16) and the ages (50 to 620 ka of tufa deposits along scarp faces and within scarp-foot depressions; Sultan et al., 1997; Smith et al., 2004a; Adelsberger and Smith, 2010; Jimenez, 2014) suggest that the denudational activities were widely distributed and that they operated for long periods. If the groundwater-related denudational activities operated for a long time span, and if the tufa were deposited from the groundwater, the ages of the groundwater should be consistent with these suggestions; ^{81}Kr and ^{36}Cl

groundwater ages (200 ka to 1.2 Ma: Sturchio et al., 2004; Patterson et al., 2005) for 25 samples from the Western Desert show that this is indeed the case. The present study suggests that fluvial denudational activities operated for long periods during previous wet periods that extend as far back as 1 million years ago. Recent ^{36}Cl ages (up to 1.3 Ma) for groundwater samples from the NSAS (Mohamed et al., 2015) indicate that the denudational activities could have operated for even a longer time period. The long-term fluvial denudation hypothesis is supported by the findings from quantitative models that suggest that groundwater processes may have an important role in the development of THV through a combination of seepage weathering and episodic removal of weathered debris by runoff and spring discharge (Pelletier and Baker, 2011). These models were developed to investigate the role of groundwater seepage in weathering bedrock, transporting unconsolidated debris and incision of U-shaped valleys in water-limited environments such as the Sahara.

Extensive sand dune fields are observed in the downwind direction of the Qattara depression (refer to section 4.4; Fig. 9A); the composition (quartz sand with minor carbonate, argillaceous material, and gypsum fragments) of the dune material is consistent with derivation from the Moghra and Marmarica Formations cropping along the northern escarpment of the Qattara depression (Aref et al., 2002). During the previous wet period, this material could have originated as debris excavated from the Qattara escarpment by groundwater discharge, been transported down the gradient towards the depression floor, and been disintegrated by salt weathering and later deflated by winds in subsequent dry periods. This suggestion is supported by the

findings of Brookes (2001, 2003), who emphasized the role of aeolian erosion in shaping landscapes, carving depressions, and transporting unconsolidated debris during the interleaving dry periods in the Egyptian portion of the Sahara.

The oscillation of the wet and dry climatic conditions (Szabo et al., 1995; Smith et al., 2004a) over the Sahara probably accelerated the scarp retreat. During wet periods, rock falls and slumped blocks accumulate along the ramparts and are partially eroded by the endorheic fluvial drainage systems originating from the scarp faces, and are disintegrated by salt weathering processes. With the advent of aridity, the groundwater table is lowered, wind activity intensifies, and additional weathered and disintegrated debris is removed by deflation from the valley floor. Groundwater sapping activities increase the rate at which escarpments retreat (Higgins and Osterkamp, 1990). Throughout the past 620,000 years, the retreat of the eastern escarpment bounding the Southern High Plains in Texas was rapid (190 m/1000 yr) (Simpkins and Baumgardner, 1982), compared to the northern escarpment (31 to 42 m/1000 yr) (Gustavson et al., 1980). The former, but not the later area, is highly affected by sapping processes. If we were to adopt the Southern High Plains rates in the Western Desert, we estimate that the escarpment could have retreated by some 200 km in a million years, a distance that exceeds the width of each of the Farafra (maximum width: 75 km) and Qattara depressions (maximum width: 176 km). The scarp retreat in the Dakhla and Kharga could not be estimated given that they are open depressions, unlike the closed Farafra and Qatara depressions. Hence, the continuous processes of groundwater discharge, scarp retreat, and sediment transport in wet and

dry periods could be responsible for the formation of THV and the excavation of the natural depressions (e.g., in Egypt: Qattara, Siwa, Bahariya, Farafra, Dakhla, Kharga; in Libya: Jaghbub) in the Libyan Plateau.

The features cited in support of surface runoff models (i.e., maegaflooding or waterfall erosion) for the origin of the THV in the Box Canyon and Malad Gorge, Idaho and in Hawaii (Lamb et al., 2008, and 2014; Craddock et al., 2012) are absent in the study area. These models require the presence of large watersheds that collect extensive amount of precipitation and channel them into a limited number of valleys. It has been shown that the distribution of the NSAS THV is extensive along the length of the scarp, there is a general lack of well-developed watersheds draining into the THV, and if present they are limited in size (typically <15 km^2; refer to section 4.1). The surface runoff models are more suited for areas of high to medium slope gradients, where infiltration is minimal and runoff is high. That is not the case in the study area, where the flat-topped limestone plateau occupies large sectors of the NSAS landscape. Moreover, there are no records of megafloods during the Quaternary period in the study area.

6. 2 Conceptual Model

A conceptual model was developed based on findings from the present study to assess the origin of THV and natural depressions in the study area, and possibly across the Sahara (Fig. 20). Seven stages are suggested: (1) precipitation over the Nubian sandstone outcrops in the south (i.e., the NAS) during the previous wet climatic periods resulted in a considerable rise of the paleopiezometric surface as much as 25 m higher than the present level (Pachur and Hoelzmann, 2000); (2) further to the north, the thick sedimentary sequences (up to 2 km thick), the confined nature of the aquifer, and the presence of deep-seated sub-vertical faults led to upward migration of groundwater from the NAS to discharge at or near the surface; (3) groundwater flow converged along free faces that were formed by structural discontinuities (e.g., faults or shear zones) or to a lesser extent by hydraulic piping failures; (4) small THV originate along free faces and enlarge and deepen with continued discharge of groundwater giving rise to extensive denudation along the structurally controlled escarpments; (6) the massive carbonate caprock is undermined and slumps, and the escarpment recedes by continued groundwater seepage along the contact between the limestone caprock and the underlying weak units and by seepage weathering of rock debris; and (7) rock debris is removed from the ramparts of the escarpment either by fluvial processes in wet periods or by wind erosion during arid periods. These stages give rise to the following landforms: THV, natural depressions, circular remnant hills, sabkhas, spring mounds, and endorheic paleolakes.

The advocated model introduces a regional comprehensive solution for the enigmatic occurrence of natural depressions and associated landforms over the Libyan Plateau in the Sahara and overcomes the shortcomings of the previous models. Models that call on the formation of natural depression by wind deflation encounter difficulties explaining the removal of massive limestone caprocks across the Sahara by wind alone. The proposed model can. As indicated earlier, in wet periods, rising groundwater compromises the integrity of the caprock; it removes underlying soft beds, causing rockfalls and block slumping of caprocks and its disintegration by salt weathering and dissolution. Caprock debris is further weathered and removed by wind deflation in interleaving arid periods. Models that call on the formation of natural depressions by fluvial stream erosion cannot explain the absence of well-developed exorheic streams over the Libyan Plateau. The groundwater sapping model does not require the existence of surface exorheic streams where the driving force is ascending groundwater. It also explains the role of endorheic streams, seepage weathering, and/or wind erosion in the removal of rock falls on the scarp ramparts, deposition of tufa along scarp faces, development of landforms within scarp-foot depressions, and deposition of high calcium carbonate sediments within paleolakes.

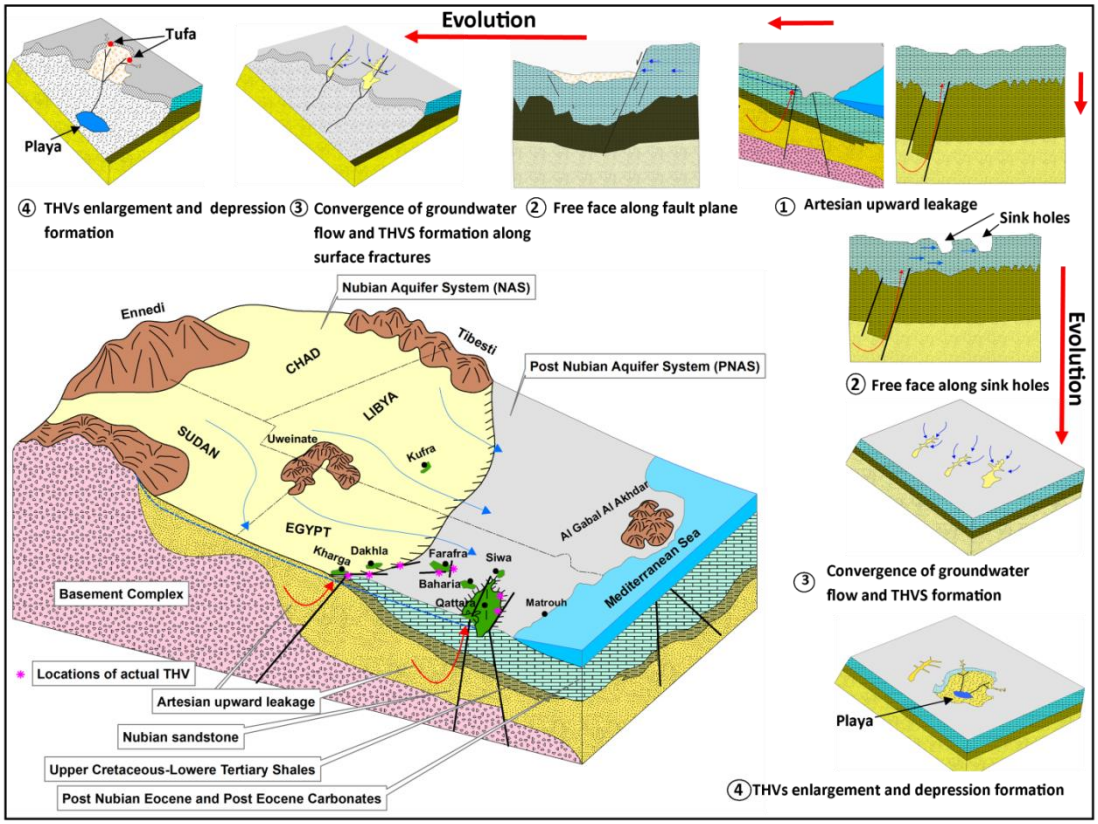

Figure 20. Block diagram of the NSAS (modified from Salem and Pallas, 2004) and landscape evolution schematic diagrams showing summary of the proposed hydrological and geomorphological processes leading to the formation of THV and natural depressions in the Sahara.

6. 3 Timing of Wet Periods

During the Quaternary wet periods the NSAS was recharged mainly by precipitation over recharge areas in the south and to a lesser extent by local precipitation (Thorweihe, 1990; Patterson et al., 2005). The timing and nature of the wet periods are subjects of debate; they were attributed to the intensification of paleomonsoons during interglacial periods (e.g., Prell and Kutzbach, 1987; Yan and Petit-Maire, 1994) or paleowesterlies during glacial periods (e.g., Sultan et al., 1997; Sturchio et al., 2004; Abouelmagd et al., 2012). Regardless of whether the wet periods were glacial or interglacial in origin, a considerable rise of the paleopiezometric surfaces was reported and the Nubian groundwater discharge intensified in depressions within Eastern Sahara (Pachur and Hoelzmann, 2000; Abotalib et al., 2016).

During previous wet climatic periods in the Sahara, one would expect a considerable lag between the time groundwater was recharged and the time it discharged in the depressions; the progressive increase in ages of groundwater (up to 1 million years) along flow direction supports this suggestion (Fig. 21; Patterson et al., 2005). This is related to the large distance (>100 km) separating recharge areas (close to Sudanese borders) from discharge areas (in depressions) and the modest groundwater velocities (0.5 to 3.5 m/yr.; Patterson et al., 2005) in the deep portion of the NAS. Findings from the present study indicate that artesian Nubian groundwater accessed deep-seated faults and contributed to the formation of paleolakes and springs in scarp-foot depressions. Because these water bodies provided ideal locations for human occupations, investigating their nature and evolution through time can provide a better

understanding for the links between climatic variability, landscape evolution and old human occupation in North Africa. Many of the basinal sediments including lacustrine, travertine and tufa deposits—that were left behind this water activity—have been studied to reconstruct the paleoclimate variability in the Sahara during the Quaternary. Examples of these studies include: Crombie et al., (1997); Kieniewicz and Smith (2007); Kieniewicz and Smith (2009) and Brookes (2010). These paleoclimatic interpretations did not take into consideration the delayed surface discharge of pluvially recharged groundwater. The overwhelming contribution of the groundwater to the formation of the basinal deposits and the time lag between recharge and discharge can confound attempts to reconstruct paleoclimatic conditions (e.g. paleotemperatures)—where for example, the isotopically inferred lake water would display characteristics that are representative of the recharge environment rather than those of the surrounding environment—and hence cast doubts on the validity of using these basinal deposits for paleoclimatic interpretations.

The expected time lag could also mislead the proper placement of wet periods in the Sahara during alternate glacial and interglacial marine stages. In order to examine this hypothesis, I compiled and reviewed all available dates from lacustrine, travertine and tufa deposits in the Eastern Sahara (Fig. 22). Inspection of figure 22 could reveal the timing and nature (i.e. interglacial versus glacial periods) of prevailing wet periods in the Sahara. Alternatively, it could demonstrate the uncertainties associated with the use of basinal sediments for paleoclimatic interpretations and timing of wet periods. The figure shows that wet periods extended through both glacial and interglacial

periods, an observation that is supported by recent electron spin resonance (ESR) dating of more than 90 samples of basinal sediments from the Dakhla depression (Kleindienst et al., 2016). Their findings indicate a long-term habitability in the Dakhla depression during at least twelve marine isotope stages. Similar findings could be extracted from the Frequency distribution of published age dates for the basinal sediments from the Eastern Sahara (Fig. 23). The figure shows two peaks of dates spanning the interglacial marine stage 1 (i.e. the Holocene) and the glacial marine stage 6. These results complicate the previous interpretations that advocate that either the glacial or the interglacial periods were solely responsible for the greening of the Sahara. They also point to the need to investigate the favorable conditions under which the basinal deposits could be used to identify the age of the wet periods and taking into consideration the potential role of the groundwater discharge in their formation.

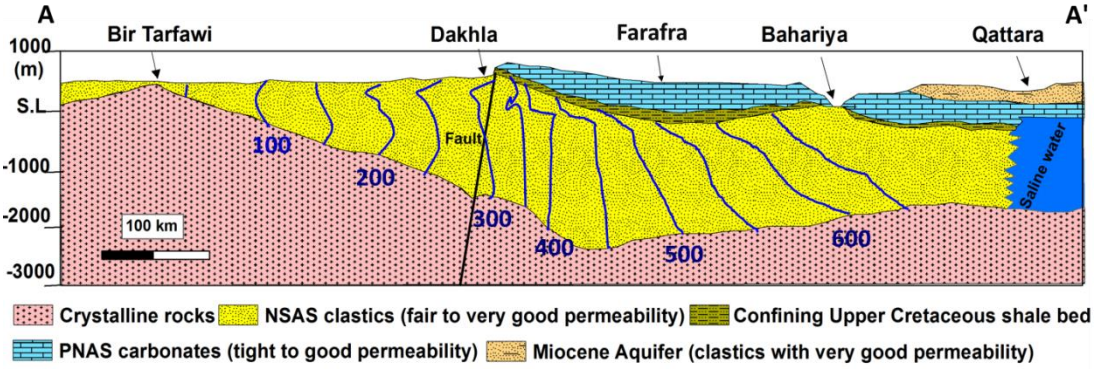

Figure 21. Hydrologic cross section of the Dakhla basin in the NSAS showing predicted groundwater ages (in thousands years) based on average groundwater velocity in the NAS (modified from Thorweihe, 1990 and Patterson et al., 2005). The cross section was constructed along transects A-A′ shown as a solid line on Figure 2.

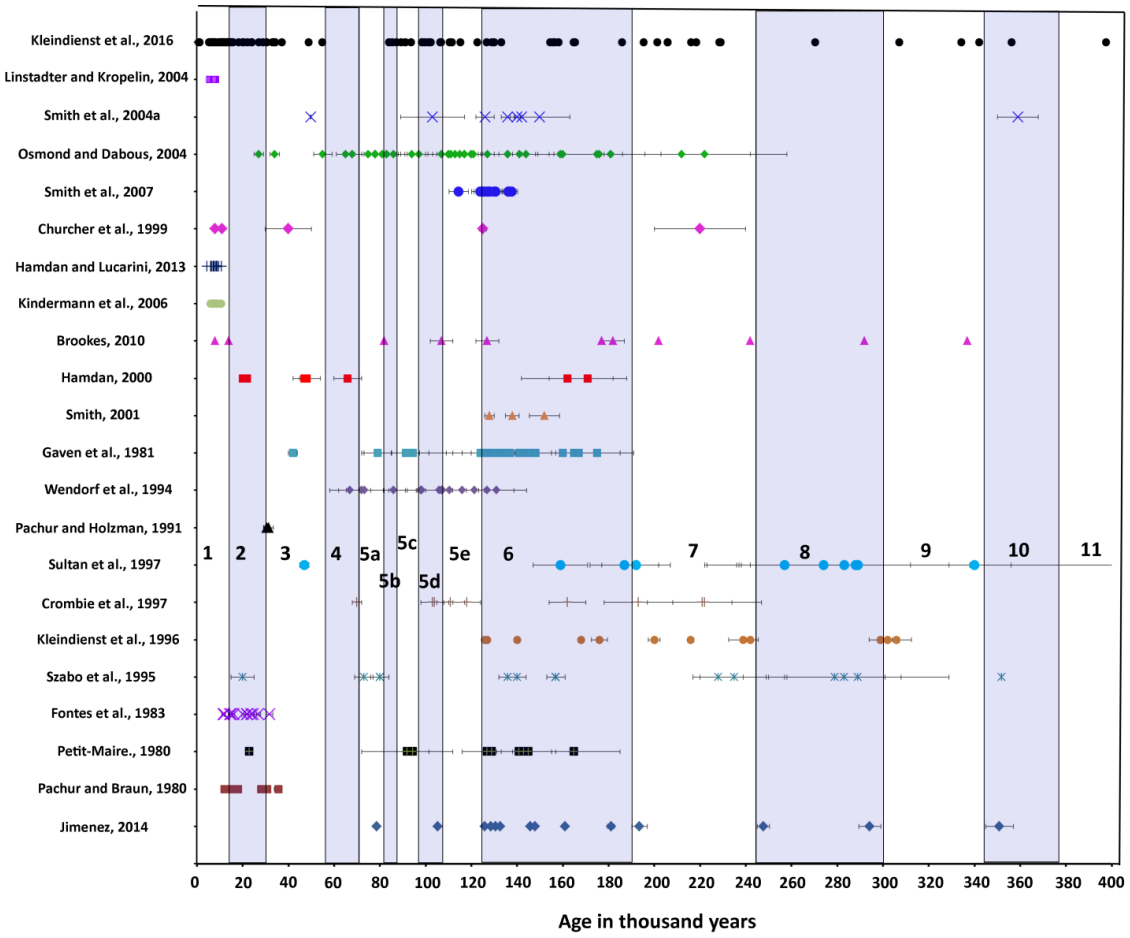

Figure 22. Summary of the reported ages of lacustrine, travertine and tufa deposits in the Eastern Sahara showing the widespread distribution of ages between glacial periods (i.e. shaded areas) and interglacial periods (non-shaded areas).

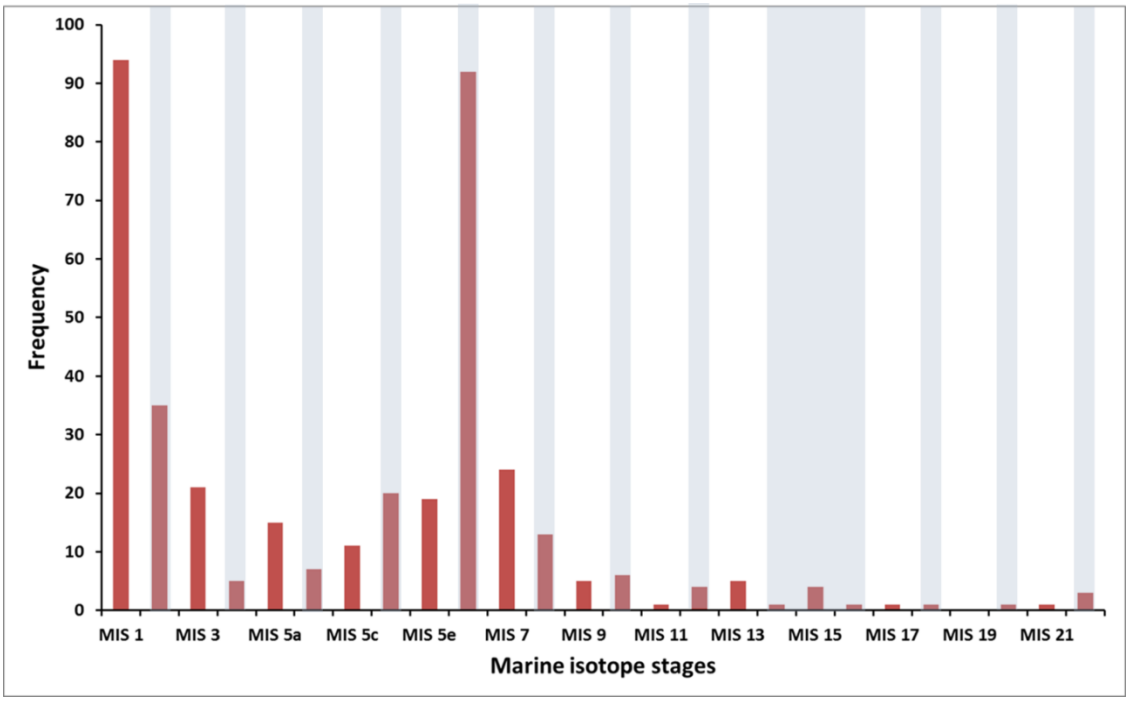

Figure 23. Frequency distribution of reported ages for basinal deposits collected from the Eastern Sahara showing two main clusters of ages, one corresponding to the interglacial MIS 1, and the other to the glacial MIS 6 with numerous smaller age groups throughout glacial (glacial) and interglacial periods (non-shaded).

CHAPTER 7

TIMING OF WET CLIMATIC PERIODS; OPTICALLY STIMULATED LUMINESCENCE (OSL) AGES OF THE SINAI QUATERNARY DEPOSITS

7.1 Geologic Setting

The Quaternary deposits in the Feiran watershed, Sinai (Fig. 24) were collected and dated using optically stimulated luminescence techniques to investigate the timing of the Saharan wet periods. These deposits are ideal for such investigations because of the relatively small size of the Feiran watershed (i.e. 1868 km^2), steep slope gradient in such mountainous terrains and the occurrence of these deposits unconformably overlying the Proterozoic crystalline rocks of the Arabian-Nubian Shield (Fig. 24). In such a setting, groundwater discharge from the underlying crystalline rock units is impeded by the massive nature of the basement rocks. These deposits have been studied around the Feiran (lat. 28.706N; long. 33.665E; elevation: 715 to 772 m a.m.s.l) and Tarfa (lat. 28.692N; long. 33.933E; elevation: 1160 to 1244 m a.m.s.l) Oases by Awad (1953), Issar and Eckstein (1969) and Gaber et al., (2009) and were interpreted as paleolake (i.e. lacustrine) deposits. However, the detailed field surveys that I conducted in 2014 and 2015 revealed that these successions are largely composed of alluvial deposits and loess (i.e. yellow silts, fine- to coarse-grained sands intercalated with pebbly size granitic fragments) with dispersed patches of colluvial (i.e. poorly sorted angular shaped cobbles and boulders) and paludal deposits (i.e. marls with abundant plant roots and mud snails) (Figs. 25, 26 and 27). These deposits attain thicknesses of up to 35 m in Feiran Oasis and 50 m in Tarfa Oasis. In general, the Tarfa Oasis deposits

(upstream) are coarser than the Feiran deposits (downstream). Alluvial loess in the two successions is believed to be introduced in the Feiran watershed by wind activity during arid climatic periods and later washed out from the mountainous slopes and redeposited during subsequent wetter periods as overbank fines around the main channel of Wadi El-Sheikh and Wadi Feiran (Konard et al., 2004).

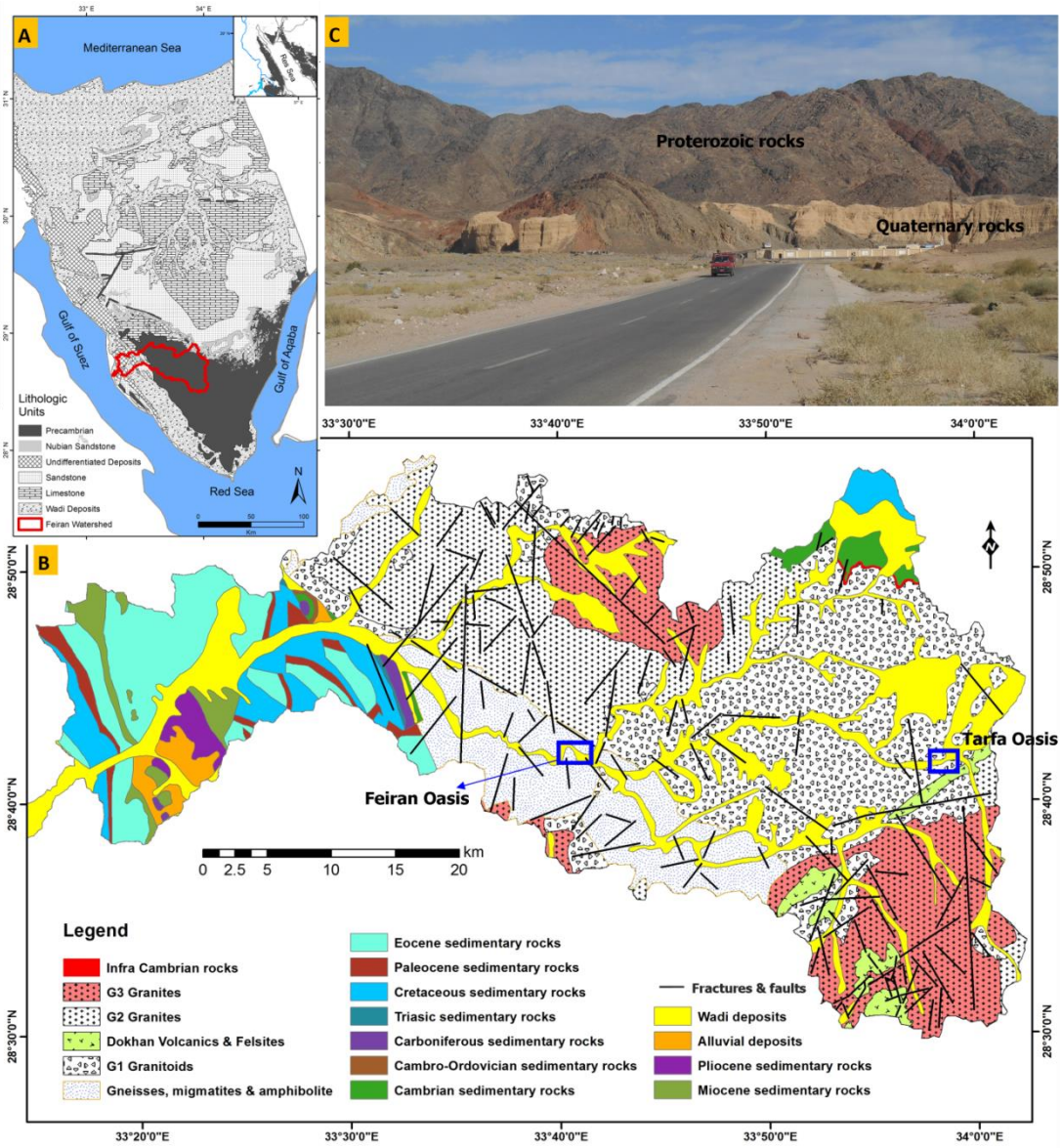

Figure 24. (A) Location map of the Feiran watershed; (B) Geological map of the Feiran watershed showing the distribution of geological units and structures and the location of the Feiran and Tarfa Oases where Quaternary deposits were sampled for OSL dating; (C) Field Panorama along Wadi Feiran within the Feiran Oasis showing Quaternary deposits overlying the Proterozoic crystalline rocks.

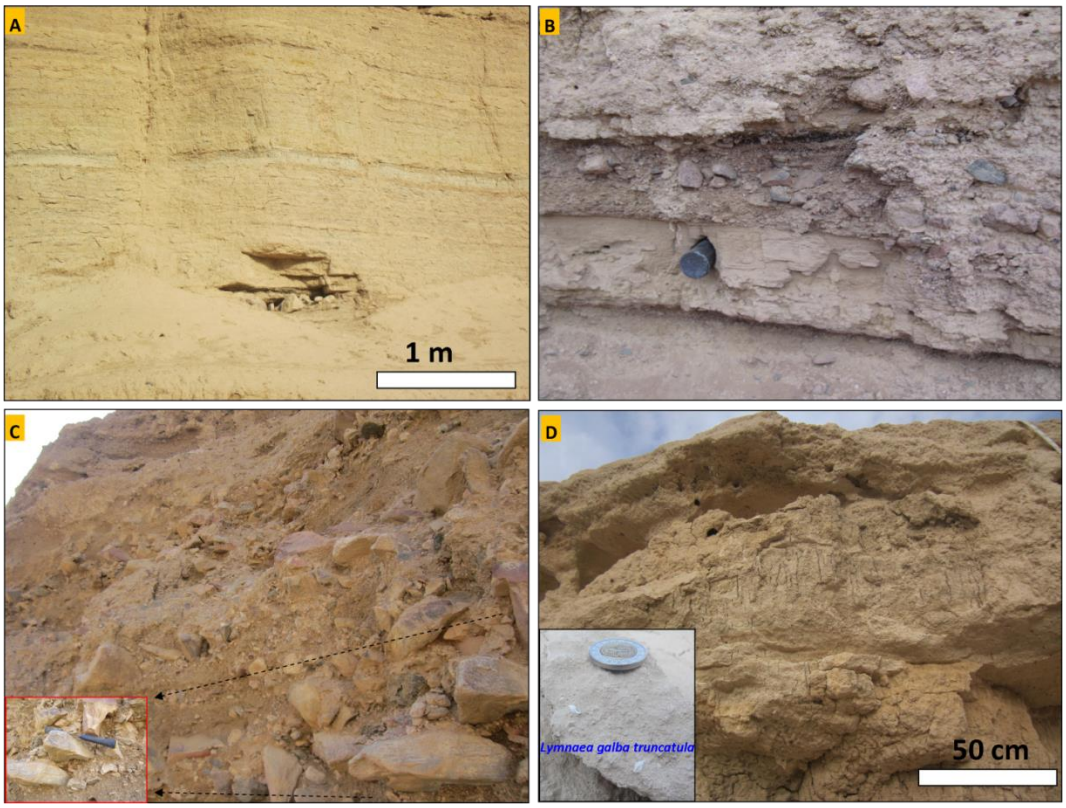

Figure 25. Field shots of various lithofacies within the Quaternary deposits of the Feiran watershed. (A) fine-grained sands and alluvium loess; (B) intercalations of alluvium sands and poorly sorted cobbles and pebbles of granitic fragments; (C) angular-shaped boulders and cobbles; and (D) marly succession with abundant plant roots and mud snails (Lymnaea galba Truncatula). Also shown, a metal tube used for OSL sampling (B), and inset showing enlargements for angular shaped boulders and cobbles (C) and mud snails (D).

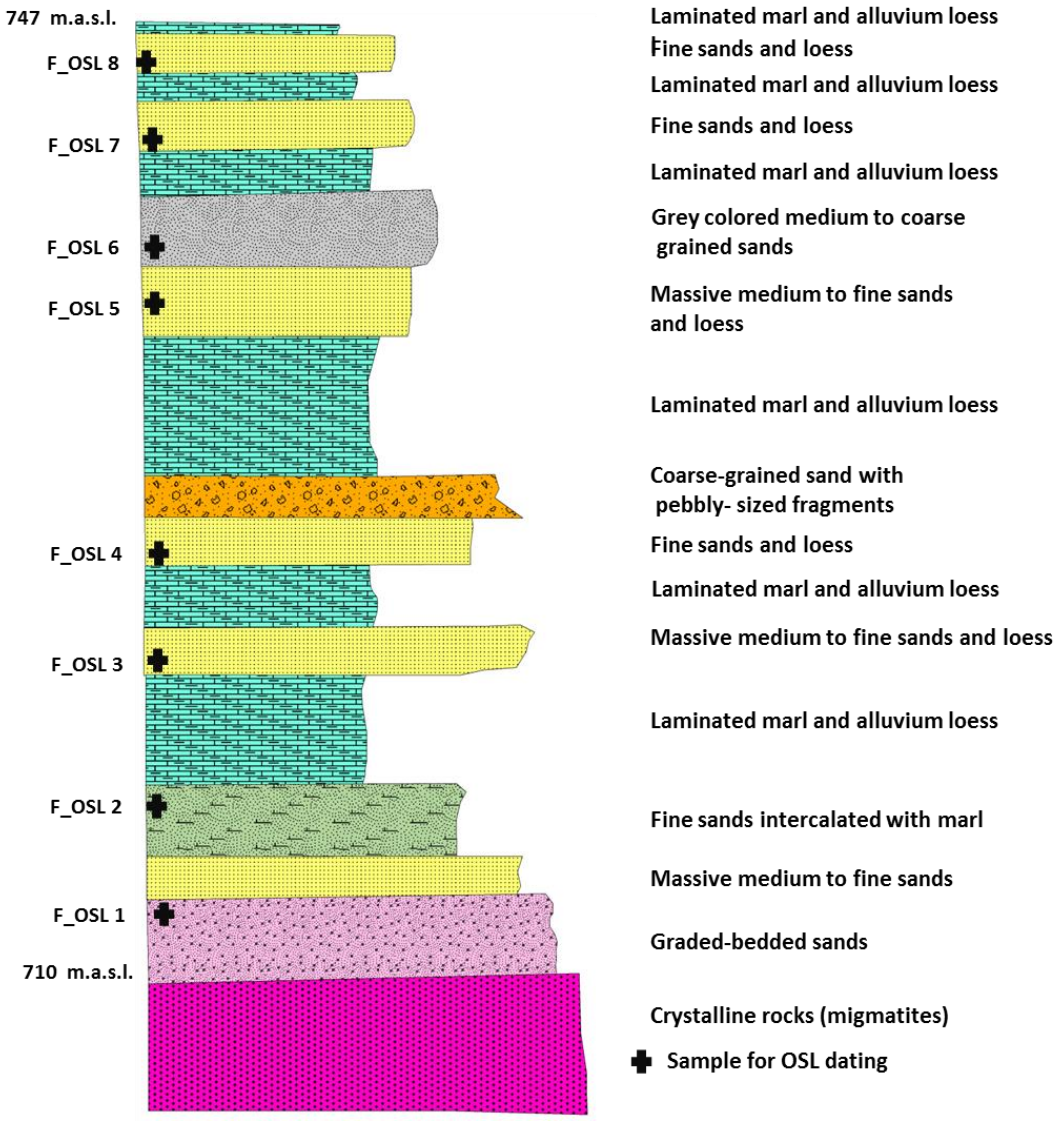

Figure 26. Lithostratigraphic section for the Quaternary deposits in Feiran Oasis showing the lithological units exposed along the sides of the main stream within the Feiran watershed.

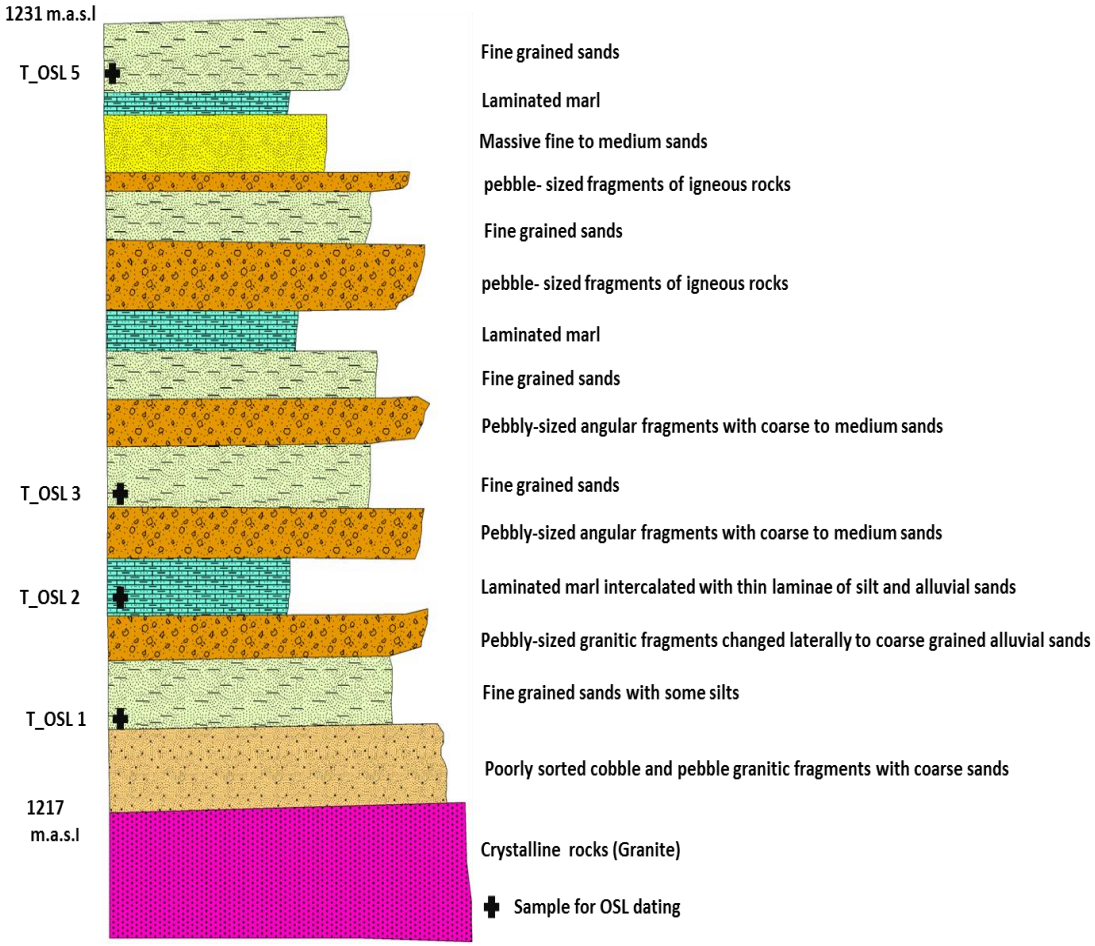

Figure 27. Lithostratigraphic section of the Quaternary deposits in the Tarfa Oasis showing the lithological units exposed along the sides of the main stream within the Feiran watershed.

7.2 OSL Sample Collection and Analysis

The OSL method is based on the fact that when lake sediments are buried, the effects of the incoming solar radiation are removed. Hence, the cosmic rays and the naturally-occurring radioactive isotopes within the buried sediments produce damage to individual quartz or feldspar grains. The longer the burial time, the greater the signal indicative of damage within individual mineral grains. This signal is the key to luminescence dating techniques. By estimating the rate of received ionizing radiation (i.e. the dose rate) from the surrounding environment, and knowing the total accumulated dose (i.e. the equivalent dose), the burial age (yr) of the sample can be estimated as follows:

$$OSl\ age\ \ (yr) = \frac{Equivelent\ dose\ (Gray)}{Dose\ rate\ (\frac{mGray}{yr})} \qquad (9)$$

Two stratigraphic successions were sampled in Feiran (7 samples) and Tarfa (4 samples) Oases for OSL dating (Figs. 26 and 27) throughout two field trips in 2014 and 2015. Samples were collected in 20 cm long, aluminum pipes (diameter: 8 cm) that were pounded into the outcrop under minimum exposure to sunlight during the sampling process (Fig. 25B). A second set of samples were collected in plastic bags for the dose-rate of the surrounding environment. These samples were collected from a circular area (diameter: 30 cm) surrounding the sample tube. The geographic location, sample elevation and burial depth were determined for each sample. Analysis of samples was conducted in the Geoluminescence Dating Research Laboratory at Baylor

University. The single aliquot regeneration (SAR) protocols were applied on the 63-100, 100-150, 150-250 and 425-500 μm quartz fractions for 23 to 67 separate aliquots (Tables 4 and 5). The purity of quartz separates was evaluated by petrographic inspection and point counting of a representative aliquot. Calculation of equivalent dose by the single aliquot protocols was analyzed under blue-light excitation (470 ± 20 nm) for 23 to 50 aliquots (Tables 4 and 5). Analyzed samples exhibit over-dispersion values with precession beyond instrumental errors especially those with values ≤ 20 % (at 1 sigma errors). Elevated values of >20% indicate a mixture of grain ages and/or insufficient solar resetting with deposition. A determination of the dose rate from the surrounding environment is needed to render an optical age. The U and Th content of the sediments, assuming secular equilibrium in the decay series and ^{40}K, were determined by inductively coupled plasma-mass spectrometry (ICP-MS/OES) analyzed by Activation Laboratory LTD, Ontario, Canada. The beta and gamma doses were adjusted according to grain diameter to compensate for mass attenuation (Fain et al., 1999) and the amount of cosmic ray dose (i.e. between 0.02 and 0.208 mGy/yr) was included in the estimated dose rate taking into account the current depth of burial (Prescott and Hutton, 1994). A uniformly, low moisture content for the burial of period of 3 +/- 1%, reflecting the hyper-arid conditions today was also applied. OSL ages were calculated using the Central Age Model or Finite Mixture Model of Galbraith et al. (1999) with over-dispersion values of <20% and >20%, respectively.

Table 4. Optically stimulated luminescence (OSL) age on quartz grains from Quaternary deposits in Feiran Oasis, Sinai, Egypt

Sample	Aliquots	Grain size (microns)	Equivalent dose (Gray) [a]	Cosmic dose (mGray/yr) [d]	Dose rate (mGray/yr) [e]	OSL age (yr) [e]
F_OSL 2	31/45	425-500	75.10 ± 5.09	0.03 ± 0.003	2.95 ± 0.15	25,440 ± 2230
F_OSL 3	47/48	100-63	77.69 ± 3.11	0.03 ± 0.003	2.91 ± 0.15	26,680 ± 1780
F_OSL 4	30/30	150-100	68.87 ± 2.93	0.04 ± 0.004	3.24 ± 0.19	21,250 ± 1490
F_OSL 5	50/67	100-63	55.63 ± 2.38	0.02 ± 0.002	3.26 ± 0.19	17,085 ± 1100
F_OSL 6	28/30	150-250	39.47 ± 1.86	0.155 ± 0.02	2.98 ± 0.15	13,435 ± 950
F_OSL 7	38/47	150-250	37.69 ± 1.51	0.176 ± 0.02	2.68 ± 0.14	14,060 ± 910
F_OSL 8	36/48	150-250	31.33 ± 1.37	0.208 ± 0.02	2.87 ± 0.15	10,910 ± 780

Table 5. Optically stimulated luminescence (OSL) age on quartz grains from Quaternary deposits in Tarfa Oasis, Sinai, Egypt

Sample	Aliquots	Grain size (microns)	Equivalent dose (Gray) [a]	Cosmic dose (mGray/yr) [d]	Dose rate (mGray/yr) [e]	OSL age (yr) [e]
T_OSL1	30/35	150-250	107.38 ± 4.59	0.02 ± 0.002	3.86 ± 0.19	27,780 ± 1770
T_OSL 2	27/32	150-250	98.36 ± 4.69	0.08 ± 0.01	4.46 ± 0.22	22,055 ± 1490
T_OSL 3	25/36	150-250	95.67 ± 4.64	0.10 ± 0.01	4.77 ± 0.24	20,045 ± 1365
T_OSL 5	23/23	100-150	62.26 ± 2.81	0.208 ± 0.02	6.06 ± 0.15	10,260 ± 670

7.3 Interpretation and Implications of the OSL Dates

Quartz extracts from the two stratigraphic successions in Feiran and Tarfa Oases yielded OSL dates typically between ca. 27 and 10 ka (Tables 4 and 5) and place the deposition of these relatively thick successions (up to 50 m) to the last glacial period (MIS 2). The fact that the two successions yielded very similar ages—yet with different dose rate environments—gives added confidence in the ages. Predominant texture of alluvial deposits in the two studied successions indicates direct deposition from stream flow under wet climatic conditions and assures sufficient exposure to sunlight before deposition. The deposition of these successions during the MIS 2 does not only demonstrate prevalent wet periods during glacial periods over the Sahara—where glacial wet periods were generally underestimated—but also sheds doubts on the validity of the reconstructions of paleoclimate variability in the Sahara during the Quaternary using conventional dating and isotopic methods where no clear records for wet periods during MIS 2 were reported. This observation calls on re-examination of the earlier paleoclimatic reconstructions of the Sahara throughout the Quaternary period for a better understanding of the nature and timing of the wet periods, the period when the Saharan aquifers were recharged.

CHAPTER 8

REGIONAL AND PLANETARY IMPLICATIONS

8.1 Implications for Landscape Evolution in the Sahara-Arabian Desert Belt

The procedures that were used to identify and map the THV over the NSAS were also applied to investigate the presence of these valleys over other fossil aquifer systems in the Sahara and in the Arabian Peninsula. Specifically, the procedure includes the morphological characteristics (10 characteristics: refer to sections 1.3 and 3.1) and statistical analysis (refer to section 3.1 and 3.2). The new analysis revealed extensive occurrence of THV along, or proximal to, escarpments that we interpret as paleodischarge locations in the Saharan and Arabian Deserts. We cite two examples, the NWSAS and the Upper-Mega Aquifer System in the Plateau of Najd in Saudi Arabia (Figs. 1, 28A and 28B).

Findings from the present study and those reported in the literature indicate that the THV in these two aquifer systems share remarkable geologic, hydrologic, and geomorphologic characteristics with those reported from the NSAS. These include: (1) local structural control along pre-existing structural discontinuities (e.g., propagation directions that are northeast-east parallel to the main trend of the Gebel El-Gharbi escarpment; Figs. 28A and 28C); (2) minimal upstream contribution areas for many of the THV; they are typically <50 km^2 in size (e.g., NWSAS, Gebel El-Gharbi area; Fig. 28C) and in some cases, they are absent as is the case with the Tuwaiq Mountains (Fig.

28B) in the Najd Plateau where the plateau dips steeply towards the east and away from the main valley propagation direction to the west (Fig. 28D); (3) the THV, escarpment, and deep-seated faults are within the confined sectors of the aquifer where clastic-dominated formations are overlain by thick carbonate and shale deposits (Thorweihe and Heinl, 2002; Edmunds et al., 2003; Stöckl, 2010); (4) THV are located within areas that witnessed wet climatic periods, elevated groundwater levels in the Pleistocene (Causse et al., 1989; McLaren et al., 2009), and natural discharge of fossil groundwater '>1 million years' (Guendouz and Michelot, 2006; Sultan et al., 2015) along deep-seated sub-vertical faults (Swezey, 1996; Engelhardt et al., 2013) and within areas of high structural control (Cornet, 1964; Guendouz and Michelot, 2006; Beaumont, 1977).

The widespread distribution of the THV in the NSAS (1450 km; refer to section. 3.2), the NWSAS (~1500 km along the Hamada De Tinhert, Plateau De Tademait, and Gebel El-Gharbi escarpments; Fig. 28A), and the Najd Plateau (~500 km along the Tuwaiq mountain escarpment; Fig. 28B) suggest extensive and widespread groundwater discharge and intense groundwater denudational activities in the Saharan and Arabian deserts during the previous wet climatic periods.

Similar groundwater-related denudational processes and/or landforms (i.e., sapping features, headward channel growth, scarp retreat, and incised canyons) were reported from many areas outside of the Saharan and Arabian deserts. Examples include, the extensive landscape modifications in the northern China deserts by progressive headward channel growth of THV (Yang et al., 2015), the retreat of the

Southern High Plains (Wood, 2002), the undermining of the massive Navajo Sandstone in the Colorado Plateau and the integration of the Colorado River system (Laity and Malin, 1985; Crossey et al., 2015), and the incision of canyons within plateaus (Hackness Hill Plateau, England: Nash, 1996; Murge Plateau, Italy: Mastronuzzi and Sanso, 2002; Altiplano Plateau, northern Chile: Hoke et al., 2004).

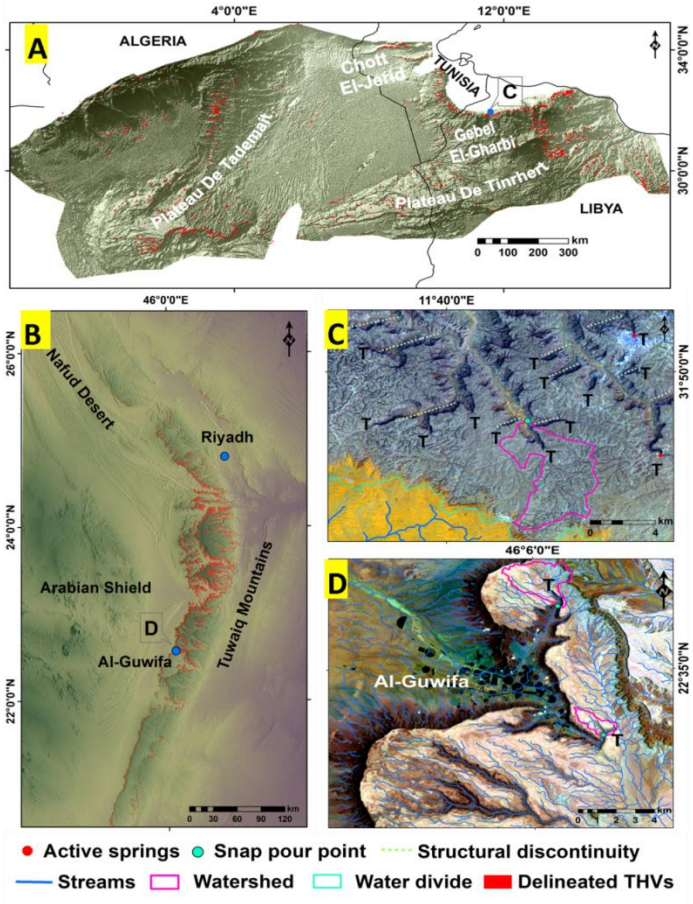

Figure 28. Distribution of THV in Saharan and Arabian fossil aquifers. (A) Hillshade image showing delineated THV in the NWSAS. (B) Hillshade image showing delineated THV in the Najd Plateau in Saudi Arabia. (C) False-color Landsat 8 data for area C in Figure 28A showing that the THV are structurally controlled by northeast-east trending structural discontinuities and that they receive minimal upstream contributions. (D) False-color Landsat 8 data for area D in Figure 28B showing endorheic streams and THV draining to the west in a direction opposite from the dip of the plateau (east) and the drainage direction of the exorheic streams on the plateau (*bright areas*). Letter T marks the onset of the THV.

8.2 Implications for paleoclimate variability in North Africa and Arabia

Across the African and Arabian Sahara, features similar to those reported in this work from the Western Desert were reported. These include abundance of groundwater sapping-related features in these regions and long lasting groundwater residence periods. These were described in detail for two major aquifers; the NWSAS in Algeria, Tunisia, and Libya and the Upper Mega Aquifer in the Arabian Sahara (refer to section 7.1). As in the case of the NAS, there has been ambiguity regarding the timing and nature of the wet periods during which these aquifers were recharged. For example for the NWSAS, the wet periods were reported for glacial and interglacial periods based on analysis of freshwater deposits (Gaven et al., 1981; Causse et al., 1989; Prendergast et al., 2016) and ^{36}Cl ages of fossil groundwater (Guendouz and Michelot, 2006; Petersen et al., 2014). In the Arabian Peninsula, similar contradictions pertaining to the timing and nature of these wet period were reported from the analysis of flood deposits (McLaren et al., 2009), paleolake deposits (Rosenberg et al., 2013), and fossil groundwater ages (Sultan et al., 2015). It is likely that the considerable lag time (hundreds of thousands of years) between the time recharge occurred and discharge of groundwater and deposition of basinal sediments led to errounous interpretation of the dated basinal sediments. The obtained ages do not provide information on the timing of the wet periods, instead they reflect the timing of discharge of the groundwater and the deposition of the basinal sediments.

8.3 Implications for the Origin of Outflow Channels in Valles Marineris, Mars

Extensive and widespread THV (outflow channels) were recorded on Mars along the length of, and cutting across, the walls of Valles Marineris (Marra et al., 2015; Fig. 29). Understanding the Martian surface and subsurface processes and their effects on the evolution of the landscape is hindered by the inaccessibility of Mars. Fortunately, the hyper-arid Sahara provides one of the best terrestrial analogs for examining the origin and evolution of many of the Martian landscape features (Higgins, 1982; Grant et al., 2004; Paillou et al., 2014), especially THV. The individual THV on Mars are larger in size than their Arabian and Saharan counterparts, yet they are geomorphologically similar (Higgins, 1982; Luo, 2000) (Fig. 29, inset). The Martian THV display characteristics similar to those reported from their Saharan and Arabian counterparts: (1) they are widespread and densely distributed along the length of Martian escarpments for over 1400 km (Marra et al., 2015), (2) they are located largely in areas where extensive faulting was reported (Treiman, 2008; Montgomery et al., 2009), a suggestion that is supported by the distribution of many of the THV along linear structural discontinuities, (3) the lack of well-developed stream networks draining towards the individual THV (Fig. 29), and (4) they are frequently associated with large-scale spring deposits (Rossi et al., 2008), but lack flood deposits commonly associated with terrestrial THV that are generated by megafloods (McEwen et al., 2012). The occurrence of these features along the crest of a 3 km high topographic bulge on the Tharsis Plateau (Montgomery and Gillespie, 2005), their dense

distribution, their presence along both sides of Valles Marineris on surfaces dipping away from the canyon, and the absence of large drainage areas needed to form the Martian THV (Fig.29) makes it unlikely that they originated from well-developed exorheic systems.

Given the above mentioned observations from the Tharsis Plateau, the similarities between the Saharan and Martian THV, findings pertaining to the significant role of groundwater processes in shaping the Saharan landscape, and the reported gigantic groundwater discharge on Mars (Montgomery and Gillespie, 2005; Montgomery et al., 2009; Mara et al., 2015), the present study suggests that future studies should investigate: (1) the potential role of structural control, pressurized groundwater discharge, and sapping processes in the evolution of the Martian landscape, and (2) the origin of the recently reported recurring slope lineae (McEwen et al., 2014) on the slopes of Valles Marineris.

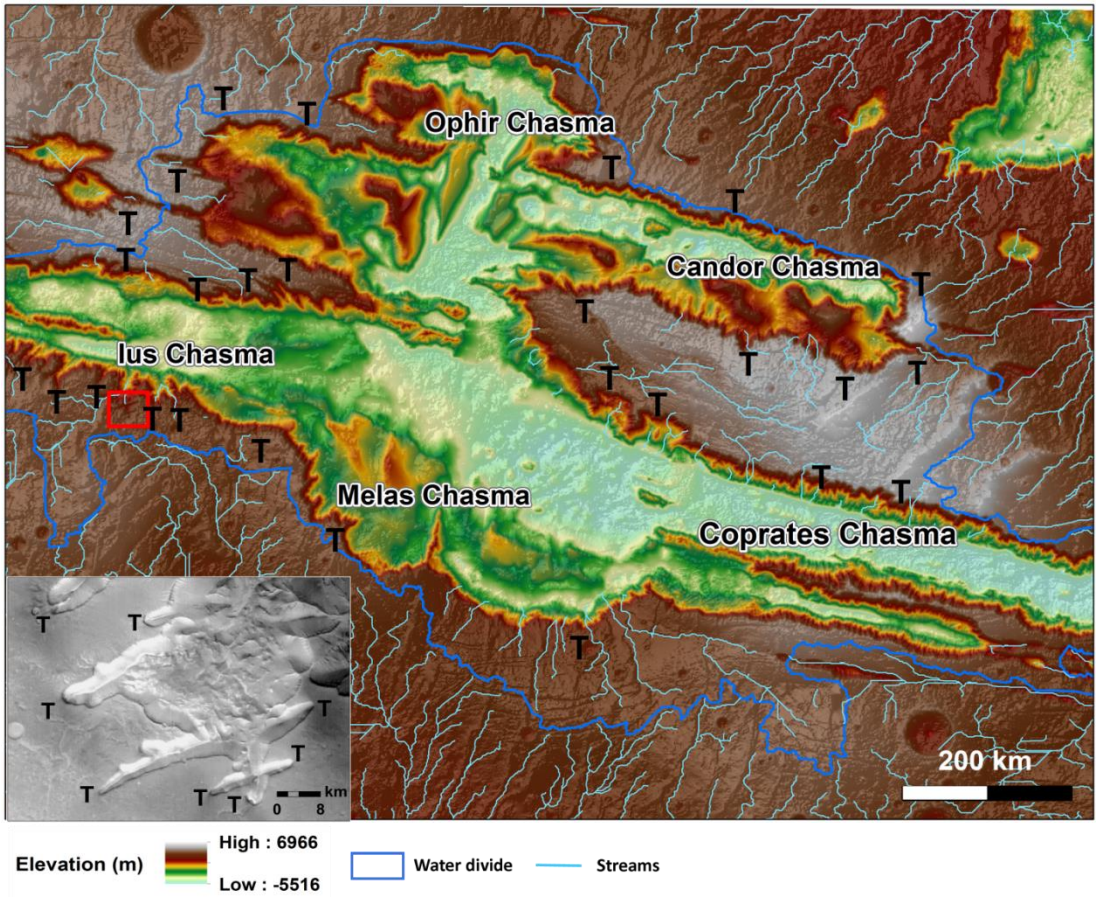

Figure 29. Color-coded digital elevation model extracted from the MOLA mosaic for the eastern region of Valles Marineris and surroundings showing extensive and dense distribution of THV (marked with letter "T") and absence of well-developed streams draining toward the THV. Inset: enlargement for area covered by the red box generated from the HRSC mosaic (ESA/DLR/FU Berlin) showing the distribution of THV along the walls of Ius Chasma.

CHAPTER 9

SUMMARY

(1) Observations and findings from the present study are consistent with elevated groundwater levels in the NSAS during previous wet climatic periods and favor a groundwater origin rather than a surface runoff origin for the THV in the Sahara. These statements are supported by the following:

a. LR model outputs over the NSAS reveal an extensive distribution of THV along the escarpments bounding depressions in the Libyan Plateau;
b. spatial analysis of modeled THV reveals strong spatial correlation with the distribution of tufa and Group I playa deposits;
c. analysis of Radarsat-1 and DEM-based stream networks indicates that the well-developed exorheic drainage systems are absent over the Libyan Plateau and that the onset of endorheic streams are associated with the delineated THV;
d. mass balance calculations indicate that the small size of the upslope contributing areas for the individual THV is inconsistent with a fluvial origin for these features given the extensive erosion that is required to remove the large volumes of material that once resided within the area occupied by the THV;
e. areas with abundant THV demonstrate high regional and local structural control;

f. the escarpments that are strongly dissected by THV are characterized by strong-over-weak stratigraphy and show evidence of salt weathering, dissolution features, and groundwater activity;

g. playa deposits proximal to THV within scarp-foot depressions have high carbonate content and are enriched in $\delta^{13}C$ values;

h. isotopic composition ($\delta^{18}O$) of tufa deposits (147 samples) are consistent with deposition from depleted Nubian waters (range $\delta^{18}O$: −12.8 to −8.0‰);

i. stable isotopic analyses of groundwater samples (71 samples) from the OMPQ aquifer indicate that the fossil Nubian groundwater ascended along deep-seated fault systems and discharged into the overlying shallower OMPQ aquifer.

(2) Quartz extracts from two stratigraphic successions in Sinai yielded OSL dates between 27 and 11 ka and placed one of the Saharan wet period into the last glacial period.

(3) The above-mentioned findings over the NSAS in the Western Desert and the OSL dates obtained for stratigraphic successions in Sinai cast doubts on the previous attempts to date the wet climatic periods in the Sahara using basinal deposits.

(4) Considerable lag time (hundreds of thousands of years) occurred between the recharge time and the time of groundwater discharge and deposition of basinal

sediments in the NAS; this led to erroneous interpretation of the ages obtained from dating basinal sediments. These ages represent the timing of groundwater discharge and deposition of basinal sediments, but they were mistakenly used to date the wet periods.

(5) As in the case of the NAS, there has been ambiguity regarding the timing and nature of the wet periods during which similar aquifers in Saharan Africa and Arabia were recharged. The widespread distribution of features similar to those reported over the NSAS across the African and Arabian Sahara including groundwater sapping-related features and long groundwater residence periods indicate that the ages of basinal sediments in these areas that represent the timing of groundwater discharge and deposition of basinal sediments were also mistakenly used to date the wet periods

(6) Outflow channels in Vallis Marineris on Mars show morphological, geological and structural characteristics, similar to those reported from the Saharan THV-abundant regions, suggesting that groundwater processes could have played a major role in shaping the Martian landscape.

(7) Understanding the role of groundwater processes in landscape evolution over areas occupied by the NSAS has implications for understanding the development of landscape in Saharan Africa, Arabian Sahara, similar settings worldwide, and the evolution of the Martian landscape.

REFERENCES

Abdeldayem, A. L., 1996. Palaeomagnetism of some Miocene rocks, Qattara depression, Western Desert, Egypt. J. African Earth Sci. 22, 525-533.

Abotalib, A.Z., Mohamed, R.S.A., 2013. Surface evidences supporting a probable new concept for the river systems evolution in Egypt: a remote sensing overview. Environ. Earth Sci. 69, 1621–1635.

Abotalib, A.Z., Sultan, M., Elkadiri, R. 2016. Groundwater processes in Saharan Africa: Implications for landscape evolution in arid environments. Earth Sci. Rev. 156. 108–136.

Abouelmagd, A., Sultan, M., Milewski, A., Kehew, A.E., Sturchio, N.C., Soliman, F., Krishnamurthy, R.V., Cutrim, E., 2012. Toward a better understanding of palaeoclimatic regimes that recharged the fossil aquifers in North Africa: Inferences from stable isotope and remote sensing data. Palaeogeogr. Palaeoclimatol. Palaeoecol. 329, 137–149.

Abouelmagd, A., Sultan, M., Sturchio, N.C., Soliman, F., Rashed, M., Ahmed, M., Kehew, A.E., Milewski, A., Chouinard, K., 2014. Paleoclimate record in the Nubian Sandstone Aquifer, Sinai Peninsula, Egypt. Quat. Res. 81, 158–167.

Adelsberger, K.A., Smith, J.R., 2010. Paleolandscape and paleoenvironmental interpretation of spring-deposited sediments in Dakhleh Oasis, Western Desert of Egypt. Catena 83, 7–22.

Aeschbach-Hertig, W., El-Gamal, H., Dahab, K., Friedrich, R., Kipfer, R., Hajdase, I., 2007. Identifying and dating the origin of groundwater resources in reclamation areas of Egypt. Advances in Isotope Hydrology and its Role in Sustainable Water Resources Management, Vienna 395–403.

Akgün, A., Türk, N., 2011. Mapping erosion susceptibility by a multivariate statistical method: a case study from the Ayvalık region, NW Turkey. Comput. Geosci. 37, 1515–1524.

Albritton, C.C., Brooks, J.E., Issawi, B., Swedan, A., 1990. Origin of the Qattara depression, Egypt. Geol. Soc. Am. Bull. 102, 952–960.

Alfarhan, M.S., Arafat, S.M., Abdelsalam, M.G., 2006. Interplay of Cretaceous-Quaternary faulting and folding in the south desert of Egypt: Insights from remote sensing analysis, in: Geological Society of America Abstracts with Programs. 3–15.

Aref, M.A.M., El-Khoriby, E., Hamdan, M.A., 2002. The role of salt weathering in the origin of the Qattara Depression, Western Desert, Egypt. Geomorphology 45, 181–195.

Awad, A., 1953. Signification Morphologique des Deposits Lacustres de la Montagne du Sinai Central. Bull. .Royal Soc. Geogr. Egypt XXV. 23–28.

Bakhbakhi, M., 2006. Nubian sandstone aquifer system. Resour. A Guideb. Soc. Sustain. Manag. Water-Policy Makers, Paris United Nations Educ. Sci. Cult. Organ. (IHP-VI Ser. Groundw. 10. 75–81.

Ball, J., 1927. Problems of the Libyan desert. Geogr. J. 21–38.

Beaumont, P., 1977. Water and development in Saudi Arabia. Geogr. J. 42–60.

Bellin, N., Vanacker, V., Kubik, P.W., 2014. Denudation rates and tectonic geomorphology of the Spanish Betic Cordillera. Earth Planet. Sci. Lett. 390, 19–30.

Brookes, I.A., 2001. Aeolian erosional lineations in the Libyan desert, Dakhla region, Egypt. Geomorphology 39, 189–209

Brookes, I.A., 2003. Geomorphic indicators of Holocene winds in Egypt's Western Desert. Geomorphology 56, 155–166.

Brookes, I.A., 2010. Spatially variable sedimentary responses to orbitally driven pluvial climate during Marine Oxygen Isotope Stage 5.1, Dakhla Oasis region, Egypt. Quat. Res. 74, 252–264.

Brown, G.F., Coleman, R.G., 1972. The tectonic framework of the Arabian Peninsula. 24th International Geological Congress Report, Montreal, 3, p.300-305.

Caussé, C., Coque, R., Fontes, J.C., Gasse, F., Gibert, E., Ouezdou, H. Ben, Zouari, K., 1989. Two high levels of continental waters in the southern Tunisian chotts at about 90 and 150 ka. Geology 17, 922–925.

Cartwright, J.A., and Dewhurst, D.N., 1998, Layer-bound compaction faults in fine-grained sediments. Geol. Soc. Am. Bull. 110, 1242–1257.

Cherkinsky, A., Culp, R.A., Dvoracek, D.K., Noakes, J.E., 2010. Status of the AMS facility at the University of Georgia. Nucl. Instruments Methods Phys. Res. Sect. B Beam Interact. with Mater. Atoms 268, 867–870.

Churcher, C.S., Kleindienst, M.R., Schwarcz, H.P., 1999. Faunal remains from a Middle Pleistocene lacustrine marl in Dakhleh Oasis, Egypt: palaeoenvironmental reconstructions. Palaeogeogr. Palaeoclimatol. Palaeoecol. 154, 301–312.

Conoscenti, C., Angileri, S., Cappadonia, C., Rotigliano, E., Agnesi, V., Märker, M., 2014. Gully erosion susceptibility assessment by means of GIS-based logistic regression: A case of Sicily (Italy). Geomorphology 204, 399–411.

Coplen, T.B., 1996. New guidelines for reporting stable hydrogen, carbon, and oxygen isotope–ratio data. Geochim. Cosmochim. Acta 60, 3359–3360.

Cornet, A., 1964. Introduction à l'hydrogéologie Saharienne. Rev. Geéographie Phys. Géologie Dyn. 61, 5–72.

Craddock, R.A., Howard, A.D., Irwin, R.P., Tooth, S., Williams, R.M.E., Chu, P., 2012. Drainage network development in the Keanakāko ʻi tephra, Kīlauea Volcano, Hawai ʻi: Implications for fluvial erosion and valley network formation on early Mars. J. Geophys. Res. Planets 117.

Craig, H., 1961. Isotopic variations in meteoric waters. Science 133, 1702-1703

Crombie, M.K., Arvidson, R.E., Sturchio, N.C., El Alfy, Z., Zeid, K.A., 1997. Age and isotopic constraints on Pleistocene pluvial episodes in the Western Desert,

Egypt. Palaeogeogr. Palaeoclimatol. Palaeoecol. 130, 337–355. doi:10.1016/S0031-0182(96)00134-4

Crossey, L.C., Karlstrom, K.E., Dorsey, R., Pearce, J., Wan, E., Beard, L.S., Asmerom, Y., Polyak, V., Crow, R.S., Cohen, A. and Bright, J., 2015. Importance of groundwater in propagating downward integration of the 6–5 Ma Colorado River system: Geochemistry of springs, travertines, and lacustrine carbonates of the Grand Canyon region over the past 12 Ma. Geosphere 11,660-682.

Dahab, K., Sadek, M., El-Fakharany, M. K., 1999. Replenishment and mineralization processes of lower Miocene aquifer at Wadi El-Farigh area and its vicinities, using environmental isotopes and hydrochemistry. Sci. J, Fac. Sci. Menufia Univ. 13, 15–25.

Devauchelle, O., Petroff, A.P., Seybold, H.F., Rothman, D.H., 2012. Ramification of stream networks. Proc. Natl. Acad. Sci. USA 109, 20832–20836. doi:10.1073/pnas.1215218109

Dunne, T., 1980. Formation and controls of channel networks. Prog. Phys. Geogr. 4, 211–239. doi:10.1177/030913338000400204

Edmunds, W.M., Guendouz, A.H., Mamou, A., Moulla, A., Shand, P., Zouari, K., 2003. Groundwater evolution in the Continental Intercalaire aquifer of southern Algeria and Tunisia: trace element and isotopic indicators. Appl. Geochemistry 18, 805–822.

El-Bakri, A., Tantawi, A., Blavoux, B., Dray, M., 1992. Sources of water recharge identified by isotopes in El Minya Governate (Nile valley, Middle Egypt), in: Proceeding of International Symposium on Isotope Techniques in Water Resources Development 1991, IAEA, Vienna, 643-645.

El-Gamal, H., 2005. Environmental tracers in groundwater as tools to study hydrological questions in arid regions. PhD Thesis, University of Heidelberg, 146 pp.

El-Hinnawi, M., Philibbos, E., Riad, S., El-Khawaga, M.M., 2005. Geological Map of the south Western Desert, Egypt.

El-Hinnawi,M., Philibbos, E., Riad, S., El-Khawaga, M.M., 2006. Geological Map of the north Western Desert, Egypt.

El Kammar, A.M., El Kammar Jr, M.M., 1996. Potentiality of chemical weathering under arid conditions of black shales from Egypt. J. Arid Environ. 33, 179–199.

Engelhardt, I., Rausch, R., Keim, B., Al-Saud, M., Schüth, C., 2013. Surface and subsurface conceptual model of an arid environment with respect to mid- and late Holocene climate changes. Environ. Earth Sci. 69, 537–555.

Fain, J., Soumana, S., Montret, M., Miallier, D., Pilleyre, T., Sanzelle, S., 1999. Luminescence and ESR dating-beta-dose attenuation for various grain shapes calculated by a Monte-Carlo method. Quat. Sci. Rev. 18. 231–234.

Fernandez, S., Marquínez, J., Menéndez-Duarte, R., 2008. A sapping erosion susceptibility model for the southern Cantabrian Range, North Spain. Geomorphology 95, 145–157.

Fontes, J. -C ., Coque, R., Dever, L., Filly, A. and Mamou, A.,1983. Paleohydrologie isotopique de I'oued El Akarite (Sud Tunisie) au Pleistocene Superieur et a I'Holocene. Palaeogeogr. Palaeoclimatol. Palaeoecol. 43. 41–62.

Friedman, I., O'Neil, J.R., 1977. Compilation of stable isotope fractionation factors of geochemical interest. In: Fleischer. (Eds.), Data of Geochemistry, 6th Ed. Geological Survey Professional Paper 440-KK.

Gaber, A., Ghoneim, E., Khalaf, F. and El-Baz, F., 2009. Delineation of paleolakes in the Sinai Peninsula, Egypt, using remote sensing and GIS. J. arid env. 73. 127–134.

Galbraith, R.F., Roberts, R.G., Laslett, G.M., Yoshida, H., Olley, J.M., 1999. Optical dating of single and multiple grains of quartz from Jinmium rock shelter, northern Australia, part 1, experimental design and statistical models. Archaeometry 41. 339–364.

Gaven, C., Hillaire-Marcel, C. and Petit-Maire, N., 1981. A Pleistocene lacustrine episode in southeastern Libya. Nature 290.131–133.

Ghoneim, E., El-Baz, F., 2007. The application of radar topographic data to mapping of a mega-paleodrainage in the Eastern Sahara. J. Arid Environ. 69, 658–675.

Giaconia, F., Booth-Rea, G., Martínez-Martínez, J.M., Azañón, J.M., Pérez-Peña, J.V, 2012. Geomorphic analysis of the Sierra Cabrera, an active pop-up in the constrictional domain of conjugate strike-slip faults: The Palomares and Polopos fault zones (eastern Betics, SE Spain). Tectonophysics 580, 27–42.

Gindy, A.R., Albritton, C.C., Brooks, J.E., Issawi, B., Swedan, A., 1991. Origin of the Qattara Depression, Egypt: Discussion and reply. Geol. Soc. Am. Bull. 103, 1374–1376.

Goudie, A.S., 2013. Arid and semi-arid geomorphology. Cambridge University Press.

Grant, J.A., Maxwell, T.A., Johnston, A.K., Kilani, A., Williams, K.K., 2004. Documenting drainage evolution in Bir Kiseiba, southern Egypt: Constraints from ground penetrating radar and implications for Mars. J. Geophys. Res. Planets 109.

Guendouz, A., Michelot, J.-L., 2006. Chlorine-36 dating of deep groundwater from northern Sahara. J. Hydrol. 328, 572–580.

Guiraud, R., Bosworth, W., 1997. Senonian basin inversion and rejuvenation of rifting in Africa and Arabia: synthesis and implications to plate-scale tectonics. Tectonophysics 282, 39–82.

Gustavson, T. C., Finley, R.J., and McGillii, K.A., 1980. Regional dissolution of Permian salt in the Anadarko, Dalhart and Palo Duro basins of the Texas Panhandle. University of Texas at Austin Bureau of Economic Geology, Austin.

Hamdan, M.A., 2000. Quaternary travertines of Wadis Abu Had-dib area Eastern Desert, Egypt: paleoenvironment through field, sedimentology, age, and isotopic study. Sediment. Egypt 8. 49–62.

Hamdan, M.A., Lucarini, G., 2013. Holocene paleoenvironmental, paleoclimatic and geoarchaeological significance of the Sheikh El-Obeiyid area (Farafra Oasis, Egypt). Quat. Int. 302, 154–168.

Hassan, F.A., Barich, B., Mahmoud, M., Hemdan, M.A., 2001. Holocene playa deposits of Farafra Oasis, Egypt, and their palaeoclimatic and geoarchaeological significance. Geoarchaeology 16, 29–46.

Haynes, C.V., 2001. Geochronology and climate change of the Pleistocene–Holocene transition in the Darb el Arba'in Desert, Eastern Sahara. Geoarchaeology 16, 119–141.

Haynes, C.V., Haas, H., 1980. Radiocarbon evidence for Holocene recharge of ground water, Western Desert, Egypt. Radiocarbon 22, 705–716.

Hermina, M., 1990. The surroundings of Kharga, Dakhla and Farafra oases, in: The Geology of Egypt. Balkema, Rotterdam, pp. 259–292.

Higgins, C.G., 1982. Drainage systems developed by sapping on Earth and Mars. Geology 10, 147–152.

Higgins, C.G., Osterkamp, W.R., 1990. Seepage-induced cliff recession and regional denudation. Geol. Soc. Am. Spec. Pap. 252, 291–318.

Hobbs, S.W., Paull, D.J., Clarke, J.D.A., 2014. A comparison of semiarid and subhumid terrestrial gullies with gullies on Mars: Implications for Martian gully erosion. Geomorphology 204, 344–365.

Hoke, G.D., Isacks, B.L., Jordan, T.E., Jennifer, S.Y., 2004. Groundwater-sapping origin for the giant quebradas of northern Chile. Geology 32, 605–608.

Howard, A.D., Kochel, R.C., 1988. Introduction to cuesta landforms and sapping processes on the Colorado Plateau. NASA Spec. Publ. 491, 6.

Howard, A.D., Selby, M.J., 1994. Rock slopes, in: In: Abrahams, A.D., Parsons, A.J. (Eds.), Geomorphology of Desert Environments. Springer, pp. 123–172.

International Groundwater Resources Assessment Centre (IGRAC).2012. Transboundary Aquifers of the World. Available at http://www.un-igrac.org/dynamics/modules/SFIL0100/view.php?fil_Id=213

Irwin, R.P., Tooth, S., Craddock, R.A., Howard, A.D., de Latour, A.B., 2014. Origin and development of theater-headed valleys in the Atacama Desert, northern Chile: Morphological analogs to Martian valley networks. Icarus 243, 296–310.

Issar, A., Eckstein, Y., 1969. The lacustrine beds of Wadi Feiran, Sinai: their origin and significance. Israel J. Ear. Sci. 18. 21–27.

Issawi, B., 1982. Geology of the southwestern desert of Egypt. Ann. Geol. Surv. Egypt 11, 57–66.

Jerris, T., 2014. Development of structural basins and domes on the Sinn El-Kaddab Plateau, Egypt: Insights from in situ data and application of moderate

resolution orbital imagery of the Seiyal fault. Master's thesis, Missouri University of Science and Technology.

Jimenez, G., 2014. Travertine from Egypt's Western Desert: a Terrestrial Record of North African paleohydrology and paleoclimate during the late Pleistocene. Master's thesis, University of New Mexico.

Khan, S.D., Mohamed S.F., Abdelazeem, M., 2014. Remote sensing and geophysical investigations of Moghra Lake in the Qattara Depression, Western Desert, Egypt. Geomorphology 207, 10–22.

Keatings, K., Tassie, G.J., Flower, R.J., Hassan, F.A., Hamdan, M.A.R., Hughes, M., Arrowsmith, C., 2007. An examination of groundwater within the Hawara Pyramid, Egypt. Geoarchaeology 22, 533–554.

Kieniewicz, J.M., Smith, J.R., 2007. Hydrologic and climatic implications of stable isotope and minor element analyses of authigenic calcite silts and gastropod shells from a mid-Pleistocene pluvial lake, Western Desert, Egypt. Quat. Res. 68, 431–444.

Kieniewicz, J.M., Smith, J.R., 2009. Paleoenvironmental reconstruction and water balance of a mid-Pleistocene pluvial lake, Dakhleh Oasis, Egypt. Geol. Soc. Am. Bull. 121, 1154–1171.

Kindermann, K., Bubenzer, O., Nussbaum, S., Riemer, H., Darius, F., Pöllath, N. and Smettan, U., 2006. Palaeoenvironment and holocene land use of Djara, western desert of Egypt. Quat. Sci. Rev. 25(13). 1619–1637.

Kleindienst, M. R., Schwarcz, H. R, Nicoll, K., Churcher, C. S. Frizano, J., Giegangack, R. W, and Wiseman, M. E., 1996. Pleistocene geochronology and paleoclimates at Dakhleh Oasis and Kharga Oasis, Western Desert, Egypt based upon uranium-thorium determinations from water-laid tufas. Nyame Akuma 46. 96.

Kleindienst, M.R., Blackwell, B.A.B., Skinner, A.R., Churcher, C.S., Kieniewicz, J.M., Smith, J.R., Wise, N.L., Long, R.A., Deely, A.E., Blickstein, J.I.B. and Chen, K.K.L., 2016. Assessing long-term habitability at an eastern Sahara oasis: ESR dating of molluscs and herbivore teeth at Dakhleh Oasis, Egypt. Quat. Int. In press.

Klitszch, E., List, F.K., Pohlmann, G., 1987. Geological Map of Egypt. Conoco Coral and Egyptian General Petroleum Company, Cairo, Egypt, 24 Sheets, scale 1:500,000

Kochel, R.G., Piper, J.F., 1986. Morphology of large valleys on Hawaii: Evidence for groundwater sapping and comparisons with Martian valleys, in: Lunar and Planetary Science Conference Proceedings. p. 175.

Konrad, R., Katharina, K., Bernd, R., Werner, S., Ludwig, Z., 2004. Alluvial loess in the Central Sinai: occurrence, origin, and palaeoclimatological consideration. Paleoecology of Quaternary Drylands. Springer, Berlin/Heidelberg. 79– 99.

Kröpelin, S., 1993. Geomorphology, landscape evolution and paleoclimates of southwest Egypt. Catena Suppl. 26, 31–66.

Kuss, J., Scheibner, C., Gietl, R., 2000. Carbonate platform to basin transition along an upper Cretaceous to lower tertiary Syrian Arc uplift, Galala Plateaus, Eastern Desert, Egypt. GeoArabia 5, 405–424.

Laity, J., 1988. The role of groundwater sapping in valley evolution on the Colorado Plateau. Sapping Featur. Color. Plateau. 63–70.

Laity, J.E., Malin, M.C., 1985. Sapping processes and the development of theater-headed valley networks on the Colorado Plateau. Geol. Soc. Am. Bull. 203–217.

Lamb, M.P., Howard, A.D., Johnson, J., Whipple, K.X., Dietrich, W.E., Perron, J.T., 2006. Can springs cut canyons into rock? J. Geophys. Res. Planets 111.

Lamb, M.P., Dietrich, W.E., Aciego, S.M., Depaolo, D.J., Manga, M., 2008. Formation of Box Canyon, Idaho, by megaflood: implications for seepage erosion on Earth and Mars. Science 320, 1067–1070. doi:10.1126/science.1156630

Lamb, M.P., Dietrich, W.E., 2009. The persistence of waterfalls in fractured rock. Geol. Soc. Am. Bull. 121, 1123–1134.

Lamb, M.P., Mackey, B.H., Farley, K.A., 2014. Amphitheater-headed canyons formed by megaflooding at Malad Gorge, Idaho. Proc. Natl. Acad. Sci. U. S. A. 111, 57–62. doi:10.1073/pnas.131225111.

Lehmann, K.K., Berden, G., Engeln, R., 2009. An introduction to cavity ringdown spectroscopy. Cavity Ringdown Spectrosc. Tech. Appl. G.Berden R.Engeln, eds. (Wiley, 2009) 1–26.

Li, C., Liu, L., Wang, J., Zhao, C., Wang, R., 2004. Comparison of two methods of the fusion of remote sensing images with fidelity of spectral information, in: Geoscience and Remote Sensing Symposium, 2004. IGARSS'04. Proceedings. 2004 IEEE International. IEEE, pp. 2561–2564.

Linstädter, J. and Kröpelin, S., 2004. Wadi Bakht revisited: Holocene climate change and prehistoric occupation in the Gilf Kebir region of the Eastern Sahara, SW Egypt. Geoarchaeology 19(8). 753 –778.

Luo, W., 2000. Quantifying groundwater sapping landforms with a hypsometric technique. J. Geophys. Res. Planets 105, 1685–1694.

Luo, W., Arvidson, R.E., Sultan, M., Becker, R., Crombie, M.K., Sturchio, N., El Alfy, Z., 1997. Ground-water sapping processes, Western Desert, Egypt. Geol. Soc. Am. Bull. 109, 43–62. doi:10.1130/0016-7606(1997)109<0043

Luo, W., Howard, A.D., 2008. Computer simulation of the role of groundwater seepage in forming Martian valley networks. J. Geophys. Res. Planets 113.

Malin, M.C., Edgett, K.S., 2000. Evidence for recent groundwater seepage and surface runoff on Mars. Science 288, 2330–2335. doi:8640 [pii]

Marra, W.A., Braat, L., Baar, A.W., Kleinhans, M.G., 2014. Valley formation by groundwater seepage, pressurized groundwater outbursts and crater-lake overflow in flume experiments with implications for Mars. Icarus 232, 97–117.

Marra, W.A., McLelland, S. J., Parsons, D. R., Murphy, B. J., Hauber, E., and Kleinhans, M. G., 2015. Groundwater seepage landscapes from distant and local sources in experiments and on Mars. Earth Surf. Dyn. 3, 389–408.

Martınez-Casasnovas, J.A., Ramos, M.C., Poesen, J., 2004. Assessment of sidewall erosion in large gullies using multi-temporal DEMs and logistic regression analysis. Geomorphology 58, 305–321.

Mastronuzzi, G., Sansò, P., 2002. Pleistocene sea level changes, sapping processes and development of valley networks in the Apulia region (southern Italy). Geomorphology 46, 19–34.

Maxwell, T.A., 1982. Erosional patterns of the Gilf Kebir Plateau and implications of the origin of martian Canyonlands, in El-Baz, F., and Maxwell, T. A., (eds.), Desert landforms of southwest Egypt; A basis for comparison with Mars: National Aeronautics and Space Adminstration CR-3611, pp. 281-300.

McCauley, J.F., Schaber, G.G., Breed, C.S., Grolier, M.J., Haynes, C.V, Issawi, B., Elachi, C., Blom, R., 1982. Subsurface valleys and geoarcheology of the eastern sahara revealed by shuttle radar. Science 218, 1004–1020. doi:218/4576/1004

McEwen, A. S., Keszthelyi, L. P. and Grant, J. A., 2012. Have there been large, recent (Mid-Late Amazonian) water floods on Mars? Lunar and Planetary Science Conference. 43, 1612.

McEwen, A.S., Dundas, C.M., Mattson, S.S., Toigo, A.D., Ojha, L., Wray, J.J., Chojnacki, M., Byrne, S., Murchie, S.L., Thomas, N., 2014. Recurring slope lineae in equatorial regions of Mars. Nature Geoscience 7, 53–58.

McLaren, S.J., Al-Juaidi, F., Bateman, M.D., Millington, A.C., 2009. First evidence for episodic flooding events in the arid interior of central Saudi Arabia over the last 60 ka. J. Quat. Sci. 24, 198–207.

Mohamed, A., Sultan, M., Ahmed, M., Eugene, Y.A., 2015. Towards a better understanding of the hydrologic setting of the Nubian Sandstone Aquifer System: Inferences from groundwater flow models, CL-36 ages, and GRACE data. AGU, San Fransisco.

Montgomery, D.R., Gillespie, A., 2005. Formation of Martian outflow channels by catastrophic dewatering of evaporite deposits. Geology 33, 625–628.

Montgomery, D.R., Som, S.M., Jackson, M.P.A., Schreiber, B.C., Gillespie, A.R., Adams, J.B., 2009. Continental-scale salt tectonics on Mars and the origin of Valles Marineris and associated outflow channels. Geol. Soc. Am. Bull. 121, 117–133.

Moustafa, A.R., 2002. Structural style and timing of Syrian Arc deformation in northern Egypt, in: Abstracts, American Association of Petroleum Geologists, International Conference, Cairo.

Nash, D.J., 1996. Groundwater sapping and valley development in the Hackness Hills, North Yorkshire, England. Earth Surf. Process. Landforms 21, 781–795.

Neev, D., Hall, J.K., 1982. A global system of spiraling geosutures. J. Geophys. Res. Solid Earth 87, 10689–10708.

Neev, D., Hall, J.K., Saul, J.M., 1982. The Pelusium megashear system across Africa and associated lineament swarms. J. Geophys. Res. Solid Earth 87, 1015–1030.

New, M., Hulme, M., Jones, P., 2000. Representing twentieth-century space-time climate variability. Part II: Development of 1901–96 monthly grids of terrestrial surface climate. J. Clim. 13, 2217–2238.

Nicoll, K., 1998. Holocene playas as sedimentary evidence for recent climate change in the presently hyperarid Western Desert, Egypt. PhD Thesis, University of Arizona, 291 pp.

Nicoll, K., Giegengack, R., Kleindienst, M., 1999. Petrogenesis of artifact-bearing fossil spring tufa deposits from Kharga Oasis, Egypt. Geoarchaeology 14, 849–863.

O'Callaghan, J.F., Mark, D.M., 1984. The extraction of drainage networks from digital elevation data. Comput. vision, Graph. image Process. 28, 323–344.

Onda, Y., 1994. Seepage erosion and its implication to the formation of amphitheatre valley heads: a case study at Obara, Japan. Earth Surf. Process. Landforms 19, 627–640.

Osmond, J.K. and Dabous, A.A., 2004. Timing and intensity of groundwater movement during Egyptian Sahara pluvial periods by U-series analysis of secondary U in ores and carbonates. Quat. Res. 61.85–94.

Pachur, H. -J ., and Braun, G. (1980). The paleoclimate of the central Sahara, Libya, and the Libyan Desert. Paieoecology of Africa and the Surrounding Islands 12. 351–363.

Pachur, H.J. and Hoelzmann, P., 1991. Paleoclimatic implications of late Quaternary lacustrine sediments in western Nubia, Sudan. Quat. Res. 36. 257–276.

Pachur, H. J., Hoelzmann, P., 2000. Late Quaternary palaeoecology and palaeoclimates of the eastern Sahara. J. African Earth Sci. 30, 929–939.

Paillou, P., Grandjean, G., Baghdadi, N., Heggy, E., August-Bernex, T., Achache, J., 2003. Subsurface imaging in south-central Egypt using low-frequency radar: bir safsaf revisited. IEEE Trans. Geosci. Remote Sens. 41, 1672–1684. doi:10.1109/TGRS.2003.813275

Paillou, P., Bernard, D., Radebaugh, J., Lorenz, R., Le Gall, A., Farr, T., 2014. Modeling the SAR backscatter of linear dunes on Earth and Titan. Icarus 230, 208–214.

Patterson, L.J., Sturchio, N.C., Kennedy, B.M., van Soest, M.C., Sultan, M., Lu, Z., Lehmann, B., Purtschert, R., El Alfy, Z., El Kaliouby, B., 2005. Cosmogenic, radiogenic, and stable isotopic constraints on groundwater residence time in the Nubian Aquifer, Western Desert of Egypt. Geochemistry, Geophys. Geosystems 6.1-19.

Pedrera, A., Pérez-Peña, J.V., Galindo-Zaldívar, J., Azañón, J.M., Azor, A., 2009. Testing the sensitivity of geomorphic indices in areas of low-rate active folding (eastern Betic Cordillera, Spain). Geomorphology 105, 218–231.

Pelletier, J.D., Baker, V.R., 2011. The role of weathering in the formation of bedrock valleys on Earth and Mars: A numerical modeling investigation. J. Geophys. Res. Planets 116.

Petit-Maire, N. (1980). Holocene biogeographical variations along the northwestern African coast (28-19 N): Paleoclimatic implications. Paieoecology of Africa and the Surrounding Islands 12. 365–377.

Prell, W.L. and Kutzbach, J.E., 1987. Monsoon variability over the past 150,000 years. J. Geophys.Res. Atmospheres 92, 8411–8425.

Prendergast, A.L., Stevens, R.E., O'Connell, T.C., Fadlalak, A., Touati, M., Al-Mzeine, A., Schöne, B.R., Hunt, C.O. and Barker, G., 2016. Changing patterns of eastern Mediterranean shellfish exploitation in the Late Glacial and Early Holocene: Oxygen isotope evidence from gastropod in Epipaleolithic to Neolithic human occupation layers at the Haua Fteah cave, Libya. Quat. Int. 407. 80-93.

Prescott, J.R., Hutton, J.T., 1994. Cosmic ray contributions to dose rates for luminescence and ESR dating: large depths and long-term time variations. Radiat. Meas. 23. 497–500.

Rayan, A., Fernandes, R.M.S., Khalil, H.A., Mahmoud, S., Miranda, J.M., Tealab, A., 2010. Evaluation of the crustal deformations in the northern region of Lake

Nasser (Egypt) derived from 8 years of GPS campaign observations. J. Geodyn. 49, 210–215.

REGWA, 1990. Hydrogeological inventory and groundwater development plan, western Nile Delta Region. Internal report.

RIGW, 1992. Groundwater resources and projection of groundwater development, Water Security Project. National Water Research Center, Egypt, 37 pp.

Robinson, C.A., 2002. Application of satellite radar data suggest that the Kharga Depression in south-western Egypt is a fracture rock aquifer. Int. J. Remote Sens. 23, 4101–4113.

Rosenberg, T.M., Preusser, F., Risberg, J., Plikk, A., Kadi, K.A., Matter, A. and Fleitmann, D. 2013. Middle and Late Pleistocene humid periods recorded in palaeolake deposits of the Nafud desert, Saudi Arabia. Quat.Sci. Rev.70, 109–123.

Rossi, A.P., Neukum, G., Pondrelli, M., van Gasselt, S., Zegers, T., Hauber, E., Chicarro, A., Foing, B., 2008. Large-scale spring deposits on Mars? J. Geophys. Res. Planets 113.

Said, R., 1962. The geology of Egypt. Elseveir, Amsterdam.

Said, R., 1979. The Messinian in Egypt. Proc.Intern.Congr.Mediterranean Neogene, Athens.Ann.Geol.Pays Hell. Hors Ser., Fasc 101, 1083–1090.

Said, R., 1983. Proposed classification of the Quaternary of Egypt. J. African Earth Sci. 1, 41–45.

Saleh, S., 2011. Subsurface structural mapping of Northern Nasser Lake region, Aswan, Egypt, using Bouguer data. Contrib. to Geophys. Geod. 41, 45–72.

Salem, O., Pallas, P., 2004. The Nubian Sandstone Aquifer System (NSAS). In: Appelgren B (ed) Managing shared aquifer resources in Africa. ISARM-Africa. IHP-VI, Series on Groundwater no. 8, UNESCO, Paris, 19–22.

Salman, A.B., Howari, F.M., El-Sankary, M.M., Wali, A.M., Saleh, M.M., 2010. Environmental impact and natural hazards on Kharga Oasis monumental sites, Western Desert of Egypt. J. African Earth Sci. 58, 341–353.

Sanz-Montero, M.E., Wanas, H., Muñoz-García, M.B., González-Acebrón, L., López, M. V, 2013. The uppermost deposits of the stratigraphic succession of the Farafra Depression (Western Desert, Egypt): Evolution to a Post-Eocene continental event. J. African Earth Sci. 87, 33–43.

Schaber, G.G., McCauley, J.F., Breed, C.S., 1997. The use of multifrequency and polarimetric SIR-C/X-SAR data in geologic studies of Bir Safsaf, Egypt. Remote Sens. Environ. 59, 337–363.

Schumm, S.A., Boyd, K.F., Wolff, C.G., Spitz, W.J., 1995. A ground-water sapping landscape in the Florida Panhandle. Geomorphology 12, 281–297.

Schumm, S.A., Phillips, L., 1986. Composite channels of the Canterbury Plain, New Zealand: A martian analog? Geology 14, 326–329.

Shata, A.A., 1982. Hydrogeology of the great Nubian Sandstone basin, Egypt. Q. J. Eng. Geol. Hydrogeol. 15, 127–133.

Simpkins, W.W., and Baumgardner, R.W., 1982. Stream incision and scarp retreat rates based on volcanic ash date from the Seymour Formation, in: Gustavson, T.C. (Eds.), Geology and Geohydrology of the Palo Duro Basin, Texas Panhandle—A Report on the Progress of Nuclear Waste Isolation Feasibility Studies (1981). University of Texas at Austin, Bureau of Economic Geology, Austin, 160–163.

Smith, S.E., 1986. An assessment of structural deterioration on ancient Egyptian monuments and tombs in Thebes. J. F. Archaeol. 13, 503–501.

Smith, J.R., 2001. Geoarchaeology, stable-isotope geochemistry, and geochronology of fossil-spring tufas, Western Desert, Egypt. PhD Thesis, University of Pennsylvania, Philadelphia, 180 pp.

Smith, J.R., Giegengack, R., Schwarcz, H.P., 2004a. Constraints on Pleistocene pluvial climates through stable-isotope analysis of fossil-spring tufas and associated gastropods, Kharga Oasis, Egypt. Palaeogeogr. Palaeoclimatol. Palaeoecol. 206, 157–175.

Smith, J.R., Giegengack, R., Schwarcz, H.P., McDonald, M.M., Kleindienst, M.R., Hawkins, A.L., Churcher, C.S., 2004b. A reconstruction of Quaternary pluvial environments and human occupations using stratigraphy and geochronology of fossil-spring tufas, Kharga Oasis, Egypt. Geoarchaeology 19, 407–439.

Smith, J.R., Hawkins, A.L., Asmerom, Y., Polyak, V. and Giegengack, R., 2007. New age constraints on the Middle Stone Age occupations of Kharga Oasis, Western Desert, Egypt. J. Human Evol. 52. 690–701.

Sonntag, C., Muennich, K.O., Junghans, C., Klitzsch, E., Thorweihe, U., Weistroffer, K., Loehnert, E.P., Swailem, F.M., 1978. Paleoclimatic information from deuterium and oxygen-18 in C-14 dated north Saharian groundwaters. In: Isotope Hydrology, 978. International Atomic Energy Agency, Vienna, 569–580.

Squyres, C.H., Bradley, W., 1964. Notes on the Western Desert of Egypt, in: Conference Petroleum Exploration Society, Libya. 99–105.

Stern, R.J., 1985. The Najd Fault System, Saudi Arabia and Egypt: A Late Precambrian rift-related transform system? Tectonics 4, 497–511.

Stöckl, L., 2010. Hydrological and hydrochemical controls on radioactivity in deep groundwater in Saudi Arabia. Master Thesis, Albert-Luwigs Universitat Freiburg. 79 pp.

Stuiver, M., Polach, H.A., 1977. Discussion; reporting of C-14 data. Radiocarbon 19, 355–363.

Sturchio, N.C., Arehart, G.B., Sultan, M., Sano, Y., AboKamar, Y., Sayed, M., 1996. Composition and origin of thermal waters in the Gulf of Suez area, Egypt. Appl. Geochemistry 11, 471–479.

Sturchio, N.C., Du, X., Purtschert, R., Lehmann, B.E., Sultan, M., Patterson, L.J., Lu, Z., Müller, P., Bigler, T., Bailey, K., 2004. One million year old groundwater in the Sahara revealed by krypton-81 and chlorine-36. Geophys. Res. Lett. 31.

Sultan, M., Arvidson, R.E., Duncan, I.J., Stern, R.J., El Kaliouby, B., 1988. Extension of the Najd shear system from Saudi Arabia to the central Eastern Desert of Egypt based on integrated field and Landsat observations. Tectonics 7, 1291–1306.

Sultan, M., Becker, R., Arvidson, R.E., Shore, P., Stern, R.J., El Alfy, Z., Attia, R.I., 1993. New constraints on Red Sea rifting from correlations of Arabian and Nubian Neoproterozoic outcrops. Tectonics 12, 1303–1319.

Sultan, M., Sturchio, N., Hassan, F.A., Hamdan, M.A.R., Mahmood, A.M., El Alfy, Z., Stein, T., 1997. Precipitation source inferred from stable isotopic composition of Pleistocene groundwater and carbonate deposits in the Western desert of Egypt. Quat. Res. 48, 29–37.

Sultan, M., Sturchio, N.C., Gheith, H., Hady, Y.A., Anbeawy, M., 2000. Chemical and Isotopic Constraints on the Origin of Wadi El-Tarfa Ground Water, Eastern Desert, Egypt. Groundwater 38, 743–751.

Sultan, M., Yan, E., Sturchio, N., Wagdy, A., Gelil, K.A., Becker, R., Manocha, N., Milewski, A., 2007. Natural discharge: a key to sustainable utilization of fossil groundwater. J. Hydrol. 335, 25–36.

Sultan, M., Yousef, A.F., Metwally, S.E., Becker, R., Milewski, A., Sauck, W., Sturchio, N.C., Mohamed, A.M.M., Wagdy, A., El Alfy, Z., 2011. Red Sea rifting controls on aquifer distribution: Constraints from geochemical, geophysical, and remote sensing data. Geol. Soc. Am. Bull. 123, 911–924.

Sultan, M., Emil, M., Abotalib, Z.A., Abouelmagd, A., Alzahrani, A., Refai, A., AlQthamy, Kh., Alaamry, M., Bahamil, A.M., 2015. Nature and timing of the Quaternary wet climatic periods in North Africa and Arabia: isotopic, chronologic, and remote sensing constraints. GSA abstract with programs.

Swezey, C.S., 1996. Structural controls on Quaternary depocentres within the Chotts Trough region of southern Tunisia. J. African Earth Sci. 22, 335–347.

Szabo, B.J., Haynes, C.V, Maxwell, T.A., 1995. Ages of Quaternary pluvial episodes determined by uranium-series and radiocarbon dating of lacustrine deposits of Eastern Sahara. Palaeogeogr. Palaeoclimatol. Palaeoecol. 113, 227–242.

Tarboton, D.G., 1997. A new method for the determination of flow directions and upslope areas in grid digital elevation models. Water Resour. Res. 33, 309–319.

Teng, J., Vaze, J., Tuteja, N.K., Gallant, J.C., 2008. A GIS-Based Tool for Spatial and Distributed Hydrological Modelling: CLASS Spatial Analyst. Trans. GIS 12, 209–225.

Tewksbury, B.J., Hogan, J.P., Kattenhorn, S.A., Mehrtens, C.J., Tarabees, E.A., 2014. Polygonal faults in chalk: Insights from extensive exposures of the Khoman Formation, Western Desert, Egypt. Geology 42, 479–482.

Thompson, A., 2007. Water resources of the Al Fayoum area, Egypt. Master Thesis, University of Illinois at Chicago, 43 pp.

Thorweihe, U., 1990. Nubian aquifer system. Geol. Egypt 601–614.

Thorweihe, U., Heinl, M., 2002. Groundwater resources of the Nubian aquifer system. Aquifers major basins–non-renewable water Resour. Modif. Synth.

Thurmond, A.K., Stern, R.J., Abdelsalam, M.G., Nielsen, K.C., Abdeen, M.M., Hinz, E., 2004. The Nubian Swell. J. African Earth Sci. 39, 401–407.

Torab, M. 2013. Geomorphology of fossil springs mounds in some selected portions of Western Desert oases of Egypt, The 2nd Intl Symposium on Kaz Mountains (Mt. Ida) and Edremit (Edremit-Balikesir.

Treiman, A.H., 2008. Ancient groundwater flow in the Valles Marineris on Mars inferred from fault trace ridges. Nat. Geosci. 1, 181–183.

Vogel, J.S., Southon, J.R., Nelson, D.E., Brown, T.A., 1984. Performance of catalytically condensed carbon for use in accelerator mass spectrometry. Nucl. Instruments Methods Phys. Res. Sect. B Beam Interact. with Mater. Atoms 5, 289–293.

Wanas, H.A., 2012. Pseudospherulitic fibrous calcite from the Quaternary shallow lacustrine carbonates of the Farafra Oasis, Western Desert, Egypt: A primary precipitate with possible bacterial influence. J. African Earth Sci. 65, 105–114.

Wendorf, F., Schild, R., 1980. Prehistory of the eastern Sahara. Academic Press.

Wendorf, F., Schild, R., Close, A.E., 1984. Cattle-keepers of the eastern Sahara: the neolithic of Bir Kiseiba. Department of Anthropology [and] Institute for the Study of Earth and Man, Southern Methodist University.

Wendorf, F., Schild, R., Close, A.E., Schwarcz, H.P., Miller, G.H., Grün, R., Bluszcz, A., Stokes, S., Morawska, L., Huxtable, J., and Lundberg, J., 1994. A chronology for the Middle and Late Pleistocene wet episodes in the eastern Sahara. Late Quaternary chronology and paleoclimates of the Eastern Mediterranean. 147–168.

Wescott, W.A., Atta, M., Blanchard, D.C., Cole, R.M., Georgeson, S.T., Miller, D.A., O'Hayer, W.W., Wilson, A.D., Dolson, J.C., Sehim, A., 2011. Jurassic Rift Architecture in the Northeastern Western Desert, Egypt. AAPG Search and Discovery Article #10379, from poster presentation at AAPG International Conference and Exhibition, Milan, Italy.

Wood, W.W., 2002. Role of ground water in geomorphology, geology, and paleoclimate of the Southern High Plains, USA. Groundwater 40, 438–447.

Wüst, R.A.J., Schlüchter, C., 2000. The origin of soluble salts in rocks of the Thebes mountains, Egypt: The damage potential to ancient Egyptian wall art. J. Archaeol. Sci. 27, 1161–1172.

Yan, Z., Petit-Maire, N., 1994. The last 140 ka in the Afro-Asian arid/semi-arid transitional zone. Palaeogeogr. Palaeoclimatol. Palaeoecol. 110, 217–233.

Yang, X., Scuderi, L.A., Wang, X., Scuderi, L.J., Zhang, D., Li, H., Forman, S., Xu, Q., Wang, R., Huang, W., Yang, S., 2015. Groundwater sapping as the cause of irreversible desertification of Hunshandake Sandy Lands, Inner Mongolia, northern China. Proc. Natl. Acad. Sci. USA. 112, 702–706.

Zaher, M.A., Senosy, M.M., Youssef, M.M., Ehara, S., 2009. Thickness variation of the sedimentary cover in the South Western Desert of Egypt as deduced from Bouguer gravity and drill-hole data using neural network method. Earth, planets Sp. 61, 659–674.

APPENDIX A

Isotopic composition of Quaternary deposits in the Eastern Sahara and inferred isotopic composition of the waters from which these deposits were formed

Carbonates Oxygen 18 and Carbon 13 ‰			**Water Oxygen 18 (SMOW) ‰ at different temperatures**			**Author**
PDB	**SMOW**	**Carbon 13**	**T 17.5**	**T 19.75**	**T 22**	
Crystal Mountain						
-11.4116	19.44838	-0.09	-10.2378	-9.73836	-9.25012	Jimenez, 2014
-11.2054	19.65455	-0.93	-10.0376	-9.5381	-9.04975	Jimenez, 2014
-11.6178	19.24221	-2.59	-10.4379	-9.93863	-9.45049	Jimenez, 2014
-11.0921	19.76795	-11.47	-9.92749	-9.42795	-8.93955	Jimenez, 2014
-11.0817	19.77826	-10.77	-9.91748	-9.41793	-8.92953	Jimenez, 2014
-11.8033	19.05665	-10.2	-10.6181	-10.1189	-9.63082	Jimenez, 2014
-12.7517	18.10826	-8.24	-11.5388	-11.0401	-10.5525	Jimenez, 2014
Dakhla Oasis						
-10.5972	20.26276	-4.72	-9.44709	-8.9473	-8.45866	Jimenez, 2014
-10.6282	20.23183	-4.3	-9.47711	-8.97734	-8.48872	Jimenez, 2014
-10.422	20.43801	-4.43	-9.27694	-8.77707	-8.28835	Jimenez, 2014
-9.45299	21.40701	-5.92	-8.33615	-7.83581	-7.34662	Jimenez, 2014
-7.82423	23.03577	-5.47	-6.75482	-6.25368	-5.76371	Jimenez, 2014
-8.00978	22.85022	-5.47	-6.93497	-6.43392	-5.94405	Jimenez, 2014
-11.5972	19.26283	-3.56	-10.4179	-9.91861	-9.43045	Smith, 2001
-9.3499	21.5101	-1.17	-8.23607	-7.73567	-7.24644	Smith, 2001
-9.23651	21.62349	-0.03	-8.12598	-7.62552	-7.13624	Smith, 2001
-7.97886	22.88114	-6.12	-6.90495	-6.40388	-5.91399	Smith, 2001
-7.71083	23.14917	-1.86	-6.64473	-6.14353	-5.65351	Smith, 2001
-9.24681	21.61319	-4.25	-8.13598	-7.63554	-7.14625	Smith, 2001
-9.28805	21.57195	-3.46	-8.17602	-7.67559	-7.18633	Smith, 2001
-9.56638	21.29362	-5.01	-8.44624	-7.94595	-7.45682	Smith, 2001
-10.0303	20.82973	-4.58	-8.89662	-8.39656	-7.90765	Smith, 2001
-10.7725	20.08751	-1.46	-9.61723	-9.11753	-8.62898	Smith, 2001
-11.7312	19.12881	-0.84	-10.548	-10.0488	-9.56069	Smith, 2001

-11.3085	19.55147	-9.47	-10.1377	-9.63823	-9.14993	Smith, 2001
-9.78286	21.07714	-2.21	-8.65642	-8.15624	-7.66721	Smith, 2001
Refuf Pass						
-11.1024	19.75764	-5.15	-9.9375	-9.43796	-8.94957	Jimenez, 2014
-11.0714	19.78856	-4.95	-9.90747	-9.40792	-8.91951	Jimenez, 2014
-8.90663	21.95337	-3.21	-7.80571	-7.30509	-6.81565	Jimenez, 2014
-10.1437	20.71634	-3.82	-9.00672	-8.50671	-8.01786	Jimenez, 2014
-10.3808	20.47924	-2.81	-9.23691	-8.73702	-8.24828	Jimenez, 2014
-10.2571	20.60294	-1.79	-9.11681	-8.61686	-8.12806	Jimenez, 2014
-10.3292	20.53078	-2.6	-9.18687	-8.68695	-8.19819	Jimenez, 2014
-10.8756	19.98443	-3.07	-9.71731	-9.21766	-8.72916	Jimenez, 2014
-11.0817	19.77826	-3.47	-9.91748	-9.41793	-8.92953	Jimenez, 2014
-11.2776	19.58239	-4.32	-10.1076	-9.60819	-9.11988	Jimenez, 2014
-10.7931	20.0669	-2.1	-9.63725	-9.13756	-8.64901	Jimenez, 2014
-10.3705	20.48955	-0.92	-9.2269	-8.727	-8.23826	Jimenez, 2014
-11.3498	19.51023	-2.9	-10.1777	-9.67828	-9.19001	Jimenez, 2014
-9.9478	20.9122		-8.81656	-8.31645	-7.82751	Sultan et al., 1997
-9.9478	20.9122		-8.81656	-8.31645	-7.82751	Sultan et al., 1997
Wadi Midauwara						
-9.33959	21.52041	-2.11	-8.22606	-7.72566	-7.23642	Jimenez, 2014
-10.7519	20.10813	-1.65	-9.59721	-9.0975	-8.60894	Jimenez, 2014
-9.43237	21.42763	-1.95	-8.31614	-7.81578	-7.32659	Jimenez, 2014
-9.76224	21.09776	-1.42	-8.6364	-8.13621	-7.64717	Jimenez, 2014
-9.45299	21.40701	-1.59	-8.33615	-7.83581	-7.34662	Jimenez, 2014
-10.0921	20.76788	-1.62	-8.95667	-8.45664	-7.96776	Jimenez, 2014
-11.824	19.03604	-1.29	-10.6381	-10.1389	-9.65085	Jimenez, 2014
-9.63854	21.22146	-0.69	-8.5163	-8.01605	-7.52695	Jimenez, 2014
-7.82423	23.03577	-0.86	-6.75482	-6.25368	-5.76371	Jimenez, 2014
-6.79337	24.06663	-1.69	-5.75398	-5.25233	-4.76187	Jimenez, 2014
-10.5766	20.28338	-2.36	-9.42707	-8.92727	-8.43863	Jimenez, 2014
-9.79317	21.06683	-0.58	-8.66643	-8.16625	-7.67723	Smith, 2001
-9.15404	21.70596	0.66	-8.04591	-7.54542	-7.05609	Smith, 2001
-9.98903	20.87097	-0.45	-8.85659	-8.35651	-7.86758	Smith, 2001
-7.6696	23.1904	-0.18	-6.6047	-6.10348	-5.61344	Smith, 2001
-9.8241	21.0359	-0.29	-8.69646	-8.19629	-7.70728	Smith, 2001

-10.1127	20.74726	-0.55	-8.97669	-8.47667	-7.9878	Smith, 2001
-9.65916	21.20084	-1.56	-8.53632	-8.03608	-7.54699	Smith, 2001
-9.61792	21.24208	-1.27	-8.49629	-7.99602	-7.50692	Smith, 2001
-9.29836	21.56164	-0.58	-8.18603	-7.6856	-7.19635	Smith, 2001
-9.38083	21.47917	-2.2	-8.26609	-7.76571	-7.27649	Smith, 2001
-10.9271	19.93288	-2.4	-9.76736	-9.26773	-8.77925	Smith, 2001
-11.659	19.20097	-0.06	-10.478	-9.97869	-9.49056	Smith, 2001
-8.95817	21.90183	0.92	-7.85575	-7.35516	-6.86574	Smith, 2001
-11.6075	19.25252	0.18	-10.4279	-9.92862	-9.44047	Smith, 2001
-11.7518	19.1082	-4.35	-10.568	-10.0688	-9.58073	Smith, 2001
-10.69	20.16998	-4.39	-9.53716	-9.03742	-8.54883	Smith, 2001
-9.44268	21.41732	-0.24	-8.32614	-7.82579	-7.3366	Smith, 2001
-8.14379	22.71621	1.17	-7.06508	-6.5641	-6.07428	Smith, 2001
-12.2672	18.59277	-5.13	-11.0684	-10.5695	-10.0816	Smith, 2001
-7.65929	23.20071	-0.79	-6.59469	-6.09346	-5.60342	Smith, 2001
-9.16435	21.69565	-2.21	-8.05592	-7.55543	-7.06611	Smith, 2001
-9.66947	21.19053	-0.93	-8.54633	-8.04609	-7.55701	Smith, 2001
-8.23657	22.62343	-0.45	-7.15516	-6.65422	-6.16445	Smith, 2001
-7.22633	23.63367	-0.06	-6.17433	-5.6729	-5.18265	Smith, 2001
-5.97899	24.88101	0.04	-4.96332	-4.46127	-3.97042	Smith, 2001
-6.48411	24.37589	0.71	-5.45373	-4.95193	-4.46132	Smith, 2001
-8.31904	22.54096	-0.3	-7.23523	-6.73433	-6.2446	Smith, 2001
-8.55614	22.30386	-0.38	-7.46542	-6.96464	-6.47502	Smith, 2001
-9.14373	21.71627	-0.17	-8.0359	-7.5354	-7.04607	Smith, 2001
-8.71077	22.14923	-0.52	-7.61555	-7.11484	-6.6253	Smith, 2001
Ain Amur						
-11.7209	19.13912	-0.82	-10.538	-10.0388	-9.55067	Smith, 2001
-12.1229	18.73709	-3.51	-10.9283	-10.4293	-9.94139	Smith, 2001
-12.5765	18.28351	-6.06	-11.3687	-10.8699	-10.3822	Smith, 2001
-11.9786	18.88141	-5.6	-10.7882	-10.2891	-9.80113	Smith, 2001
-10.4838	20.37615	-5.51	-9.33699	-8.83715	-8.34846	Smith, 2001
-9.72101	21.13899	-3.12	-8.59637	-8.09616	-7.6071	Smith, 2001
Matana						
-12.1023	18.7577	-3.28	-10.9083	-10.4093	-9.92135	Smith, 2001
-9.60762	21.25238	-1.64	-8.48628	-7.98601	-7.4969	Smith, 2001
-9.69008	21.16992	-0.99	-8.56635	-8.06612	-7.57705	Smith, 2001
-8.58706	22.27294	1.33	-7.49545	-6.99468	-6.50508	Smith, 2001

-11.3292	19.53085	-2.87	-10.1577	-9.65826	-9.16997	Smith, 2001
-11.5559	19.30406	-3.49	-10.3779	-9.87855	-9.39038	Smith, 2001
-11.5147	19.34529	-3.15	-10.3378	-9.8385	-9.3503	Smith, 2001
-10.0509	20.80912	-0.03	-8.91664	-8.41659	-7.92769	Smith, 2001
-9.85502	21.00498	-1.57	-8.72648	-8.22633	-7.73734	Smith, 2001
-8.83447	22.02553	-1.63	-7.73565	-7.235	-6.74552	Smith, 2001
-8.3912	22.4688	-0.93	-7.30529	-6.80442	-6.31473	Smith, 2001
-10.3086	20.5514	-2.36	-9.16685	-8.66692	-8.17815	Smith, 2001
Buluq						
-8.78293	22.07707	-2.06	-7.68561	-7.18493	-6.69543	Smith, 2001
-9.61792	21.24208	-2.93	-8.49629	-7.99602	-7.50692	Smith, 2001
-10.6797	20.18029	-1.74	-9.52715	-9.02741	-8.53881	Smith, 2001
Gebel El Yabisa						
-8.752	22.108		-7.65558	-7.15489	-6.66537	Sultan et al., 1997
-10.9374	19.92258		-9.77736	-9.27775	-8.78927	Sultan et al., 1997
-10.5148	20.34523		-9.36702	-8.86719	-8.37852	Sultan et al., 1997
-10.9374	19.92258		-9.77736	-9.27775	-8.78927	Sultan et al., 1997
-6.64905	24.21095		-5.61386	-5.11214	-4.62162	Sultan et al., 1997
-12.3394	18.52061		-11.1385	-10.6396	-10.1518	Sultan et al., 1997
-13.762	17.09802		-12.5197	-12.0214	-11.5343	Sultan et al., 1997
Gebel Agouz						
-4.94813	25.91187		-3.96247	-3.45992	-2.96858	Sultan et al., 1997
-11.5456	19.31437		-10.3679	-9.86854	-9.38036	Sultan et al., 1997
-8.14379	22.71621		-7.06508	-6.5641	-6.07428	Sultan et al., 1997
Kurkur Oasis						
-13.2981	17.56191	-1.5	-12.0693	-11.5708	-11.0835	Crombie et al., 1997

-14.1331	16.72691	-3	-12.88	-12.3819	-11.895	Crombie et al., 1997
-13.762	17.09802	-3.2	-12.5197	-12.0214	-11.5343	Crombie et al., 1997
-14.03	16.83	-3.2	-12.7799	-12.2818	-11.7948	Crombie et al., 1997
-13.4012	17.45882	-3.1	-12.1694	-11.671	-11.1837	Crombie et al., 1997
-13.9578	16.90216	-3.1	-12.7098	-12.2117	-11.7247	Crombie et al., 1997
-11.7312	19.12881	-3	-10.548	-10.0488	-9.56069	Crombie et al., 1997
-12.3188	18.54122	-1.2	-11.1185	-10.6195	-10.1317	Crombie et al., 1997
-10.3705	20.48955	0	-9.2269	-8.727	-8.23826	Crombie et al., 1997
-12.8754	17.98456	-1.4	-11.6589	-11.1603	-10.6727	Crombie et al., 1997
-10.154	20.70603	-3.3	-9.01672	-8.51672	-8.02787	Crombie et al., 1997
-9.36021	21.49979	-2.1	-8.24608	-7.74569	-7.25646	Crombie et al., 1997
-9.74163	21.11837	-1.6	-8.61639	-8.11618	-7.62714	Crombie et al., 1997
-12.3188	18.54122	-1.1	-11.1185	-10.6195	-10.1317	Crombie et al., 1997
-12.8239	18.0361	-0.69	-11.6089	-11.1102	-10.6226	Jimenez, 2014
-11.7518	19.1082	-0.42	-10.568	-10.0688	-9.58073	Jimenez, 2014
-13.8341	17.02586	-4.02	-12.5897	-12.0915	-11.6044	Jimenez, 2014
-11.3704	19.48961	-2.86	-10.1977	-9.69831	-9.21004	Jimenez, 2014
-9.9478	20.9122	-2.8	-8.81656	-8.31645	-7.82751	Jimenez, 2014
-11.5147	19.34529	-3.51	-10.3378	-9.8385	-9.3503	Jimenez, 2014
-8.81385	22.04615	-1.41	-7.71563	-7.21497	-6.72548	Jimenez, 2014
-11.2776	19.58239	-2.86	-10.1076	-9.60819	-9.11988	Jimenez, 2014
-9.23651	21.62349	-2.21	-8.12598	-7.62552	-7.13624	Jimenez, 2014
-9.77255	21.08745	-2.26	-8.64641	-8.14622	-7.65719	Jimenez, 2014
-11.1024	19.75764	-2.94	-9.9375	-9.43796	-8.94957	Jimenez, 2014
-10.8653	19.99474	-3.3	-9.70731	-9.20765	-8.71914	Jimenez, 2014
-13.2569	17.60314	-4.53	-12.0293	-11.5308	-11.0434	Jimenez, 2014
-11.3601	19.49992	-2.49	-10.1877	-9.6883	-9.20003	Jimenez, 2014

-13.3084	17.5516	-4	-12.0793	-11.5808	-11.0935	Jimenez, 2014
-8.41182	22.44818	-2.39	-7.3253	-6.82445	-6.33476	Jimenez, 2014
-8.89632	21.96368	-2.02	-7.7957	-7.29508	-6.80563	Jimenez, 2014
-9.23651	21.62349	-2.26	-8.12598	-7.62552	-7.13624	Jimenez, 2014
-8.5149	22.3451	-1.49	-7.42539	-6.92458	-6.43495	Jimenez, 2014
-12.4219	18.43814	-1.16	-11.2186	-10.7197	-10.2319	Jimenez, 2014

APPENDIX B

Age dating of lacustrine, travertine and tufa deposits in the Sahara

Author	Age	Error	Author	Age	Error
Jimenez, 2014	525289	29793	Kindermann et al., 2006	6597	0
Jimenez, 2014	1398928	181479	Kindermann et al., 2006	6448	0
Jimenez, 2014	1015941	119370	Kindermann et al., 2006	6430	0
Jimenez, 2014	350962	6053	Kindermann et al., 2006	6406	0
Jimenez, 2014	294247	4751	Kindermann et al., 2006	6365	0
Jimenez, 2014	451504	10520	Kindermann et al., 2006	5982	0
Jimenez, 2014	602170	63819	Kindermann et al., 2006	5866	0
Jimenez, 2014	130495	552	Hamdan and Lucarini, 2013	10721	325
Jimenez, 2014	125946	583	Hamdan and Lucarini, 2013	8079	254
Jimenez, 2014	132602	741	Hamdan and Lucarini, 2013	8773	160
Jimenez, 2014	545835	35391	Hamdan and Lucarini, 2013	9544	5
Jimenez, 2014	431845	9565	Hamdan and Lucarini, 2013	8896	86
Jimenez, 2014	450007	13928	Hamdan and Lucarini, 2013	8528	61
Jimenez, 2014	498445	21382	Hamdan and Lucarini, 2013	8329	113
Jimenez, 2014	647743	60676	Hamdan and Lucarini, 2013	7624	30
Jimenez, 2014	181052	1560	Hamdan and Lucarini, 2013	7286	94
Jimenez, 2014	160899	870	Hamdan and Lucarini, 2013	7510	107
Jimenez, 2014	105362	402	Hamdan and Lucarini, 2013	7254	64
Jimenez, 2014	567468	50194	Hamdan and Lucarini, 2013	7227	39
Jimenez, 2014	602000	74659	Hamdan and Lucarini, 2013	7217	36
Jimenez, 2014	730173	120378	Hamdan and Lucarini, 2013	7079	62

Jimenez, 2014	916772	119591	Hamdan and Lucarini, 2013	6407	84
Jimenez, 2014	792803	119591	Hamdan and Lucarini, 2013	6144	98
Jimenez, 2014	128463	949	Hamdan and Lucarini, 2013	7079	62
Jimenez, 2014	78699	635	Hamdan and Lucarini, 2013	4517	131
Jimenez, 2014	145706	763	Hamdan and Lucarini, 2013	7536	24
Jimenez, 2014	247775	2665	Hamdan and Lucarini, 2013	7353	123
Jimenez, 2014	516287	29730	Hamdan and Lucarini, 2013	7671	55
Jimenez, 2014	612096	119416	Churcher et al., 1999	8000	0
Jimenez, 2014	846334	119416	Churcher et al., 1999	11000	0
Jimenez, 2014	193533	3445	Churcher et al., 1999	40000	10000
Jimenez, 2014	1026277	119416	Churcher et al., 1999	125000	1600
Jimenez, 2014	147753	894	Churcher et al., 1999	220000	20000
Pachur and Braun, 1980			Smith et al., 2007	127748	1386
Pachur and Braun, 1980	16740	400	Smith et al., 2007	129808	5058
Pachur and Braun, 1980	16920	400	Smith et al., 2007	127892	1300
Pachur and Braun, 1980	30750	460	Smith et al., 2007	114395	4193
Pachur and Braun, 1980	18070	215	Smith et al., 2007	124567	3383
Pachur and Braun, 1980	35600	1750	Smith et al., 2007	127069	3826
Pachur and Braun, 1980	12050	255	Smith et al., 2007	125665	2500
Pachur and Braun, 1980	28050	340	Smith et al., 2007	123840	3645
Pachur and Braun, 1980	15710	185	Smith et al., 2007	137617	2629

Petit-Mair, 1980	22950	300	Smith et al., 2007	136358	3365
Petit-Mair, 1980	91950	20000	Smith et al., 2007	136039	2200
Petit-Mair, 1980	94450	7000	Smith et al., 2007	130532	2832
Petit-Mair, 1980	126950	11000	Osmond and Dabous, 2004	83000	6000
Petit-Mair, 1980	128950	13000	Osmond and Dabous, 2004	107000	9000
Petit-Mair, 1980	140950	14000	Osmond and Dabous, 2004	144000	14000
Petit-Mair, 1980	142950	12000	Osmond and Dabous, 2004	136000	13000
Petit-Mair, 1980	144950	12000	Osmond and Dabous, 2004	136000	12000
Petit-Mair, 1980	164950	20000	Osmond and Dabous, 2004	55000	4000
Fontes et al., 1983	21850	750	Osmond and Dabous, 2004	113000	10000
Fontes et al., 1983	26910	850	Osmond and Dabous, 2004	141000	15000
Fontes et al., 1983	22190	2500	Osmond and Dabous, 2004	65000	4000
Fontes et al., 1983	16100	380	Osmond and Dabous, 2004	34000	2000
Fontes et al., 1983	19980	400	Osmond and Dabous, 2004	81000	5000
Fontes et al., 1983	14410	820	Osmond and Dabous, 2004	127000	11000
Fontes et al., 1983	15150	570	Osmond and Dabous, 2004	83000	5000
Fontes et al., 1983	11620	900	Osmond and Dabous, 2004	117000	10000
Fontes et al., 1983	23700	1410	Osmond and Dabous, 2004	86000	6000
Fontes et al., 1983	24600	2400	Osmond and Dabous, 2004	110000	10000
Fontes et al., 1983	31750	1490	Osmond and Dabous, 2004	115000	10000
Fontes et al., 1983	12010	200	Osmond and Dabous, 2004	75000	6000

Szabo et al., 1995	288950	40000	Osmond and Dabous, 2004	111000	10000
Szabo et al., 1995	227950	11000	Osmond and Dabous, 2004	117000	10000
Szabo et al., 1995	19950	5000	Osmond and Dabous, 2004	181000	22000
Szabo et al., 1995	72950	4000	Osmond and Dabous, 2004	97000	6000
Szabo et al., 1995	79950	4000	Osmond and Dabous, 2004	78000	5000
Szabo et al., 1995	139950	4000	Osmond and Dabous, 2004	78000	5000
Szabo et al., 1995	156950	4000	Osmond and Dabous, 2004	27000	2000
Szabo et al., 1995	234950	15000	Osmond and Dabous, 2004	121000	11000
Szabo et al., 1995	278950	22000	Osmond and Dabous, 2004	110000	9000
Szabo et al., 1995	282950	25000	Osmond and Dabous, 2004	175000	21000
Szabo et al., 1995	351950	0	Osmond and Dabous, 2004	160000	18000
Szabo et al., 1995	156950	4000	Osmond and Dabous, 2004	181000	22000
Szabo et al., 1995	79950	4000	Osmond and Dabous, 2004	120000	10000
Szabo et al., 1995	135950	4000	Osmond and Dabous, 2004	222000	36000
Szabo et al., 1995	156950	4000	Osmond and Dabous, 2004	68000	4000
Kleindienst et al., 1996	301950	0	Osmond and Dabous, 2004	78000	5000
Kleindienst et al., 1996	241950	2500	Osmond and Dabous, 2004	212000	30000
Kleindienst et al., 1996	199950	2500	Osmond and Dabous, 2004	159000	15000
Kleindienst et al., 1996	175950	3500	Osmond and Dabous, 2004	176000	20000
Kleindienst et al., 1996	139950	1000	Osmond and Dabous, 2004	94000	7000
Kleindienst et al., 1996	126950	800	Osmond and Dabous, 2004	83000	6000

Kleindienst et al., 1996	167950	1000	Osmond and Dabous, 2004	78000	6000
Kleindienst et al., 1996	298950	5000	Smith et al., 2004a	49800	100
Kleindienst et al., 1996	305950	6500	Smith et al., 2004a	136000	3000
Kleindienst et al., 1996	238950	6500	Smith et al., 2004a	126000	4000
Kleindienst et al., 1996	215950	700	Smith et al., 2004a	140000	1200
Kleindienst et al., 1996	125950	300	Smith et al., 2004a	142000	300
Crombie et al., 1997	69950	2000	Smith et al., 2004a	103000	14000
Crombie et al., 1997	103950	6000	Smith et al., 2004a	150000	13000
Crombie et al., 1997	102950	5000	Smith et al., 2004a	359000	9000
Crombie et al., 1997	110950	6000	Linstadter and Kropelin, 2004	8200	500
Crombie et al., 1997	117950	6000	Linstadter and Kropelin, 2004	7980	90
Crombie et al., 1997	161950	8000	Linstadter and Kropelin, 2004	7405	125
Crombie et al., 1997	220950	13000	Linstadter and Kropelin, 2004	7145	100
Crombie et al., 1997	192950	15000	Linstadter and Kropelin, 2004	6870	65
Crombie et al., 1997	221950	25000	Linstadter and Kropelin, 2004	6080	420
Sultan et al., 1997	186950	15000	Linstadter and Kropelin, 2004	6200	1000
Sultan et al., 1997	287950	50000	Linstadter and Kropelin, 2004	5405	75
Sultan et al., 1997	273950	38000	Kleindienst et al., 2016	195400	0
Sultan et al., 1997	282950	46000	Kleindienst et al., 2016	10600	0
Sultan et al., 1997	46950	2000	Kleindienst et al., 2016	87200	0
Sultan et al., 1997	191950	15000	Kleindienst et al., 2016	14000	0
Sultan et al., 1997	256950	34000	Kleindienst et al., 2016	91200	0
Sultan et al., 1997	158950	12000	Kleindienst et al., 2016	14300	0
Sultan et al., 1997	339950	98000	Kleindienst et al., 2016	89300	0

Sultan et al., 1997	288950	67000	Kleindienst et al., 2016	14200	0
Pachur and Holzman, 1991	31250	2080	Kleindienst et al., 2016	8400	0
Pachur and Holzman, 1991	30450	1200	Kleindienst et al., 2016	700	0
Wendorf et al., 1994	130950	7700	Kleindienst et al., 2016	14900	0
Wendorf et al., 1994	97950	14000	Kleindienst et al., 2016	1100	0
Wendorf et al., 1994	121250	22900	Kleindienst et al., 2016	48800	0
Wendorf et al., 1994	98350	7200	Kleindienst et al., 2016	5300	0
Wendorf et al., 1994	71950	10000	Kleindienst et al., 2016	84000	0
Wendorf et al., 1994	73350	8200	Kleindienst et al., 2016	7300	0
Wendorf et al., 1994	126950	0	Kleindienst et al., 2016	85300	0
Wendorf et al., 1994	85950	10000	Kleindienst et al., 2016	7800	0
Wendorf et al., 1994	106950	15000	Kleindienst et al., 2016	93700	0
Wendorf et al., 1994	107350	10500	Kleindienst et al., 2016	10800	0
Wendorf et al., 1994	110550	10600	Kleindienst et al., 2016	98400	0
Wendorf et al., 1994	105850	9500	Kleindienst et al., 2016	10100	0
Wendorf et al., 1994	66950	9000	Kleindienst et al., 2016	98500	0
Wendorf et al., 1994	115950	9800	Kleindienst et al., 2016	9900	0
Gaven et al., 1981	78950	6000	Kleindienst et al., 2016	99700	0
Gaven et al., 1981	91250	6000	Kleindienst et al., 2016	6600	0
Gaven et al., 1981	94450	7000	Kleindienst et al., 2016	101200	0
Gaven et al., 1981	41950	2000	Kleindienst et al., 2016	10400	0
Gaven et al., 1981	136950	11000	Kleindienst et al., 2016	106400	0
Gaven et al., 1981	140950	-14000	Kleindienst et al., 2016	11100	0
Gaven et al., 1981	142950	-12000	Kleindienst et al., 2016	106600	0
Gaven et al., 1981	144950	12000	Kleindienst et al., 2016	5600	0
Gaven et al., 1981	147950	16000	Kleindienst et al., 2016	106800	0
Gaven et al., 1981	159950	15000	Kleindienst et al., 2016	10700	0
Gaven et al., 1981	164950	20000	Kleindienst et al., 2016	110500	0
Gaven et al., 1981	166950	18000	Kleindienst et al., 2016	11100	0
Gaven et al., 1981	174950	16000	Kleindienst et al., 2016	111400	0
Gaven et al., 1981	92950	2000	Kleindienst et al., 2016	6200	0

Gaven et al., 1981	91950	20000	Kleindienst et al., 2016	115200	0
Gaven et al., 1981	123950	15000	Kleindienst et al., 2016	9600	0
Gaven et al., 1981	126950	11000	Kleindienst et al., 2016	122600	0
Gaven et al., 1981	128950	-13000	Kleindienst et al., 2016	11600	0
Gaven et al., 1981	129950	10000	Kleindienst et al., 2016	126700	0
Gaven et al., 1981	132950	9000	Kleindienst et al., 2016	24000	0
Gaven et al., 1981	134950	9000	Kleindienst et al., 2016	128900	0
Smith, 2001	127950	2000	Kleindienst et al., 2016	13000	0
Smith, 2001	137950	3000	Kleindienst et al., 2016	129900	0
Smith, 2001	151950	6500	Kleindienst et al., 2016	7000	0
Hamdan, 2000	170950	17000	Kleindienst et al., 2016	133000	0
Hamdan, 2000	161950	20000	Kleindienst et al., 2016	12700	0
Hamdan, 2000	46950	2000	Kleindienst et al., 2016	154400	0
Hamdan, 2000	47950	6000	Kleindienst et al., 2016	15300	0
Hamdan, 2000	65950	6000	Kleindienst et al., 2016	155700	0
Hamdan, 2000	21950	300	Kleindienst et al., 2016	20400	0
Hamdan, 2000	19950	300	Kleindienst et al., 2016	156500	0
Brookes, 2010	13950	0	Kleindienst et al., 2016	12100	0
Brookes, 2010	7950	0	Kleindienst et al., 2016	158100	0
Brookes, 2010	81950	0	Kleindienst et al., 2016	15700	0
Brookes, 2010	81950	0	Kleindienst et al., 2016	164600	0
Brookes, 2010	126950	5000	Kleindienst et al., 2016	15500	0
Brookes, 2010	106950	5000	Kleindienst et al., 2016	165400	0
Brookes, 2010	181950	5000	Kleindienst et al., 2016	13400	0
Brookes, 2010	176950	0	Kleindienst et al., 2016	185900	0
Brookes, 2010	176950	0	Kleindienst et al., 2016	14800	0
Brookes, 2010	241950	0	Kleindienst et al., 2016	201300	0

Brookes, 2010	201950	0	Kleindienst et al., 2016	23900	0
Brookes, 2010	336950	0	Kleindienst et al., 2016	205700	0
Brookes, 2010	291950	0	Kleindienst et al., 2016	28800	0
Brookes, 2010	486950	0	Kleindienst et al., 2016	205800	0
Brookes, 2010	511950	0	Kleindienst et al., 2016	20000	0
Kindermann et al., 2006	9450	500	Kleindienst et al., 2016	216000	0
Kindermann et al., 2006	10620	570	Kleindienst et al., 2016	13500	0
Kindermann et al., 2006	10180	570	Kleindienst et al., 2016	218400	0
Kindermann et al., 2006	9670	490	Kleindienst et al., 2016	18200	0
Kindermann et al., 2006	8620	0	Kleindienst et al., 2016	228300	0
Kindermann et al., 2006	8055	0	Kleindienst et al., 2016	22100	0
Kindermann et al., 2006	7913	0	Kleindienst et al., 2016	229100	0
Kindermann et al., 2006	7820	0	Kleindienst et al., 2016	32900	0
Kindermann et al., 2006	7588	0	Kleindienst et al., 2016	270400	0
Kindermann et al., 2006	7500	0	Kleindienst et al., 2016	27100	0
Kindermann et al., 2006	7421	0	Kleindienst et al., 2016	307000	0
Kindermann et al., 2006	7303	0	Kleindienst et al., 2016	30600	0
Kindermann et al., 2006	7260	0	Kleindienst et al., 2016	334200	0
Kindermann et al., 2006	7215	0	Kleindienst et al., 2016	34300	0
Kindermann et al., 2006	7040	0	Kleindienst et al., 2016	342000	0
Kindermann et al., 2006	7030	0	Kleindienst et al., 2016	33400	0
Kindermann et al., 2006	6959	0	Kleindienst et al., 2016	356300	0

Kindermann et al., 2006	6900	0	Kleindienst et al., 2016	34000	0
Kindermann et al., 2006	6885	0	Kleindienst et al., 2016	397600	0
Kindermann et al., 2006	6786	0	Kleindienst et al., 2016	37000	0
Kindermann et al., 2006	6753	0	Kleindienst et al., 2016	468000	0
Kindermann et al., 2006	6713	0	Kleindienst et al., 2016	54800	0
Kindermann et al., 2006	6696	0	Kleindienst et al., 2016	687600	0
Kindermann et al., 2006	6685	0	Kleindienst et al., 2016	102200	0
Kindermann et al., 2006	6605	0	-------	------	---